

DEPARTMENT OF PHYSICS, UNIVERSITY OF JYVÄSKYLÄ
RESEARCH REPORT No. ??/2019

**JET TRANSVERSE MOMENTUM DISTRIBUTIONS
FROM RECONSTRUCTED JETS
IN P–PB COLLISIONS AT $\sqrt{s_{\text{NN}}} = 5.02 \text{ TeV}$**

**BY
TOMAS SNELLMAN**

Academic Dissertation
for the Degree of
Doctor of Philosophy

Jyväskylä, Finland
June 2019

Author	Tomas Snellman University of Jyväskylä Finland
Supervisors	Dr. Kim Dong Jo University of Jyväskylä Finland
	Prof. Jan Rak University of Jyväskylä Finland
Reviewers	Prof. Stefan Bathe Baruch College, CUNY USA
	Prof. Marcin Chrząszcz Instytut Fizyki Jądrowej PAN Poland
Opponent	Prof. Jamie Nagle University of Colorado Boulder USA

¹ *Acknowledgements

Contents

1	Introduction	2
1.1	Quantum chromodynamics	4
1.1.1	Foundation of QCD	4
1.1.2	Asymptotic Freedom	7
1.2	Heavy-ion physics	9
1.2.1	History	10
1.3	Features of Heavy-Ion Collisions	11
1.3.1	Collision Geometry	11
1.3.2	Collective motion	15
1.4	Hard processes	22
1.4.1	pQCD factorization	22
1.4.2	Jet showering	24
1.4.3	Soft gluon radiation and angular ordering	25
1.4.4	Jet hadronisation	27
1.4.5	Interactions between jet and medium	31
1.4.6	New paradigm of jet Quenching	35
1.5	QGP in Small systems	40
1.5.1	Collective phenomena	40
1.5.2	Absence of jet quenching	41
1.5.3	Centrality determination in small systems	44
2	Experimental Setup	47
2.1	CERN	47
2.2	Large Hadron Collider	48
2.2.1	LHC experiments	49
2.3	ALICE	50
2.3.1	Tracking	51
2.3.2	TPC	53
2.3.3	Particle identification	54
2.3.4	Electromagnetic Calorimeter	55
2.3.5	Forward and trigger detectors	56
2.3.6	Muon spectrometer	58
2.3.7	Triggers	58
2.4	TPC upgrade	60
2.4.1	ALICE upgrade during LS2	60
2.4.2	TPC upgrade	60

38	3 Event and track selection	64
39	3.1 Event selection	64
40	3.2 Track reconstruction	64
41	3.3 Cluster selection	68
42	4 Analysis method	70
43	4.1 Jet Finding	70
44	4.1.1 Anti k_T algorithm	70
45	4.2 Definition of j_T	71
46	4.3 Unfolding detector effects	73
47	4.3.1 Bayesian unfolding	74
48	4.3.2 Toy Monte Carlo	76
49	4.3.3 Pythia Response matrices	77
50	4.3.4 Unfolding closure test	78
51	4.4 Background	81
52	4.4.1 Perpendicular cone background	81
53	4.4.2 Random background	83
54	4.5 Fitting	84
55	5 Systematic uncertainties	86
56	5.1 Background	86
57	5.2 Unfolding	86
58	5.2.1 Effect of number of iterations	87
59	5.2.2 Effect of different prior	87
60	5.2.3 Effect of p_T truncation	87
61	5.3 Tracking	90
62	5.4 EMCAL clusters	91
63	5.5 Summary of systematic uncertainties	93
64	6 Results	94
65	6.1 High multiplicity events	96
66	7 Discussions	98
67	7.1 Comparing dihadron and jet j_T results	98
68	7.1.1 Different R parameters	99
69	7.1.2 Leading tracks versus jet as reference	100
70	8 Summary	104

71 1 Introduction

72 This thesis focuses on studying Quantum Chromodynamics (QCD) [1], a part of
73 the standard model of particle physics [2], which is the theory describing the strong
74 interactions. Strong interaction is the force responsible for interactions that holds
75 the nucleus of an atom together. Fundamentally it describes the interactions be-
76 tween quarks and gluons, the elementary constituents of the building blocks of the
77 nucleus, protons and neutrons. Because of specifics of this interaction quarks and
78 gluons, together dubbed partons, can never be seen free [3]. Under ordinary con-
79 ditions they are confined into bound states called hadrons. In extreme conditions
80 they can form a medium of asymptotically free quarks and gluons, quark-gluon
81 plasma (QGP) [4].

82 Indirectly quarks can be seen in high energy particle collisions as jets, colli-
83 mated streams of particles observed in high energy particle collisions [5]. The
84 physics of these jets is the primary topic discussed in this thesis. Understanding
85 jets is important when one is interested in the processes that produce the partons
86 that eventually fragment into jets. By themselves jets can provide an insight into
87 QCD when the fragmentation is studied. Jets can also be used as probes of the
88 QGP medium.

89 Experimentally jets are often studied with a jet reconstruction algorithm which
90 clusters observed tracks to find a reasonable estimate of the initial parton. That is
91 also the case in this thesis. The main observable studied is the jet fragmentation
92 transverse momentum j_T which is defined as the perpendicular component of the
93 momentum of jet constituents with respect to the jet axis, the best estimate of
94 the initial parton. j_T measures the transverse nudge that fragmentation products
95 receive.

96 The analysis studies collisions between protons and lead nuclei. Originally
97 meant as a reference for lead-lead collisions to rule out possible cold nuclear mat-
98 ter effects [6]; effects caused by the regular 'cold' nuclear matter of a nucleus as
99 opposed to QGP. However, p-Pb collisions have provided interesting physics by
100 themselves. Many of the collective phenomena that in Pb-Pb collisions were att-
101 tributed to QGP have been observed also in high multiplicity p-Pb collisions [7]
102 and even in ultra high multiplicity pp collisions [7]. However observables of jet
103 modification show no conclusive signals in p-Pb collisions [6, 7].

104 This thesis is organised as follows: Section 1 first gives a general introduction
105 into the history and properties of QCD and Heavy-Ion physics. It is followed by a
106 description of hard processes, jet fragmentation and hadronisation and how these
107 processes might look like in a Heavy-Ion environment. Finally there is a discussion
108 on the physics of small systems.

109 The experimental setup that was used to collect the data in this thesis is
110 described in Section 2. It starts by explaining the accelerator facilities at CERN

111 and LHC in more detail. This is followed by a description of the ALICE experiment
112 and its sub-detectors. A part of Section 2 is dedicated to coming upgrades of
113 ALICE as this is a timely topic. In 2019-2020 ALICE will be upgraded and I have
114 made a personal contribution to the TPC upgrade.

115 Section 3 gives a description of the event, track and cluster selection criteria
116 used in the analysis. This is followed in Section 4 by the specific analysis methods
117 used in this thesis. First the jet reconstruction algorithm used, anti- k_T , is de-
118 scribed. Section 4 continues by introducing the j_T observable, how it is obtained
119 and what methods are used to estimate background contribution and correct for
120 detector effects. Finally the fitting method used for the final results is described.
121 Section 5 gives the different systematic uncertainties that arise from the analysis.

122 Finally the results from the analysis are presented in Section 6. The results
123 are compared to PYTHIA and Herwig Monte Carlo generators. Further discussion
124 of the results is given in Section 7 when the results are compared to j_T results
125 obtained with a different analysis method. Section 8 summarises the main results
126 and gives an outlook for future.

127 **1.1 Quantum chromodynamics**

128 **1.1.1 Foundation of QCD**

129 There are four known basic interactions in the universe: gravity, electromagnetic,
130 weak and strong interactions. The standard model of particle physics [2] includes
131 three of these, electromagnetic, weak and strong interactions. The fourth one,
132 gravity, is described well in all but the most extreme of cases by the theory of
133 general relativity [8]. The standard model is a quantum field theory where particle
134 interactions are dictated by local gauge symmetries [5].

135 The first interaction included in the standard model was the electromagnetic
136 interaction. The foundations of quantum field theory and Quantum Electrody-
137 namics (QED) were already laid out by the work by Dirac in 1927 [9]. The full
138 theory of QED was formulated in 1946-1949 by Tomonaga [10], Schwinger [11, 12],
139 Feynman [13]

140 Motivated by the success of a quantum field theory approach for the elec-
141 tromagnetic interaction physicists started working on the remaining interactions.
142 However, the weak and strong nuclear interactions proved more challenging to
143 formulate [14]. In the end the weak interaction was unified with the electromag-
144 netic interaction into the electroweak theory. The final theory was formulated by
145 Glashow [15], Salam [16] and Weinberg [17].

146 The theory of strong interactions became to be known as Quantum Chromo-
147 dynamics (QCD). The search for a theory of strong interactions began after the
148 formulation of QED and drew further inspiration from the introduction of new
149 powerful particle accelerators that were capable of particle physics research in the
150 1950s. Before this particles were mainly discovered from cosmic rays. Positrons,
151 neutrons and muons were discovered in the 1930s and charged pions were discov-
152 ered in 1947 [18, 19]. The neutral pion was discovered in 1950 [20].

153 The Lawrence Berkeley National Laboratory started the Bevalac accelerator in
154 1954, Super Proton Synchrotron (SPS) in CERN began operating in 1959 and the
155 Alternating Gradient Synchrotron (AGS) at Brookhaven started in 1960. With
156 an energy of 33 GeV AGS was the most powerful accelerator of that time. By the
157 beginning of 1960s several new particles had been discovered. These included an-
158 tiprotons [21], antineutrons [22], Δ -particles and the six hyperons (Ξ^0 [23], Ξ^- [24],
159 Σ^\pm [25], Σ^0 [26] and Λ [27]).

160 Facing this avalanche of new particles, physicists started the search for symme-
161 tries within them. Already in 1932 Heisenberg [28] had proposed an isospin model
162 to explain similarities between the proton and the neutron. In 1962 Gell-Mann
163 and Ne’eman presented that particles sharing the same quantum numbers (spin,
164 parity) could be organised using the symmetry of SU(3). [29] Heisenberg’s Isospin
165 model followed the symmetry of SU(2). Using the SU(3) model known baryons

¹⁶⁶ and mesons could be presented as octets. This also lead to the discovery of the
¹⁶⁷ Ω^- [30] particle since this was missing from the SU(3) decouplet that included
¹⁶⁸ heavier baryons.

¹⁶⁹ The most simple representation of SU(3) was a triplet. Inside this triplet
¹⁷⁰ particles would have electric charges $2/3$ or $-1/3$. However, these had not been
¹⁷¹ detected. In 1964 Gell-Mann [31] and Zweig [32] proposed that baryons and mesons
¹⁷² would be bound states of these three hypothetical triplet particles that Gell-Mann
¹⁷³ called quarks and Zweig called aces. Now we know that these are the u , d and s
¹⁷⁴ quarks. However, this original quark model without colour was violating the Pauli
¹⁷⁵ exclusion principle. For example the Ω^- particle is comprised of three s quarks,
¹⁷⁶ two of which would have exactly the same quantum states, since spin can only
¹⁷⁷ have two values.

¹⁷⁸ The idea of colour had already been presented by Greenberg in 1964 [33]. In
¹⁷⁹ 1971 Gell-Mann and Fritzsch presented their model [34], which solved the antisym-
¹⁸⁰ metry problem. They added a colour quantum number to quarks, which separated
¹⁸¹ quarks of the same species. In the new colour model the baryonic wave function
¹⁸² became

$$(qqq) \rightarrow (q_r q_g q_b - q_g q_r q_b + q_b q_r q_g - q_r q_b q_g + q_g q_b q_r - q_b q_g q_r), \quad (1)$$

¹⁸³ The colour model was also supported by experimental evidence. The decay rate
¹⁸⁴ of a neutral pion with the addition of colours is

$$\Lambda(\pi^0 \rightarrow \gamma\gamma) = \frac{\alpha^2}{2\pi} \frac{N_c^2}{3^2} \frac{m_\pi^3}{f_\pi^2}. \quad (2)$$

¹⁸⁵ For $N_c = 3$ this gives 7.75 eV and the measured value is (7.86 ± 0.54) eV [35].

¹⁸⁶ Another observable that combines the colour information also to the number
¹⁸⁷ of quark flavours is the Drell-Ratio R [36]

$$R = \frac{\sigma(e^+ + e^- \rightarrow \text{hadrons})}{\sigma(e^+ + e^- \rightarrow \mu^+ + \mu^-)} = N_c \sum_f Q_f^2. \quad (3)$$

¹⁸⁸ This ratio has the numerical value 2 when including the three light quarks u , d
¹⁸⁹ and s . When the collision energy reaches the threshold of heavy quark (c and
¹⁹⁰ b) production processes this increases to $^{10}/3$ (for $f = u, d, s, c$) and $^{11}/3$ (for $f =$
¹⁹¹ u, d, s, c, b). The energy threshold ($\sqrt{s} \approx 350$ GeV) of $t\bar{t}$ production, has not been
¹⁹² reached so far by any e^+e^- colliders.

¹⁹³ The colour model explained why no free quarks had been observed as only
¹⁹⁴ colour neutral states are possible. The simplest ways of producing a colour neu-
¹⁹⁵ tral object are the combination of three quarks, and the combination of a quark-
¹⁹⁶ antiquark pair. These are known as baryons and mesons.

197 First experimental indication of the existence of quarks came in 1969 when a
198 series of experiments at the Stanford Linear Accelerator Center (SLAC) revealed
199 that protons and neutrons appeared to have some substructure [37, 38]. For this
200 discovery they eventually received the Nobel Prize in Physics in 1990 [39]. Bjorken
201 demonstrated that these results could be explained if protons and neutrons were
202 composed of virtually noninteracting pointlike particles [40, 41]. Feynman [42]
203 interpreted these objects as real particles and suggested they would be the quarks
204 of Gell-Mann’s model. At the time, however, this seemed mysterious; if all strongly
205 interacting particles, hadrons, were composed of quarks, then quarks should surely
206 be strongly interacting themselves. Why would they appear to be almost free
207 inside hadrons? This turned out to be a key clue in formulating the theory of
208 strong interactions. [14]

209 After the addition of colour the main ingredients of QCD had been established.
210 The final quantum field theory of Quantum Chromodynamics formed quickly be-
211 tween 1972 and 1974. Main part of this was the work by Gross, Wilczek, Politzer
212 and George for non-abelian gauge field theories [1, 43–46]. The work showed that
213 quarks would indeed be asymptotically free in a non-abelian theory, which ex-
214 plained the results from SLAC. Gross, Wilczek and Politzer received the Nobel
215 Prize in Physics for their work [47]. The role of gluons as a colour octet was pre-
216 sented by Fritzsch, Gell-Mann and Leutwyler in 1973 [48]. The theory had now 8
217 massless gluons to mediate the strong interaction.

218 The quark model was extended in 1974 when the discovery of the charm quark
219 and the first charmed hadron, J/Ψ , was simultaneously published by teams from
220 the SLAC [49], from Brookhaven National Laboratory [50] and from the ADONE
221 collider in Frascati, Italy [51]. In 1976 the Nobel Prize in Physics was awarded to
222 Richter and Ting for the discovery of the charm quark [52]. The existence of a
223 fourth quark had already been speculated in 1964 by Bjorken and Glashow [53], but
224 a proper prediction was provided by Glashow, Iliopoulos and Maiani in 1970 [15]
225 based on symmetries between leptons and quarks in weak interactions.

226 However, these gluons had not been discovered. Indirect evidence of the ex-
227 istence had been seen as it was observed that only about half of the momentum
228 of protons was transported by the quarks [54]. Direct evidence should be seen in
229 electron-electron collisions as a third, gluonic, jet in addition to two quark jets.
230 Three jet events were first seen in 1979 at the PETRA accelerator at DESY [55–57].

231 The two remaining quarks, bottom and top, were introduced by Kobayashi
232 and Maskawa to explain CP-violation [58]. For this they received the Nobel Prize
233 in Physics in 2008 [59]. Bottom quark was discovered soon after, in 1977, at
234 Fermilab [60]. The heaviest quark, top quark, would eventually be discovered in
235 1995 by the CDF [61] and DØ [62] experiments at Fermilab.

236 **1.1.2 Asymptotic Freedom**

237 In Quantum Electrodynamics (QED) the electric charge is screened. In the vicinity
238 of a charge, the vacuum becomes polarized. Virtual charged particle-antiparticle
239 pairs around the charge are arranged so that opposing charges face each other.
240 Since the pairs also include an equal amount opposite charge compared to the
241 original charge the average charge seen by an observer at a distance is smaller.
242 When the distance to the charge increases the effective charge decreases until the
243 coupling constant of QED reaches the fine-structure constant $\alpha = \frac{1}{137}$. [5]

244 Contrary to QED, QCD is a non-abelian theory. In other words the generators
245 of the symmetry group of QCD, SU(3), do not commute. This has the practical
246 consequence that gluons interact also with other gluons, whereas in QED the
247 neutral carrier particles, photons, only interact with charged particles. There
248 is screening also in QCD because of the colour charges, but in addition to that
249 there is antiscreening because of the gluon interactions. In QCD the antiscreening
250 effect dominates over screening. Thus for larger distances to the colour charge
251 the coupling constant is larger. This explains why no free colour charges can be
252 observed. When the distance between charges increases the interaction strengthens
253 until it is strong enough to produce a new quark-antiquark pair. On the other
254 hand, at very small distances the coupling constant approaches zero. This is
255 called asymptotic freedom. [5]

256 In 1975 Collins [63] predicted a state where individual quarks and gluons are
257 no longer confined into bound hadronic states. Instead they form a bulk QCD
258 matter that Edward Shuryak called Quark-Gluon plasma in his 1980 review of
259 QCD and the theory of superdense matter [4]. QGP can be seen as a separate
260 state of matter. A schematic view of a phase diagram for QCD matter is shown
261 in Figure 1.

262 In the early universe at the age of 10^{-6} s after the Big Bang the conditions
263 preferred the existence of QGP instead of hadronic matter. Nowadays bulk QCD
264 matter, its properties and its phase transitions between hadronic matter and the
265 quark-gluon plasma (QGP) can be explored in the laboratory, through collisions
266 of heavy atomic nuclei at ultra-relativistic energies. The study of QCD matter at
267 high temperature is of fundamental and broad interest. The phase transition in
268 QCD is the only phase transition in a quantum field theory that can be probed by
269 any present or foreseeable technology.

270 One important property of the QGP is the shear viscosity to entropy ratio, η/s .
271 It is believed that this ratio has an universal minimum value of $1/4\pi \approx 0.08$, among
272 all substances in nature. This limit would be reached in the strong coupling limit
273 of certain gauge theories [65]. The temperature dependance of the ratio is shown
274 in Figure 2. The minimum value of η/s is found in the vicinity of the critical
275 temperature, T_c [66]. Finding the η/s values in QGP matter would therefore also

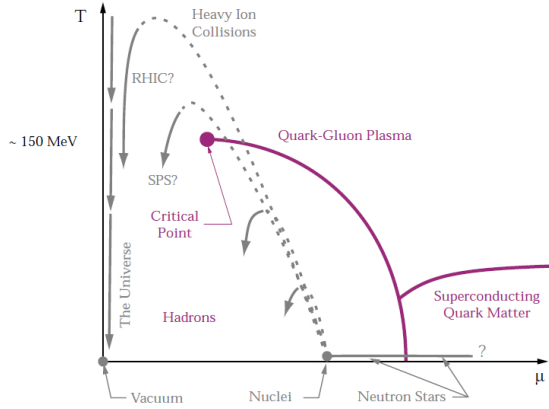


Figure 1: A schematic outline for the phase diagram of QCD matter at ultra-high density and temperature. The quark chemical potential μ that is on the x-axis represents the imbalance between quarks and antiquarks. At zero temperature this corresponds to the number of quarks but at higher temperatures there are also additional pairs of quarks and antiquarks. Along the horizontal axis the temperature is zero, and the density is zero up to the onset transition where it jumps to nuclear density, and then rises with increasing μ . Neutron stars are in this region of the phase diagram, although it is not known whether their cores are dense enough to reach the quark matter phase. Along the vertical axis the temperature rises, taking us through the crossover from a hadronic gas to the quark-gluon plasma. This is the regime explored by high-energy heavy-ion colliders. [64]

276 provide a way of determining the critical point of QCD matter.

277 The η/s value for the matter created in Au–Au collisions at RHIC ($\sqrt{s_{NN}} =$
 278 200 GeV) has been estimated to be 0.09 ± 0.015 [66], which is very close to the
 279 lowest value for a wide class of thermal quantum field theories [65] for all relativistic
 280 quantum field theories at finite temperature and zero chemical potential. This
 281 suggests that the the matter created goes through a phase where it is close to the
 282 critical point of QCD.

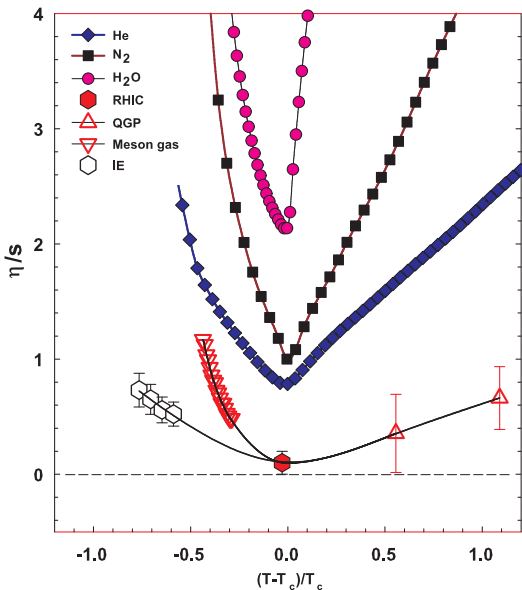


Figure 2: η/s as a function of $(T - T_c)/T_c$ for several substances as indicated. The $\eta/s = 0.09 \pm 0.015$ estimate at RHIC comes from Au–Au collisions at $\sqrt{s_{NN}} = 200$ GeV. The calculated values for the meson-gas have an associated error of $\sim 50\%$. The lattice QCD value $T_c = 170$ MeV is assumed for nuclear matter. The lines are drawn to guide the eye. [66]

283 1.2 Heavy-ion physics

284 The Quark Gluon Plasma (QGP) is experimentally accessible by colliding heavy-
 285 ions at high energies. Nowadays research of Heavy-Ion Collisions is mainly per-
 286 formed at two particle colliders; The Relativistic heavy-ion Collider (RHIC) at
 287 BNL in New York, USA and the Large Hadron Collider (LHC) at CERN in Switzer-
 288 land. Energy densities at these colliders should be enough to produce QGP and
 289 convincing evidence of the creation has been seen at both colliders. Complimen-
 290 tary research with heavy nuclei is also performed at the Super Proton Synchrotron
 291 (SPS) at CERN.

292 The development of heavy-ion physics is strongly connected to the development
 293 of particle colliders. Experimental study of relativistic heavy-ion collisions has been
 294 carried out for three decades, beginning with the Bevalac at Lawrence Berkeley
 295 National Laboratory (LBNL) [67], and continuing with the AGS at Brookhaven
 296 National Laboratory (BNL) [68], CERN SPS [69], RHIC at BNL and LHC at
 297 CERN.

298 **1.2.1 History**

299 The first heavy-ion collisions were performed at the Bevalac experiment at the
300 Lawrence Berkeley National Laboratory [67] and at the Joint Institute for Nu-
301 clear Research in Dubna [70] at energies up to 1GeV per nucleon. In 1986 the
302 Super Proton Synchrotron (SPS) at CERN started to look for QGP signatures in
303 O+Pb collisions. The center-of-mass energy per colliding nucleon pair ($\sqrt{s_{NN}}$)
304 was 19.4 GeV [69]. These experiments did not find any decisive evidence of the
305 existence of QGP. In 1994 a heavier lead (Pb) beam was introduced for new experi-
306 ments at $\sqrt{s_{NN}} \approx 17$ GeV. At the same time the Alternating Gradient Synchrotron
307 (AGS) at BNL, Brookhaven collided ions up to ^{32}S with a fixed target at energies
308 up to 28 GeV [68]. In 2000 CERN [71] presented compelling evidence for the ex-
309 istence of a new state of matter. Now SPS is used with 400 GeV proton beams
310 for fixed-target experiments, such as the SPS heavy-ion and Neutrino Experiment
311 (SHINE) [72], which tries to search for the critical point of strongly interacting
312 matter.

313 The Relativistic heavy-ion Collider (RHIC) at BNL in New York, USA started
314 its operation in 2000. The top center-of-mass energy per nucleon pair at RHIC,
315 200 GeV, was reached in the following years. The results from the experiments at
316 RHIC have provided a lot of convincing evidences that QGP was created [73–76].
317 The newest addition to the group of accelerators capable of heavy-ion physics is the
318 Large Hadron Collider (LHC) at CERN, Switzerland. LHC started operating in
319 November 2009 with proton-proton collisions. First Pb-Pb heavy-ion runs started
320 in November 2010 with $\sqrt{s_{NN}} = 2.76$ TeV, over ten times higher than at RHIC.
321 Since then LHC has provided both Pb-Pb and p-Pb collisions and a short period
322 of XeXe collisions. Table 1 shows a summary of these. Among the six experiments
323 at LHC, the Large Ion Collider Experiment (ALICE) is dedicated to heavy-ion
324 physics. Also CMS and ATLAS have active heavy-ion programs and LHCb uses
325 its SMOG [77] to perform unique fixed target collisions with heavy ions.

Table 1: Summary of datasets. The integrated luminosities are from ALICE.

Run 1 (2009-2013)			Run 2 (2015-2018)		
pp	0.9 TeV	$\sim 200 \mu\text{b}^{-1}$	pp	5.02 TeV	$\sim 1.3 \text{ pb}^{-1}$
	2.76 TeV	$\sim 100 \text{ nb}^{-1}$		13.0 TeV	$\sim 25 \text{ pb}^{-1}$
	7.0 TeV	$\sim 1.5 \text{ pb}^{-1}$	p-Pb	5.02 TeV	$\sim 3 \text{ nb}^{-1}$
	8.0 TeV	$\sim 2.5 \text{ pb}^{-1}$		8.16 TeV	$\sim 25 \text{ nb}^{-1}$
p-Pb	5.02 TeV	$\sim 15 \text{ nb}^{-1}$	XeXe	5.44 TeV	$\sim 0.3 \mu\text{b}^{-1}$
Pb-Pb	2.76 TeV	$\sim 75 \mu\text{b}^{-1}$	Pb-Pb	5.02 TeV	$\sim 1 \text{ nb}^{-1}$

326 1.3 Features of Heavy-Ion Collisions

327 1.3.1 Collision Geometry

328 In contrast to protons atomic nuclei are objects with considerable transverse size.
 329 The properties of a heavy-ion collision depend strongly on the impact parameter
 330 \vec{b} which is the vector connecting the centres of the two colliding nuclei at their
 331 closest approach. One illustration of a heavy-ion collision is shown in Figure 3.

332 Impact parameter defines the reaction plane which is the plane spanned by b
 333 and the beam direction. Ψ_{RP} gives the angle between the reaction plane and some
 334 reference frame angle. Experimentally the reference frame is fixed by the detector
 335 setup. Reaction plane angle cannot be directly measured in high energy nuclear
 collisions, but it can be estimated with the event plane method [78].

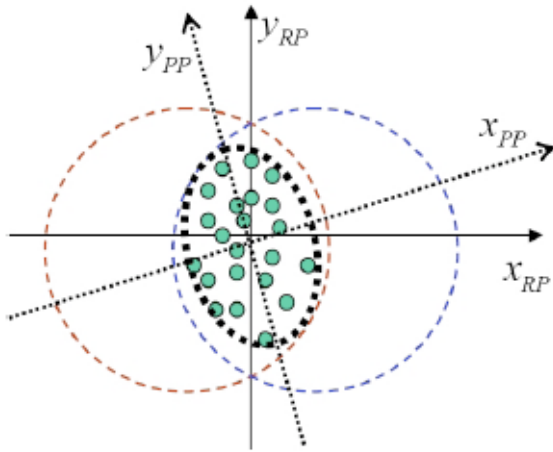


Figure 3: The definitions of the Reaction Plane and Participant Plane coordinate systems [79]. The dashed circles represent the two colliding nuclei and the green dots are partons that take part in the collision. x_{PP} and x_{RP} are the participant and reaction planes. The angle between x_{RP} and x_{PP} is given by Eq. (4). y_{PP} and y_{RP} are lines perpendicular to the participant and reaction planes.

336
 337 Participant zone is the area containing the participants. The distribution of
 338 nucleons in the nucleus exhibits time-dependent fluctuations. Because the nucleon
 339 distribution at the time of the collision defines the participant zone, the axis of
 340 the participant zone fluctuates and can deviate from the reaction plane. The angle
 341 between the participant plane and the reaction plane is defined by [80]

$$\psi_{PP} = \arctan \frac{-2\sigma_{xy}}{\sigma_y^2 - \sigma_x^2 + \sqrt{(\sigma_y^2 - \sigma_x^2)^2 + 4\sigma_{xy}^2}}, \quad (4)$$

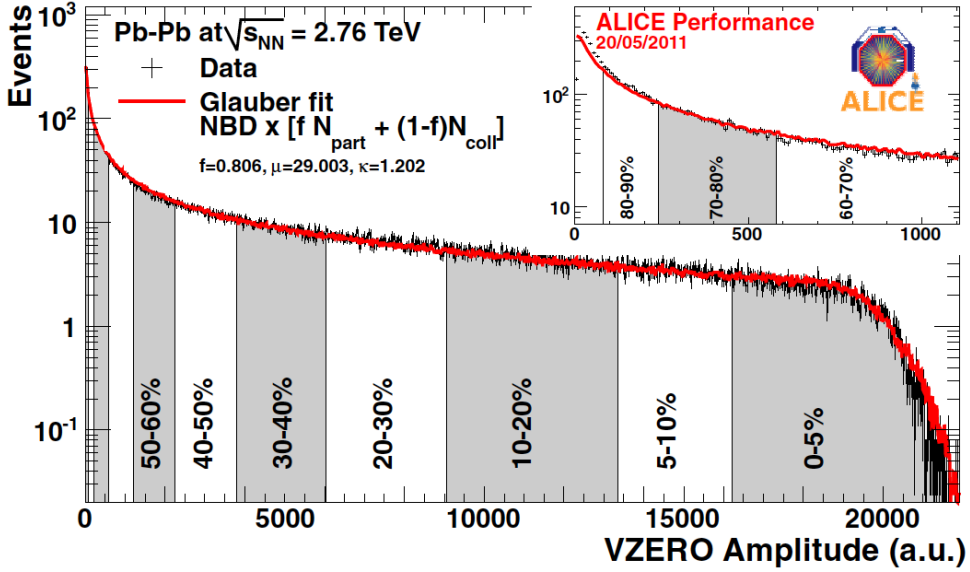


Figure 4: An illustration of the multiplicity distribution in ALICE measurements. The red line shows the fit of the Glauber calculation to the measurement. The data is divided into centrality bins [81]. The size of the bins corresponds to the indicated percentile.

342 where the σ -terms are averaged over the energy density.

$$\sigma_y^2 = \langle y^2 \rangle - \langle y \rangle^2, \sigma_x^2 = \langle x^2 \rangle - \langle x \rangle^2, \sigma_{xy} = \langle xy \rangle - \langle x \rangle \langle y \rangle \quad (5)$$

343 The impact parameter is one way to quantize the centrality of a heavy-ion
 344 collision but it is impossible to measure in a collision. It can be estimated from
 345 observed data using theoretical models, but this is always model-dependent and
 346 to compare results from different experiments one needs an universal definition for
 347 centrality.

348 Instead in practice centrality is defined by dividing collision events into per-
 349 centile bins by the number participants or experimentally by the observed mul-
 350 tiplicity. Centrality bin 0-5% corresponds to the most central collisions with the
 351 highest multiplicity and higher centrality percentages correspond to more periph-
 352 eral collisions with lower multiplicities. A multiplicity distribution from ALICE
 353 measurements [81] illustrating the centrality division is shown in Figure 4. The
 354 distribution is fitted using a phenomenological approach based on a Glauber Monte
 355 Carlo [82] plus a convolution of a model for the particle production and a negative
 356 binomial distribution.

357 The Glauber Model is often used to model the nuclear geometry in a heavy-

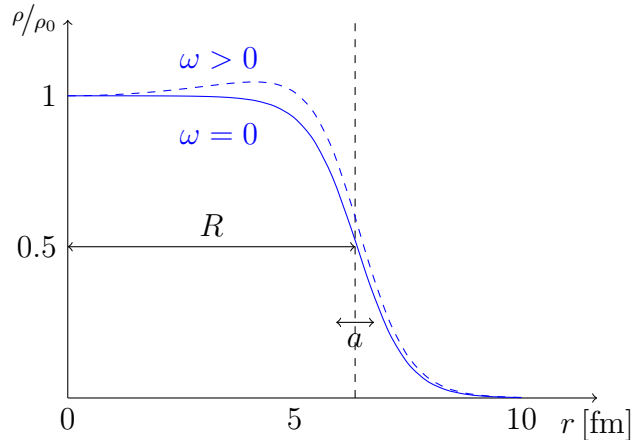


Figure 5: Woods-saxon distribution, with typical values for a Pb nucleus, $a = 0.55\text{fm}$ and $R = 6.6\text{fm}$.

358 ion collision. The model was originally introduced already in 1958 [83] and the
 359 modern terminology and tools were introduced in 1976 [84] by Białas, Bleszyński,
 360 and Czyż to model inelastic nuclear collisions.

361 The model starts by defining the thickness function which is the integral of the
 362 nuclear density over a line going through the nucleus with minimum distance s
 363 from its center

$$T_A(s) = \int_{-\infty}^{\infty} dz \rho(\sqrt{s^2 + z^2}), \quad (6)$$

364 where $\rho(\sqrt{s^2 + z^2})$ is the number density of nuclear matter. This can be exper-
 365 imently determined by studying the nuclear charge distribution in low-energy
 366 electron-nucleus scattering experiments [82, 85]. For a spherically symmetric nu-
 367 cleus a good approximation is given by the Woods-Saxon potential [86].

$$\rho(r) = \frac{\rho_0(1 + \omega r^2/R^2)}{1 + \exp(\frac{r-R}{a})}, \quad (7)$$

368 where ρ_0 is the nucleon density in center of the nucleus, R is the nuclear radius,
 369 a parametrizes the depth of the skin and ω can be used to introduce a surface
 370 excess. Figure 5 shows how this distribution looks like. With $\omega = 0$ the density
 371 stays relatively constant as a function of r until around R where it drops to almost
 372 0 within a distance given by a .

373 Overlap function is an integral of the thickness functions of two colliding nuclei
 374 over the overlap area. This can be seen as the material that takes part in the
 375 collision. It is given as a function of the impact parameter b

$$T_{AB}(\vec{b}) = \int d^2s T_A(\vec{s}) T_B(\vec{s} - \vec{b}) \quad (8)$$

³⁷⁶ The average overlap function, $\langle T_{AA} \rangle$, in an A-A collisions is given by [87]

$$\langle T_{AA} \rangle = \frac{\int T_{AA}(b) db}{\int (1 - e^{-\sigma_{pp}^{inel} T_{AA}(b)}) db}. \quad (9)$$

³⁷⁷ Using $\langle T_{AA} \rangle$ one can calculate the mean number of binary collisions

$$\langle N_{coll} \rangle = \sigma_{pp}^{inel} \langle T_{AA} \rangle, \quad (10)$$

³⁷⁸ where the total inelastic cross-section, σ_{pp}^{inel} , gives the probability of two nucleons
³⁷⁹ interacting. As each binary collision has equal probability for direct production
³⁸⁰ of high-momentum partons, the number of binary collisions is related to the hard
³⁸¹ processes in a heavy-ion collision. Thus the number of high momentum particles is
³⁸² proportional to $\langle N_{coll} \rangle$ [86, 88, 89]. This required knowledge of σ_{inel}^{NN} , which can be
³⁸³ measured in proton-proton collisions at different energies. At the LHC the most
³⁸⁴ precise cross section measurements come from TOTEM [90].

³⁸⁵ Soft production on the other hand is related to the number of participants [88].
³⁸⁶ It is assumed that in the binary interactions participants get excited and further
³⁸⁷ interactions are not affected by previous interactions because the time scales are
³⁸⁸ too short for any reaction to happen in the nucleons. After the interactions excited
³⁸⁹ nucleons are transformed into soft particle production. The average number of
³⁹⁰ participants, $\langle N_{part} \rangle$ can be calculated from the Glauber model

$$\begin{aligned} \langle N_{part}^{AB}(\vec{b}) \rangle &= \int d^2s T_A(\vec{s}) \left[1 - \left[1 - \sigma_{NN} \frac{T_B(\vec{s} - \vec{b})}{B} \right]^B \right] \\ &+ \int d^2s T_B(\vec{s}) \left[1 - \left[1 - \sigma_{NN} \frac{T_A(\vec{s} - \vec{b})}{A} \right]^A \right]. \end{aligned} \quad (11)$$

³⁹¹ There are two often used approaches to Glauber calculations. The optical ap-
³⁹² proximation is one way to get simple analytical expressions for the nucleus-nucleus
³⁹³ interaction cross-section, the number of interacting nucleons and the number of
³⁹⁴ nucleon-nucleon collisions. In the optical Glauber it is assumed that during the
³⁹⁵ crossing of the nuclei the nucleons move independently and they will be essentially
³⁹⁶ undeflected.

³⁹⁷ With increased appreciation of the physics emerging from fluctuations in the
³⁹⁸ collision geometry the Glauber Monte Carlo (GMC) approach has emerged as a

method to get a more realistic description of the collisions. In GMC the nucleons
 are distributed randomly in a three-dimensional coordinate system according to
 the nuclear density distributions [86]. A heavy-ion collision is then treated as
 a series of independent nucleon-nucleon collisions, where in the simplest model
 nucleons interact if their distance in the plane orthogonal to the beam axis, d ,
 satisfies

$$d < \sqrt{\sigma_{\text{inel}}^{\text{NN}}} \quad (12)$$

The average number of participants and binary collisions can then be determined
 by simulating many nucleus-nucleus collisions. The results of one GMC Pb-Pb
 event with impact parameter $b = 9.8$ fm is shown in Figure 6

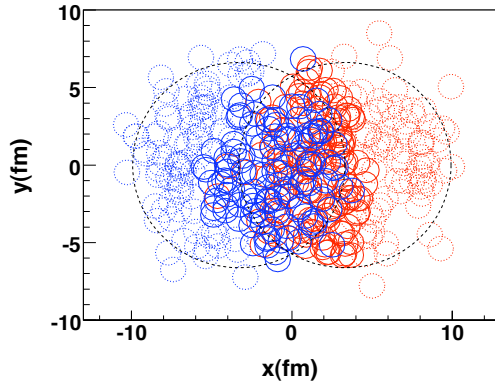


Figure 6: The results of one Glauber Monte Carlo simulation for a Pb–Pb collision.
 Big circles with black dotted boundaries represent the two colliding nuclei. The
 participant zone is highlighted with the solid red line. Small red and blue circles
 represent nucleons. Circles with solid boundaries are participants i.e. they interact
 with at least one nucleon from the other nucleus. Circles with dotted boundaries
 are spectators which do not take part in the collision. Figure from [91]

1.3.2 Collective motion

Quite often the evolution of a heavy-ion event can be divided into four stages. A
 schematic representation of the evolution of the collisions is shown in Figure 7.
 Stage 1 follows immediately the collision. This is known as the pre-equilibrium
 stage. The length of this stage is not known but it is assumed to last about $1 \text{ fm}/c$
 in proper time τ .

The second stage is the regime where thermal equilibrium or at least near-
 equilibrium is reached. This lasts about $5 - 10 \text{ fm}/c$ until the temperature of

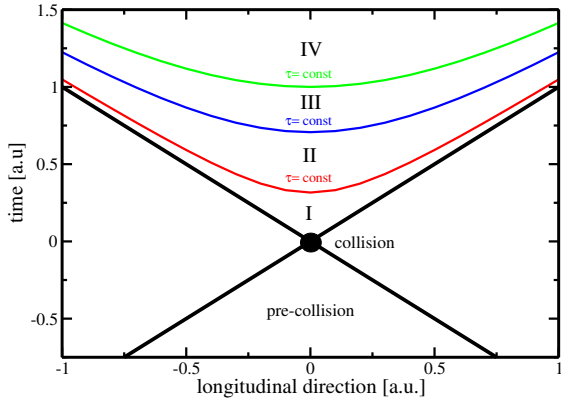


Figure 7: Schematic representation [92] of a heavy-ion collision as the function of time and longitudinal coordinates z . The various stages of the evolution correspond to proper time $\tau = \sqrt{t^2 - z^2}$ which is shown as hyperbolic curves separating the different stages.

416 the system sinks low enough for hadronization to occur and the system loses its
 417 deconfined, strongly coupled state. The third stage is the hadron gas stage where
 418 the hadrons still interact with each other. This ends when hadron scattering
 419 becomes rare and they no longer interact. In the final stage hadrons are free
 420 streaming and they fly in straight lines until they reach the detector.

421 In a heavy-ion collision the bulk collective particle production that is emitted
 422 from the QGP medium is referred to as flow. After the formation of the QGP, the
 423 matter begins to expand as it is driven outwards by the strong pressure difference
 424 between the center of the collision zone and the vacuum outside the collision vol-
 425 ume. The pressure-driven expansion is transformed into flow of low-momentum
 426 particles in the hadronization phase. Since the expansion is mainly isotropic the
 427 resulting particle flow is isotropic with small anisotropic corrections that are of the
 428 order of 10% at most. The isotropic part of flow is referred to as radial flow.

429 The transverse momentum spectra dN/dp_T in heavy-ion collisions is shown in
 430 Figure 8. The vast majority of produced particles have small p_T . The difference
 431 between the yield of 1 GeV/c and 4 GeV/c particles is already 2-3 orders of mag-
 432 nitude. Any observables that are integrated over p_T are therefore dominated by
 433 the small momentum particles.

434 The geometry of the heavy-ion collision produces an anisotropic component to
 435 the collective motion. In a non-central heavy-ion collision, with a large impact
 436 parameter, the shape of the impact zone is almond-like. In a central collision
 437 the overlap region is almost symmetric in the transverse plane. In this case the
 438 impact parameter is small. Collisions with different impact parameters are shown
 439 in Figure 9.

440 The pressure gradient is largest in-plane, in the direction of the impact parameter b , where the distance from high pressure, at the collision center, to low
441 pressure, outside the overlap zone, is smallest. This leads to stronger collective
442 flow along the direction of b , which in turn results in enhanced thermal emission
443 through a larger effective temperature into this direction, as compared to out-of-
444 plane [94–96]. The resulting flow is illustrated in Figure 9.

446 Flow is typically quantified in the form of a Fourier composition

$$E \frac{d^3N}{dp^3} = \frac{1}{2\pi p_T} \frac{d^2N}{dp_T d\eta} \left(1 + \sum_{n=1}^{\infty} 2v_n(p_T, \eta) \cos(n(\phi - \Psi_n)) \right), \quad (13)$$

447 where the coefficients v_n give the relative strengths of different anisotropic flow

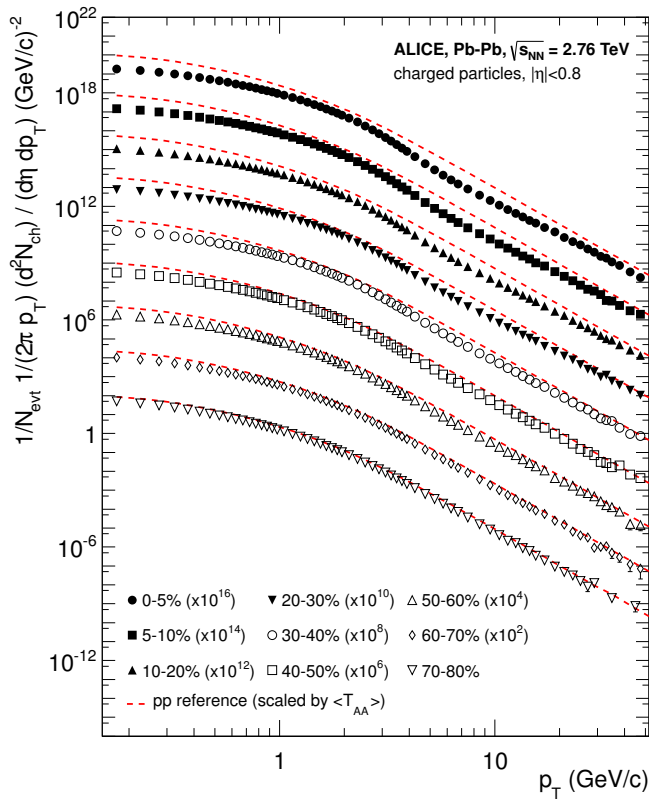


Figure 8: Charged particle spectra measured by ALICE [93] for the 9 centrality classes given in the legend. The distributions are offset by arbitrary factors given in the legend for clarity. The distributions are offset by arbitrary factors given in the legend for clarity. The dashed lines show the proton-proton reference spectra scaled by the nuclear overlap function determined for each centrality class and by the Pb-Pb spectra scaling factors [93].

448 components and the overall normalisation gives the strength of radial flow. Elliptic
 449 flow, i.e. flow with two maxima, is represented by v_2 and v_3 represents triangular
 450 flow. The first coefficient, v_1 , is connected to directed flow [97]. This will however
 451 in total be zero because of momentum conservation. It can be nonzero in some
 452 rapidity or momentum regions but it must be canceled by other regions.

453 In a peripheral collision v_2 is the dominant part of anisotropic flow as it arises
 454 from the asymmetric geometry of the collision region. Higher harmonics, the
 455 most notable of which is the triangular flow, come from fluctuations in the initial
 456 conditions [98]. As the colliding nuclei are not static objects, the arrangement of
 457 the nucleons at the time of the collision is random. The shape of the collision zone
 458 is not a perfect almond. Instead it can have a more complex shape. Also inside
 459 the collision zone the density of the created medium is not homogenous but it can
 460 have denser hot spots

461 It has been noted that higher harmonics of v_n would be suppressed by vis-
 462 cos effects and that the shape of v_n as a function of n would provide another
 463 valuable tool for studying η/s [99]. For a long time it was believed that the odd
 464 harmonics would be negligible. In 2007 Mishra et al. [100] argued that density
 465 inhomogeneities in the initial state would lead to non-zero v_n values for higher
 466 harmonics including v_3 .

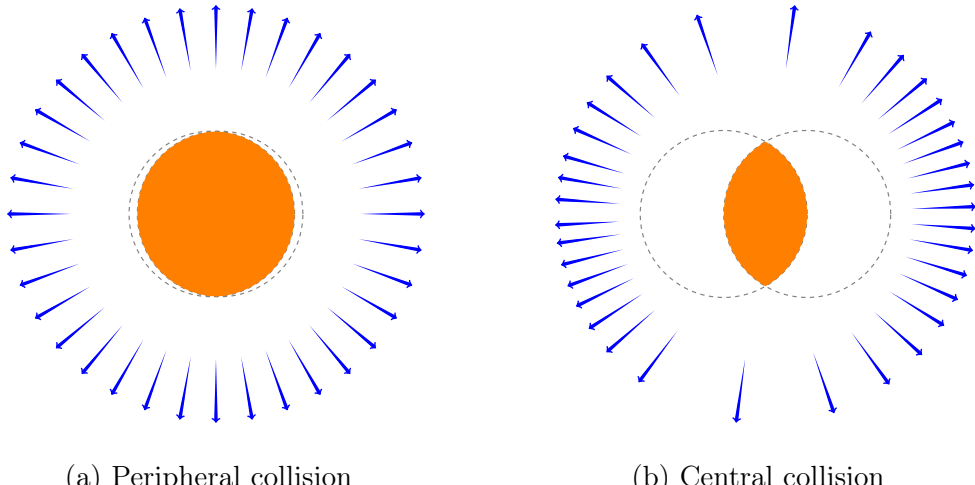


Figure 9: Illustration of flow in momentum space in central and peripheral collisions. The density of the arrows represent the magnitude of flow seen at a large distance from the collision in the corresponding azimuthal direction. In a peripheral collision momentum flow into in-plane direction is strong and flow into out-of-plane direction is weak. In a central collision anisotropy in flow is smaller, but the total yield of particles is larger.

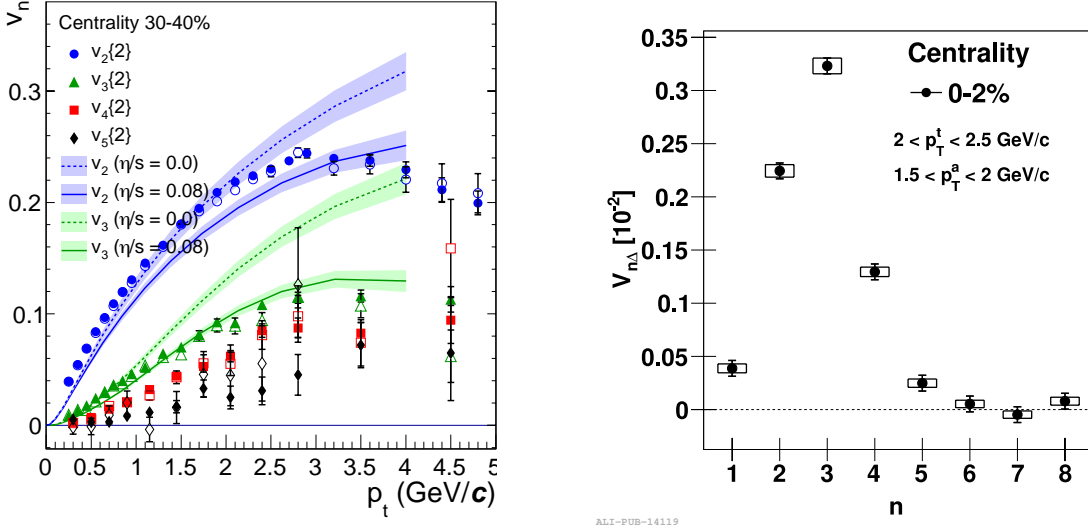


Figure 10: Flow measurements of higher harmonics. *left:* ALICE measurement of v_2 , v_3 , v_4 , v_5 as a function of transverse momentum. The flow coefficients are determined by two-particle correlations using different rapidity separations. The full and open symbols are for $\Delta\eta > 0.2$ and $\Delta\eta > 1.0$. The results are compared to hydrodynamic predictions [102] with different values of η/s [103]. *right:* Amplitude of v_n harmonics as a function of n for the 2% most central collisions as measured by ALICE [104].

467 The first one to predict anisotropic flow in heavy-ion collisions was Ollitrault
 468 in 1992 [94]. However, the first papers on anisotropy did not discuss the Fourier
 469 composition. Instead they approached the problem with a classic event shape
 470 analysis. (sphericity) The first experimental studies of anisotropy were performed
 471 at the AGS [101] in 1993, where it was noted that the anisotropy of particle
 472 production in one rapidity region correlates with the reaction plane angle defined
 473 in another rapidity region. The first ones to present the Fourier decomposition
 474 were Voloshin and Zhang in 1996 [97]

475 Measurements of different flow harmonics are shown in Figure 10. The left
 476 panel shows different flow harmonics as a function of p_T as measured by AL-
 477 ICE [103] in peripheral collisions. In general flow coefficients decrease as a function
 478 of n after $n = 2$. Central collisions are an exception. The right panel of Figure 10
 479 shows v_n as a function of n in central collisions as measured by ALICE [104]. The
 480 results are compared to hydrodynamic predictions [102].

481 The measured collective flow in heavy-ion collisions has been successfully mod-

482 elled with the relativistic version of hydrodynamics. The power of relativistic
483 hydrodynamics lies in its simplicity and generality. Hydrodynamics only requires
484 that there is local thermal equilibrium in the system. In order to reach thermal
485 equilibrium the system must be strongly coupled so that the mean free path is
486 shorter than the length scales of interest, which is assumed to hold for QGP phase
487 of a heavy-ion collision [92].

488 The use of relativistic hydrodynamics in high-energy physics dates back to
489 Landau [105] and the 1950's, before QCD was discovered. Back then it was used
490 in proton-proton collisions. Development of hydrodynamics for the use of heavy-
491 ion physics has been active since the 1980's, including Bjorken's study of boost-
492 invariant longitudinal expansion and infinite transverse flow [106]. Major steps
493 were taken later with the inclusion of finite size and and dynamically generated
494 transverse size [107, 108], a part of which was done at the University of Jyväskylä.

495 Understanding of the properties of the QGP has been improved with the help
496 of new data from LHC and RHIC and theoretical developments over the years.
497 For example, as shown in Figure 11(a), the quantification of the temperature de-
498 pendence shear viscosity over entropy ratio has been tested with event-by-event
499 Eskola-Kajantie-Ruuskanen-Tuominen (EKRT) + viscous hydrodynamic calcula-
500 tions [109], where the first qualitative possibilities were investigated. In this hy-
501 drodynamic calculations, the initial energy density profiles are calculated using a
502 next-to-leading order perturbative-QCD + saturation model (EKRT) [110, 111].
503 The subsequent space-time evolution is described by relativistic dissipative fluid
504 dynamics with different parametrisations for the temperature dependence of the
505 shear viscosity to entropy density ratio $\eta/s(T)$. This model gives a good descrip-
506 tion of the charged hadron multiplicity and the low- p_T region of the charged hadron
507 spectra at RHIC and the LHC [109]. Each of the $\eta/s(T)$ parametrisations have
508 been adjusted to reproduce the measured v_n from central to mid-peripheral col-
509 lisions. The model calculations in which the temperature of the phase transition
510 is larger than for "param1" are ruled out by the previous measurements [112] and
511 their studies. The remaining two sets of parameters which described most of data
512 is labeled as "best fits" in Figure 11(a). For the "param1" parametrisation the
513 phase transition from the hadronic to the QGP phase occurs at the lowest temper-
514 ature, around 150 MeV. This parametrisation is also characterised by a moderate
515 slope in $\eta/s(T)$ which decreases (increases) in the hadronic (QGP) phase.

516 The estimation of the η/s has been also established with Bayesian analysis,
517 which is applied to form the initial conditions with no assumptions on the physi-
518 cal mechanisms of the entropy production [113]. The robust statistical analytical
519 methods allows performing the model to data calibration in a multi-dimensional
520 parameter space. In addition to finding the most likely combination of input pa-
521 rameters, the Bayesian statistical method also provides the full uncertainty quan-

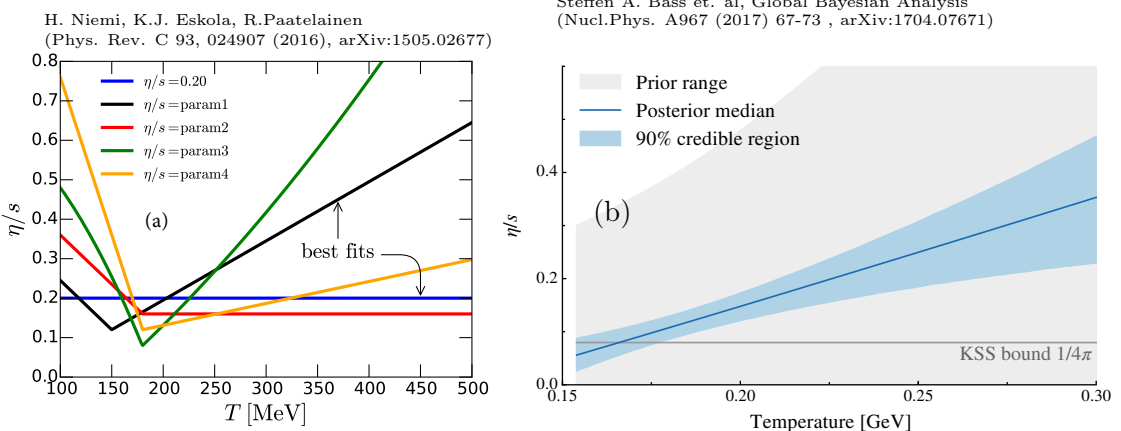


Figure 11: Temperature dependence of η/s . *left:* Different parametrisations of $\eta/s(T)$ that have been tested in hydrodynamical simulations. *right:* Result of a global Bayesian analysis narrowing down the possible $\eta/s(T)$ behaviour [113]

tification in the form of posterior probability distributions for all the parameters.
 522 The resulting $\eta/s(T)$ parametrisation is shown in Figure 11(b).

523 Based on the aforementioned model calculations, the phase transition from the
 524 hadronic to the QGP phase occurs at the lowest temperature, around 150 MeV.
 525 Although the temperature dependence of the η/s is currently not well known, the
 526 calculations generally suggest a minimum value of η/s from 0.08 to 0.12, close to
 527 the universal limit $1/(4\pi)$ [65].

528 Recently, several advancements have been made in order to further constrain
 529 the temperature dependence of η/s . New observables, such as the symmetric
 530 cumulants [112, 114], have provided detailed information on the temperature de-
 531 pendence over the evolution of the QGP. Furthermore, the non-linear formalism
 532 has resulted in remarkable new constraints on the initial conditions [115], and the
 533 η/s at the freeze-out conditions, for which is among the least understood parts of
 534 hydrodynamic calculations.

536 **1.4 Hard processes**

537 **1.4.1 pQCD factorization**

538 The term Hard Scattering is used in connection with the scattering of two point-
539 like constituents (partons) of colliding nucleons, when the momentum transfer Q^2
540 is large ($Q \gg \Lambda_{\text{QCD}}$). Figure 12 shows the incoming partons, quarks or gluons, as
541 they exchange a space-like virtual gluon and produce two highly virtual outgoing
542 partons. The outgoing partons will eventually fragment into collimated showers of
543 partons, referred to as jets.

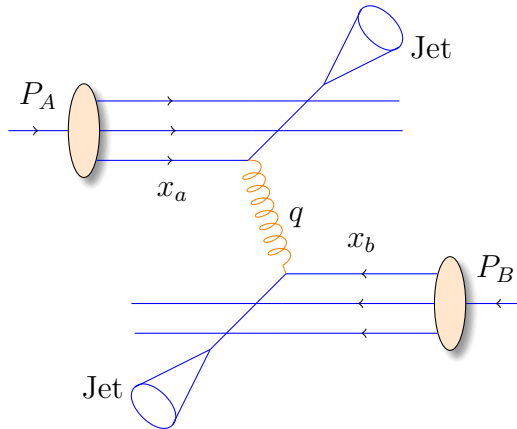


Figure 12: Schematic view of hard scattering process between 2 protons, producing 2 jets

544 Historically one would study hard scatterings foremost with inclusive hadron
545 spectra. In this context hadron production from hard scatterings can be factorised
546 into three components; the parton distribution functions f_a , f_b that give the prob-
547 ability of getting a parton with momentum fraction x of the proton, the cross
548 section of the elementary scattering $ab \rightarrow cd$, and the fragmentation functions
549 that give the probability of getting hadron h from the parton.

$$\frac{d\sigma_{pp}^h}{dy d^2p_T} = K \Sigma_{abcd} \int dx_a dx_b f_a(x_a, Q^2) f_b(x_b, Q^2) \frac{d\sigma}{dt} (ab \rightarrow cd) \frac{D_{h/c}^0}{\pi z_c}, \quad (14)$$

550 where

$$x_{a,b} = \frac{|p_{a,b}|}{|p_{\text{proton}}|}. \quad (15)$$

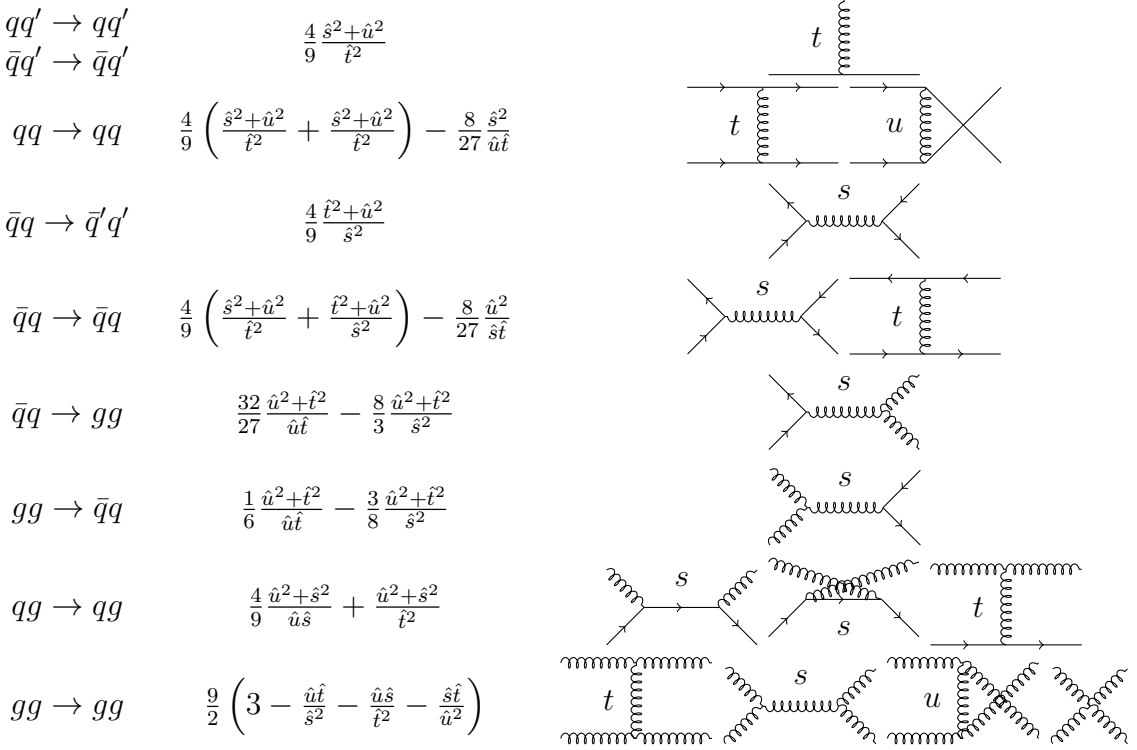


Figure 13: The basic pQCD processes and their quadratic matrix elements

551 Parton distribution functions will be discussed further in the following section.
 552 The elementary cross section $ab \rightarrow cd$ can be calculated from QCD. A summary
 553 of the first order $2 \rightarrow 2$ processes in QCD is shown in Figure 13.
 554 The final component in the factorization, fragmentation functions, describe the
 555 distribution of the fractional momenta of fragments radiated from the outgoing
 556 parton. In a leading order picture, it can be interpreted as the probability that
 557 the observed final state originates from a given parton [116]. Like the PDFs they
 558 are non-perturbative and must be determined experimentally. The measurement
 559 is usually performed in e^+e^- collisions where the kinematics are better controlled.

560 Parton Distribution Function

561 Parton Distribution Functions (PDFs) $f_a(x)$ give the differential probability for
 562 parton a to carry momentum fraction x of the proton momentum. As the PDFs
 563 cannot be calculated from first principles they are measured in Deeply Inelastic
 564 Scattering (DIS) experiments [117] and are extrapolated to the relevant momen-
 565 tum scales using the Dokshitzer-Gribov-Lipatov-Altarelli-Parisi (DGLAP) evolu-
 566 tion scheme [118–120]

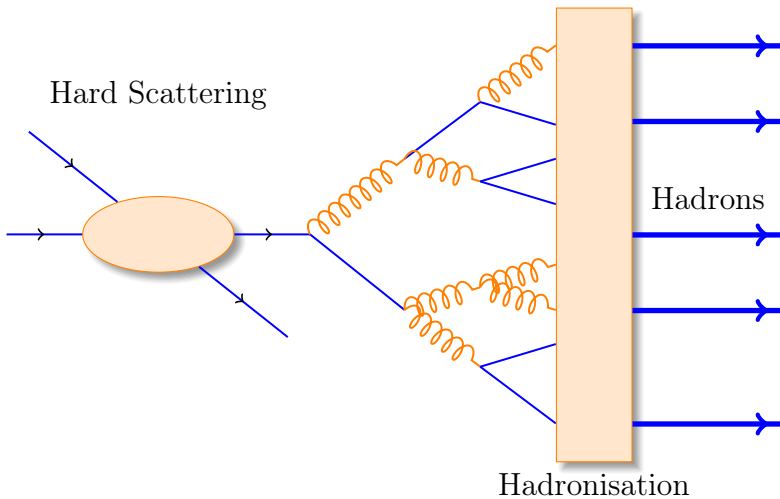


Figure 14: An illustration of jet showering. The highly virtual parton from the hard scattering will produce a shower of softer partons. When the virtuality is low enough the shower will go through a hadronisation process that produces the hadrons, which will be eventually observed in the detector.

$$\mu_F^2 \frac{\partial f_i(x, \mu_F^2)}{\partial \mu_F^2} = \sum_j \frac{\alpha_s(\mu_F)}{2\pi i} \int_x^1 \frac{dz}{z} P_{ij}(z) f_j\left(\frac{x}{z}, \mu_F^2\right), \quad (16)$$

where μ_F is a factorization scale. The splitting functions P_{ij} describe a probability to radiate parton i from parton j as a function of the momentum fraction z carried away by the offspring parton. Different theory interpretation and experimental data gives rise to different PDF's. Thus there are several commonly used PDF sets: CTEQ [121], HERAPDF [122], PDF4LHC [123], etc.

1.4.2 Jet showering

More detailed studies of the hard processes require a formulation of the showering process. The full picture is a complicated $2 \rightarrow n$ scattering, but it is typically seen as a series of $1 \rightarrow 2$ splittings with decreasing virtuality following the initial $2 \rightarrow 2$ scattering [124].

To first order the cascade is governed by the DGLAP evolution equation [118–120]

$$dP_a(z, Q^2) = \frac{dQ^2}{Q^2} \frac{\alpha_s}{2\pi} P_{a \rightarrow bc}(z) dz, \quad (17)$$

which gives the differential probability that parton a (mother) will branch to two partons b and c (daughters), at a virtuality scale Q^2 . Daughter b takes a fraction

z of the parton a energy and daughter c takes energy fraction $1 - z$. The splittings kernels $P_{a \rightarrow bc}(z)$ are

$$P_{q \rightarrow qg}(z) = \frac{4}{3} \frac{1+z^2}{1-z} \quad (18)$$

$$P_{g \rightarrow gg}(z) = 3 \frac{(1-z)(1-z)^2}{z(1-z)} \quad (19)$$

$$P_{g \rightarrow q\bar{q}}(z) = \frac{n_f}{2} (z^2 + (1-z)^2), \quad (20)$$

where n_f is the kinematically allowed number of quark flavours. There is some freedom in how the evolution variable Q^2 is chosen. If $Q^2 = f(z)m^2$ and $f(z)$ is a positive and a smooth function it holds that

$$\frac{dQ^2}{Q^2} dz = \frac{dm^2}{m^2} dz. \quad (21)$$

Of the Monte Carlo generators used in this thesis PYTHIA uses m^2 as the evolution variable [125], while HERWIG uses an energy-weighted emission angle $E^2(1 - \cos \theta) \approx m^2/z(1-z)$ [126].

Formally eq 17 corresponds to the emission of an infinite number of partons. However very soft and collinear gluons need not be considered and one can introduce an effective cut-off scale Q_0 , usually taken to be of the order of 1 GeV.

Going further one approach is to introduce time ordering, i.e. to decide which of the emissions occurs first. This is done in the form of a Sudakov form factor [127]

$$P_a^{no}(Q_{\max}^2, Q^2) = \exp \left(- \int_{Q^2}^{Q_{\max}^2} \int_{z_{\min}}^{z_{\max}} dP_a(z', Q'^2) \right), \quad (22)$$

which gives the probability that no emissions occur between the initial maximum scale Q_{\max}^2 and a given Q^2 and within limits $z_{\min} < z < z_{\max}$. Thus the probability for the first branching to occur at $Q^2 = Q_a^2$ is given by

$$d\Delta_a(z, Q_a^2, Q_{\max}^2) = dP_a(z, Q_a^2) P_a^{no}(Q_{\max}^2, Q_a^2). \quad (23)$$

Partons b and c that were produced will further branch with maximum virtuality scale Q_{\max}^2 given by Q_a^2 . Similarly their daughters will continue branching until the cutoff scale is reached, thus producing a shower.

1.4.3 Soft gluon radiation and angular ordering

Let us now consider a case where a gluon splits into two quarks, and one of the created quarks emits a soft gluon as seen in Figure 15. In the laboratory frame the time it takes for a gluon to be emitted from a quark can be estimated to be [128]

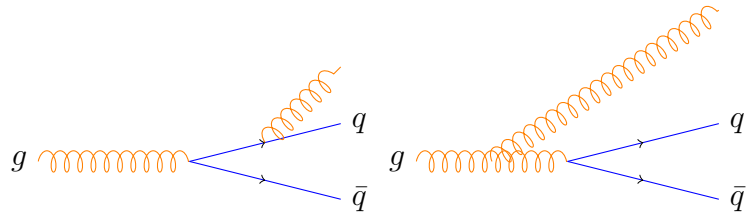


Figure 15: Soft gluon production

$$t_{\text{emit}} \approx \frac{1}{E_q}, \quad (24)$$

where the energy of the quark is given by E_q . In the rest frame of the quark its energy is given by its virtuality M_{virt} and assuming the quark is massless the Lorentz factor between the rest frame and the laboratory frame is

$$\gamma = \frac{E_q}{M_{\text{virt}}}. \quad (25)$$

Thus the emission time can be written as

$$t_{\text{emit}} \approx \frac{E_q}{M_{\text{virt}}^2} = \frac{E_q}{(k + p)^2}, \quad (26)$$

where k and p are the four-momenta of the gluon and the quark after the gluon emission. This can be written open in the laboratory frame. Through assuming that the end products are massless and Taylor-expanding the resulting cosine term gives a form that expresses the emission time using the opening angle θ_{kq} between the quark and the gluon

$$t_{\text{emit}} \approx \frac{1}{k\theta_{kq}^2}. \quad (27)$$

The transverse wavelength of the emitted gluon is $\lambda_{\perp}^{-1} = k_{\perp} \approx k\theta_{kq}$. Thus we get

$$t_{\text{emit}} \approx \frac{\lambda_{\perp}}{\theta_{kq}}. \quad (28)$$

The secondary gluon can only probe the quark of the earlier splitting if the transverse wavelength is smaller than the transverse separation of the produced $q\bar{q}$ pair. The transverse separation is given by

$$r_{\perp}^{q\bar{q}} \approx \theta_{q\bar{q}} t_{\text{emit}} \approx \lambda_{\perp} \frac{\theta_{q\bar{q}}}{\theta_{kq}}. \quad (29)$$

613 Thus in order for the emission to probe the individual quark, the opening angle
614 of the $q\bar{q}$ splitting, $\theta_{q\bar{q}}$, must be larger than θ_{kq} . If the opening angle θ_{kq} is larger,
615 the gluon can't distinguish between the quark and the antiquark, so it probes the
616 state of the system before the splitting, i.e. it can be treated like it was emitted
617 from the primary gluon.

618 This leads to the angular ordering of soft gluon radiation. Each successive angle
619 must be smaller than the previous one. The effect can be calculated in all orders
620 [128] and in the DGLAP formalism one can select the evolution variable Q^2 in a
621 way that ensures angular ordering as is done in the Herwig MC generator [126].
622 In PYTHIA 8 this is strictly not included, but the transverse momentum ordered
623 showers are as accurate in describing the soft gluon emissions as the angular or-
624 dered showers [127].

625 1.4.4 Jet hadronisation

626 When the virtuality of the shower is low enough, the shower starts to hadronise. In
627 this regime the parton shower reaches a scale close to Λ_{QCD} and the perturbative
628 description is no longer valid. Thus the hadronisation stage must be described in a
629 non-perturbative manner. In general hadronisation is assumed to be universal, i.e.
630 it shouldn't depend on the collision energy or system. The most simple scenario
631 that is used in several theory calculations is the so-called local parton-hadron
632 duality [129]. In the local parton-hadron duality hypothesis it is assumed that
633 there exists a low virtuality scale Q_0 in which the hadronisation happens, that is
634 independent of the scale of the primary hard process. At this scale the partons
635 are transformed into hadrons, assuming that the flow of momentum and quantum
636 numbers for the hadrons can be directly obtained from those of partons introducing
637 only small normalising constants.

638 The next sections will present more complicated hadronisation models used in
639 Monte Carlo generators, PYTHIA and Herwig.

640 Lund string model

641 One common implementation in MC generators is the Lund string fragmentation
642 algorithm [130]. The string model is based on the fact that in QCD linear confine-
643 ment is expected over large distances [127]. This can be modelled by imagining
644 a colour flux tube being stretched between the outgoing partons. The left side of
645 Figure 16 illustrates this point for a $q\bar{q}$ -pair. The tube is assumed to have a uni-
646 form fixed transverse size of about 1 fm along its length, which leads to a linearly
647 rising potential $V(r) = \kappa r$, where the string constant κ describes the amount of
648 energy per unit length. A value of $\kappa \approx 1 \text{ GeV/fm} \approx 0.2 \text{ GeV}^2$ can be obtained
649 from hadron mass spectroscopy [127].

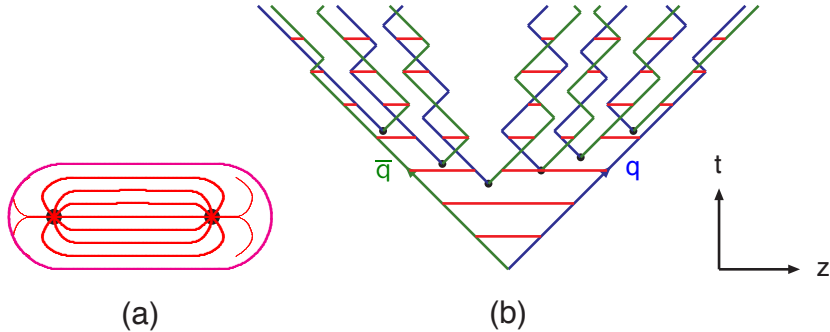


Figure 16: (a) A flux tube spanned between a quark and an antiquark. (b) The motion and breakup of a string system, with the two transverse degrees of freedom suppressed (diagonal lines are (anti)quarks, horizontal ones snapshots of the string field) [127].

650 The evolution of string fragmentation is illustrated schematically on the right
 651 side of Figure 16. This figure is drawn in a light cone presentation, so the initial
 652 quark and antiquark are going to separate directions at the speed of light. The
 653 string between them, illustrated in the figure by the red line, stretches until its
 654 potential energy becomes high enough that it can break, forming a new quark-
 655 antiquark pair. If the original pair was $q\bar{q}$ and the new pair $q'\bar{q}'$, now two new
 656 pairs $q\bar{q}'$ and $q'\bar{q}$ have formed. As these particles are also moving away from each
 657 other, the strings between them can stretch and break, creating yet more pairs.
 658 The process continues until the invariant mass of the system connected by the
 659 string becomes small enough and a final state meson is formed.

660 To mathematically model the string one can use a massless relativistic string
 661 with no transverse degrees of freedom. The gluons are represented as energy and
 662 momentum carrying kinks on the string with incoherent sums of one colour charge
 663 and one anticolour charge. When this string breaks, it is classically required that
 664 the created quark and antiquark are produced at a certain distance if they are to
 665 have any mass or transverse momentum. However, taking into account quantum
 666 mechanics, the pair must be created at one point and then tunnel out to the
 667 classically allowed region. Thus the probability to create a new quark-antiquark
 668 pair becomes proportional to the tunnelling probability [130].

$$P_{\text{tunnelling}} \propto \exp\left(\frac{-\pi m_\perp^2}{\kappa}\right) = \exp\left(\frac{-\pi m^2}{\kappa}\right) \left(\frac{-\pi p_\perp^2}{\kappa}\right), \quad (30)$$

669 where the transverse mass m_\perp is defined as $m_\perp^2 = m^2 + p_\perp^2$. The transverse
 670 momentum is now defined to be transverse to the string axis. This formula gives
 671 flavour-independent Gaussian p_\perp -distribution for the created $q\bar{q}$ pairs.

672 As explained above the string fragmentation would only produce mesons in
 673 the final state, but we know that also baryons are created in the process. In the
 674 string fragmentation model baryon production is included by adding a probability
 675 that a diquark-antidiquark pair is created instead of a quark-antiquark pair when
 676 a string breaks.

677 The kinematics of each string breaking are determined iteratively. Since there
 678 is no natural ordering, the string breaking can be considered in any order and
 679 the answer obtained must be the same. One can start from the q leg and work
 680 one's way to the \bar{q} leg, or vice versa. This give a left-right symmetry of the
 681 string fragmentation. In the Lund model this is taken into account by defining a
 682 symmetric fragmentation function

$$f(z) \propto \frac{1}{z} (1-z)^a \exp\left(-\frac{bm_\perp^2}{z}\right) \quad (31)$$

683 to break the string into a hadron and a remainder system. Here z is the fraction
 684 of light-cone momentum p^+ given to the hadron in the string breaking, m_\perp is the
 685 transverse mass of the hadron and a and b are tuneable parameters of the model.
 686 For heavy quarks this is modified as

$$f(z) \propto \frac{1}{z^{1+bm_Q^2}} (1-z)^a \exp\left(-\frac{bm_\perp^2}{z}\right). \quad (32)$$

687 The process can be thought as follows: first start from the q-leg of a $q\bar{q}$ system
 688 and choose to consider the breaking to new $q'\bar{q}'$ pair closest to this leg. Now the
 689 breaking will produce a hadron $q\bar{q}'$ and a remainder system spanning from $q'\bar{q}$.
 690 Then the process is continued until the \bar{q} -leg is reached. A small detail here is
 691 that in equation (31) it is assumed that the mass of the remainder system is large.
 692 Thus some patching up is needed for the last two hadrons coming from a string.
 693 The patching up is done such that the place where it happens looks as closely like
 694 any other string break as possible.

695 One additional possibility one must consider is that a string can have such a
 696 low mass that it cannot break at all. In this case a single hadron is generated out
 697 of the string and if necessary energy and momentum are exchanged with other
 698 partons in the event.

699 After all the hadrons are produced, the short-lived ones can still decay before
 700 the set of final state particles in the simulation is obtained [125]

701 Cluster model

702 Instead of a string model HERWIG [126] uses a cluster model for hadronisation.
 703 The advantage of cluster models is that they require a smaller number of param-
 704 eters than string models. The model is based on the preconfinement property of

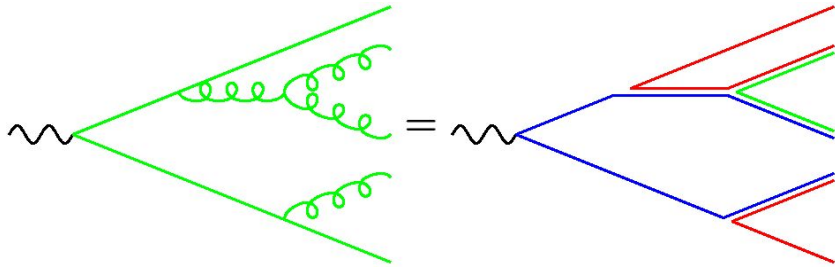


Figure 17: Colour structure of a parton shower to leading order in N_c [127]

705 parton showers, i.e. the colour structure of the shower at any evolution scale Q_0 is
 706 such that colour singlet combinations of partons can be formed with an asymptot-
 707ically universal invariant mass distribution. The invariant mass does not depend
 708 on the initial hard process scale Q , but only on Q_0 and the QCD scale Λ_{QCD} , when
 709 $Q \gg Q_0$ [127].

710 The cluster model starts from transforming all gluons non-perturbatively into
 711 $q\bar{q}$ pairs, which requires that the gluons get a mass, which must be at least twice
 712 the lightest quark mass. After the gluons are transformed into quarks, the adjacent
 713 colour lines can be clustered together to colour singlet states with mesonic quantum
 714 numbers. The momentum of these clusters is defined to be the sum of the momenta
 715 of the clustering partons. The principle of colour-preconfinement states that the
 716 mass distribution of these clusters is independent of the hard scattering process
 717 and its centre-of-mass energy [126].

718 Some of these initial clusters are too heavy to reasonably describe an excited
 719 state of a hadron. These must be split before they are allowed to decay. The
 720 cluster C is split if its mass fulfills the condition [126]

$$M_C^p \geq M_{\max}^p + (m_1 + m_2)^p, \quad (33)$$

721 where $m_{1,2}$ are the masses of the constituents partons of the cluster. M_{\max} and p
 722 are parameters given defined the model. These have to be chosen separately for
 723 clusters containing light, charmed and bottom quarks. When a cluster splits, a pair
 724 of light quarks is generated from the vacuum, which form two new clusters, both
 725 containing one quark from the original cluster and one from the newly generated
 726 pair. The splitting continues until no clusters with masses fulfilling the equation
 727 33 remains.

728 When the clusters are light enough, they decay into final state hadrons. If
 729 the cluster mass is high enough for decaying into a baryon-antibaryon pair, it
 730 can undergo either a mesonic or a baryonic decay. The probabilities of mesonic
 731 and baryonic decays are parameters in the model [126] For a mesonic decay a
 732 quark-antiquark pair is created from the vacuum and for the baryonic decay a

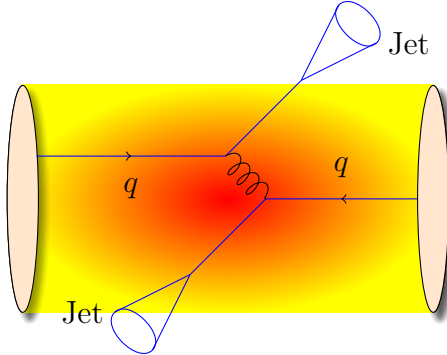


Figure 18: If hard scatterings happen in conjunction with QGP medium the produced jets must traverse the medium. Thus they are subject to interactions with the medium. Note that the dijet pair can be created anywhere within the medium volume and thus the two jets will have differing path lengths through the medium.

diquark-antidiquark pair is made. Then the exact decay products are chosen and the cluster decays isotropically in the rest frame of the cluster. If there are partons produced in the perturbative phase involved in the decay, they retain their original direction in the cluster rest frame, up to some Gaussian smearing. If the cluster mass is too low to decay into a pair of mesons, it decays into the lightest possible hadron and some energy and momentum is exchanged with the adjacent clusters. At the end we are left with the final state hadrons, some of which might still decay until the end of the simulation if they are very short-lived. [126]

1.4.5 Interactions between jet and medium

Let us now look at what happens to jet production in heavy-ion collisions. Figure 18 shows a dijet produced inside QGP medium. High momentum particles are very rare and they are only produced in the initial collisions. In a heavy ion collision, where a QGP medium is formed, the hard scattered quarks and gluons are expected to interact strongly with the medium due to their colour charges and thus lose energy, either through collisions with medium partons, or through gluon bremsstrahlung [6]. This is referred to as jet quenching. Studying the modification of jets inside the medium gives another key approach to constraining the properties of QGP. Modification can be also observed in jet shapes, particle composition, fragmentation, splitting functions and many others.

752 **Discovery of jet quenching via leading hadron suppression**

753 First evidence of jet quenching comes from observing high p_T tracks, i.e. the
754 leading hadrons of jets. In this picture jet quenching in heavy-ion collisions is
755 usually quantified with the nuclear modification factor R_{AA} , which is defined as

$$R_{AA}(p_T) = \frac{(1/N_{AA}^{evt}) dN^{AA}/dp_T}{\langle N_{coll} \rangle (1/N_{pp}^{evt}) dN^{pp}/dp_T} \quad (34)$$

756 where dN^{AA}/dp_T and dN^{pp}/dp_T are the yields in heavy-ion and proton-proton
757 collisions, respectively and $\langle N_{coll} \rangle$ is the average number of binary nucleon-nucleon
758 collisions in one heavy-ion event. The number of binary collisions can be calculated
759 from the Glauber model as shown in Section 1.3.1. From the point of view of direct
760 production at high p_T a heavy-ion collision can be estimated relatively well to be
761 only a series of proton-proton collisions. At low p_T this scaling breaks down as the
762 determining factor in direct production is the number of participants.

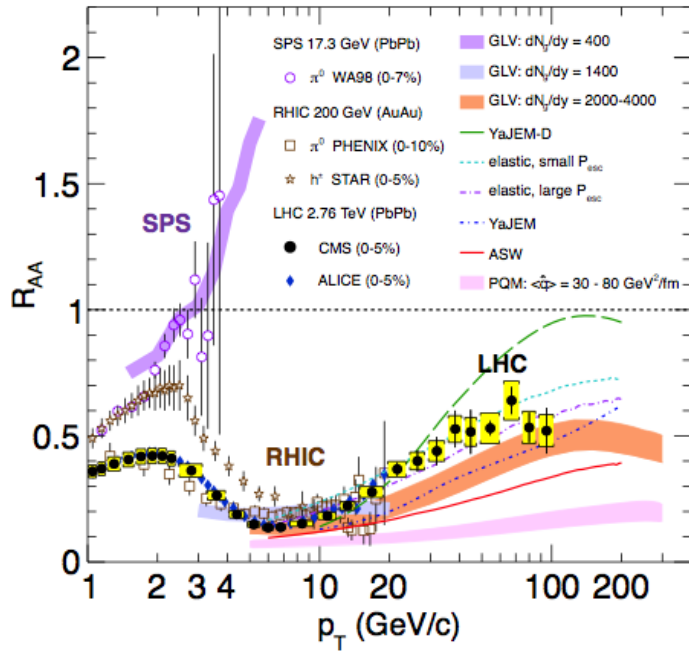


Figure 19: Measurements of the nuclear modification factor R_{AA} in central heavy-ion collisions at three different center-of-mass energies, as a function of p_T , for neutral pions (π^0), charged hadrons (h^\pm), and charged particles [131–135], compared to several theoretical predictions [69, 136–140]. The error bars on the points are the statistical uncertainties, and the yellow boxes around the CMS points are the systematic uncertainties. The bands for some of the theoretical calculations represent their uncertainties [141].

If the medium has no effect on high p_T particles the nuclear modification factor should be 1. As seen in Figure 19 R_{AA} at RHIC and LHC has been observed to be as low as 0.2, which is a clear signal that jet quenching is happening. However, the physical interpretation is not that 80 % of high momentum tracks disappear, rather they are shifted to smaller momenta. The relation between the shift in momentum and R_{AA} depends on the steepness of the dN/dp_T spectra. At LHC energies the spectrum is flatter and thus the same R_{AA} value as in RHIC requires a larger momentum shift, which results from the larger temperature of the medium at LHC.

The reaction plane dependence of inclusive particle R_{AA} demonstrates that energy loss is path length dependent [142], as expected from models. The path length can be affected by collisions centrality and system size. However, the temperature and lifetime of the QGP also changes with changing centrality and system size. Thus to study different path lengths the angle relative to the reaction plane gives the cleanest signal, as the properties of medium remain the same. Additionally it was concluded that there is no suppression for path lengths below $L = 2 \text{ fm}$. Similar indications about path length dependence are given by jet v_2 both at RHIC [143] and at LHC [144, 145].

QED Bremsstrahlung

Many of the energy loss models exploit the analogy between the QCD interaction of parton propagating through the coloured medium and the QED energy loss of electron propagating through material. An electron propagating through matter loses its energy by photon Bremsstrahlung radiation. In the simplest case, each individual scattering center results in a single emission of a photon. This is known as the Bethe-Heitler regime [146]. The energy spectrum of radiated photons dN/dE is, in this case, proportional to $1/E$. However, the Bremsstrahlung photon, can be radiated only when the distance between the scattering centers is larger than the formation length. In the limit, when the scattering centers are closer than the formation length, the Bremsstrahlung process is suppressed. This phenomenon is known as the Landau-Pomeranchuk-Migdal (LPM) [147, 148] suppression. The radiated spectrum in this regime is proportional to $1/\sqrt{E}$.

Lower energy photons are further suppressed by the destructive interference leading to the suppression of Bremsstrahlung photons of $E < \gamma\omega_p$, where ω_p is the plasma frequency of the radiator. This is known as Dielectric suppression. The photon energy distribution in this regime is proportional to the energy of the photon. A schematic view of the effect of these three regimes is shown in Figure 20.

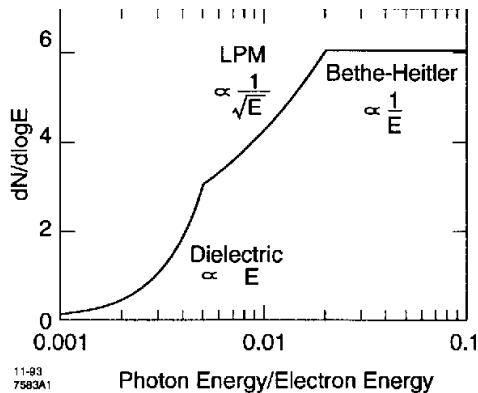


Figure 20: The expected bremsstrahlung spectrum for an electron propagating through material [149]

799 QCD

800 In QCD the radiative energy loss mechanism is given in terms of the transport co-
 801 efficient $\langle \hat{q} \rangle$, which describes the average momentum transfer between the medium
 802 and parton [150]. The exact definition of this depends on the theoretical formalism
 803 used to describe the energy loss mechanism.

804 The simplest energy loss process is elastic QCD scattering off the medium par-
 805 tons. In elastic scatterings the recoil energy of the scattered partons are absorbed
 806 by the thermal medium, which reduces the energy of the initial parton. The mean
 807 energy loss from elastic scatterings can be estimated by

$$\langle \Delta E \rangle_{\text{el}} = \sigma \rho L \langle E \rangle_{\text{1scatt}} \propto L, \quad (35)$$

808 where σ is the interaction cross section and $\langle E \rangle_{\text{1scatt}}$ is the mean energy transfer
 809 of one individual scattering [151]. This assumption holds if the mean energy is
 810 independent of the total energy of the parton (E). The transport coefficient of
 811 elastic scattering, $\langle \hat{q}_{\text{el}} \rangle = \langle \Delta E \rangle / L$, is defined as the mean energy loss per unit path
 812 length.

813 Another energy loss mechanism is medium-induced radiation. In QCD this
 814 radiation is mainly due to the elementary splitting processes, $q \rightarrow qg_r$ and $g \rightarrow gg_r$.
 815 Assuming that the parton is moving with the speed of light radiation energy loss
 816 can be estimated by

$$\langle \Delta E \rangle_{\text{rad}} \propto T^3 L^2, \quad (36)$$

817 where L is the length of the medium and T is its temperature [152]. The differ-
 818 ent exponents of L in equations 35 and 36 indicate that radiative energy loss is
 819 dominant over elastic energy loss.

820 There are several models that attempt to describe the nature of the energy loss
821 mechanism. The most used models can be divided into four formalisms.

822 In the Gyulassy-Levai-Vitev (GLV) [153] opacity expansion model the radiative
823 energy loss is considered on a few scattering centers N_{scatt} . The radiated gluon
824 is constructed by pQCD calculation as summing up the relevant scattering amplitudes
825 in terms of the number of scatterings. Another approach into opacity expansion is the ASW
826 model by Armesto, Salgado and Wiedemann [154].

827 Thermal effective theory formulation by Arnold, Moore and Yaffe (AMY) [155]
828 uses dynamical scattering centers. It is based on leading order pQCD hard thermal
829 loop effective field theory. This model assumes that because of the high temperature
830 of the plasma the strong coupling constant can be treated as small. The parton propagating
831 through the medium will lose energy from soft scatterings and hard scatterings.

833 The above models calculate the energy loss while the parton propagates through
834 the medium, focusing on the pQCD part. The higher twist (HT) approach by Wang
835 and Guo [156] implements the energy loss mechanism in the energy scale evolution
836 of the fragmentation functions.

837 The last category is formed by the Monte Carlo methods. The PYTHIA event
838 generator [157] is widely used in high-energy particle physics. Two Monte Carlo
839 models based on PYTHIA describing the energy loss mechanism are PYQUEN [158]
840 and Q-Pythia [159]. Other Monte Carlo models include JEWEL [160] and Ya-
841 JEM [161].

842 1.4.6 New paradigm of jet Quenching

843 As described in the previous sections the first indications of jet quenching, such
844 as R_{AA} , looked essentially at the leading hadrons of jets, the hard part, ignoring
845 the soft scale part of jet phenomena. However, experimental methods have since
846 improved; jet reconstruction algorithms have become reliable in the LHC era.
847 Instead of the leading hadron we can study the entire jet shower and its structure.
848 In jet observables one must consider what happens to the lost energy. Radiated
849 gluons may end up being clustered with the jet, depending on the radiation angle,
850 the parameters of jet reconstruction and whether the gluon reaches equilibrium
851 with the medium or not. Thus the suppression on the jet level is expected to
852 be smaller. Figure 21 shows jet R_{AA} in central Pb–Pb collisions measured by
853 ALICE,ATLAS and CMS and indeed jet R_{AA} is about 0.5 instead of 0.2.

854 Thus, on the level of the reconstructed jet, energy loss manifests itself as broadening
855 and softening of the jet. This is seen for example in jet-hadron correlations.
856 Figure 22 shows $\Delta\eta$ correlations with the leading jet. $\Delta\phi$ correlations have similar
857 trends. Jets in Pb–Pb are observed to be broader, with the greatest increase in
858 the width for low momentum associated particles. This is consistent with expec-

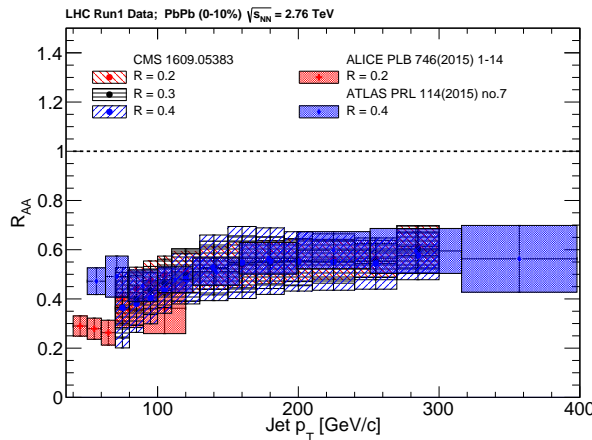


Figure 21: Reconstructed anti- k_T jet R_{AA} from ALICE [162] with $R = 0.2$ for $|\eta| < 0.5$, ATLAS [163] with $R = 0.4$ for $|\eta| < 2.1$, and CMS [164] with $R = 0.2, 0.3$ and 0.4 for $|\eta| < 2.0$. The ALICE and CMS data are consistent within uncertainties while the ATLAS data are higher. The experiments use slightly different methods in selecting jets and subtracting the underlying event contribution. Compared to ALICE and CMS the ATLAS technique could impose a survivor bias and lead to a higher jet RAA at low momenta. Figure from [6]

tations from partonic energy loss. These studies found that the subleading jet was broadened even more than the leading jet, indicating a bias towards selecting less modified jets as the leading jet. Jet hadron correlations have also been studied at RHIC with similar conclusion [165].

863 Phase-space view of the medium modified parton cascade

The new paradigm in jet quenching in heavy-ion collisions involves multi-scale problems [167, 168]. The elementary scattering and the subsequent branching process down to non-perturbative scales are dominated by hard scales in the vacuum as well as in the medium. Soft scales, of the order of the temperature of the medium, characterise the interactions of soft partons produced in the shower with the QGP. Soft scales also rule hadronisation, which is expected to take place in vacuum for sufficiently energetic probes, even though some modifications can persist from modifications of colour flow [169–171]. Understanding the contributions from the different processes to the jet shower evolution in medium and their scale dependence is crucial to constrain the dynamics of jet energy loss in the expanding medium, the role of colour coherence [172], and fundamental medium properties like temperature dependent transport coefficient [173, 174].

Let us now look at medium modification of jets in a $\log(p) - \log(\theta)$ plane

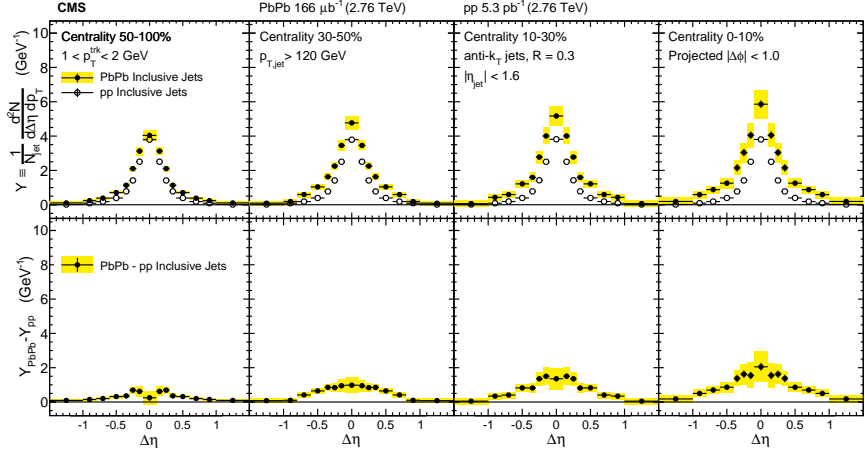


Figure 22: Measurement by CMS [166]. Symmetrized $\Delta\eta$ distributions correlated with Pb–Pb and pp inclusive jets with $p_T > 120 \text{ GeV}$ are shown in the top panels for tracks with $1 < p_T < 2 \text{ GeV}$. The difference between per-jet yields in Pb–Pb and pp collisions is shown in the bottom panels. These measurements indicate that the jet is broadened and softened, as expected. The effect is stronger in more central collisions. $\Delta\phi$ correlations have similar trends.

as shown in [167]. The different momentum and angular scales are subject to different physical phenomena. Figure 23 shows the relevant medium modification phenomena for different regions of the phase space at time t , when a jet propagates through a thermal cloud of temperature T . As in practice jets propagate over a finite path-length L in QCD matter, Figure 23 can be taken as a representation of the distribution of partonic jet fragments at moment $t \approx L$, when the jet escapes the medium. [167]

The region marked as DGLAP is dominated by the primary vacuum splittings explained in section 1.4.2. This region is determined by $\theta > \theta_{\text{vac}}$ with

$$\theta_{\text{vac}} \propto 1/\sqrt{p_T}. \quad (37)$$

Medium-induced parton branching fills the $\log p$ - $\log \theta$ -plane from the bottom up (in p) and from the inside out (in θ). This is because transverse momentum is acquired by Brownian motion in the medium, $k_\perp^2 \propto \hat{q}t$. The formation time constraint $t \geq p/k_\perp^2 \approx p/\hat{q}t$ implies that medium-induced quanta can be formed in the region $p \leq k_{\text{form}}$ where

$$k_{\text{form}}(t) = \hat{q}t^2. \quad (38)$$

For these splittees to survive without further splittings they must have

$$p \geq k_{\text{split}} \approx \alpha_s^2 k_{\text{form}}(t) \approx \alpha_s^2 \hat{q}t^2. \quad (39)$$

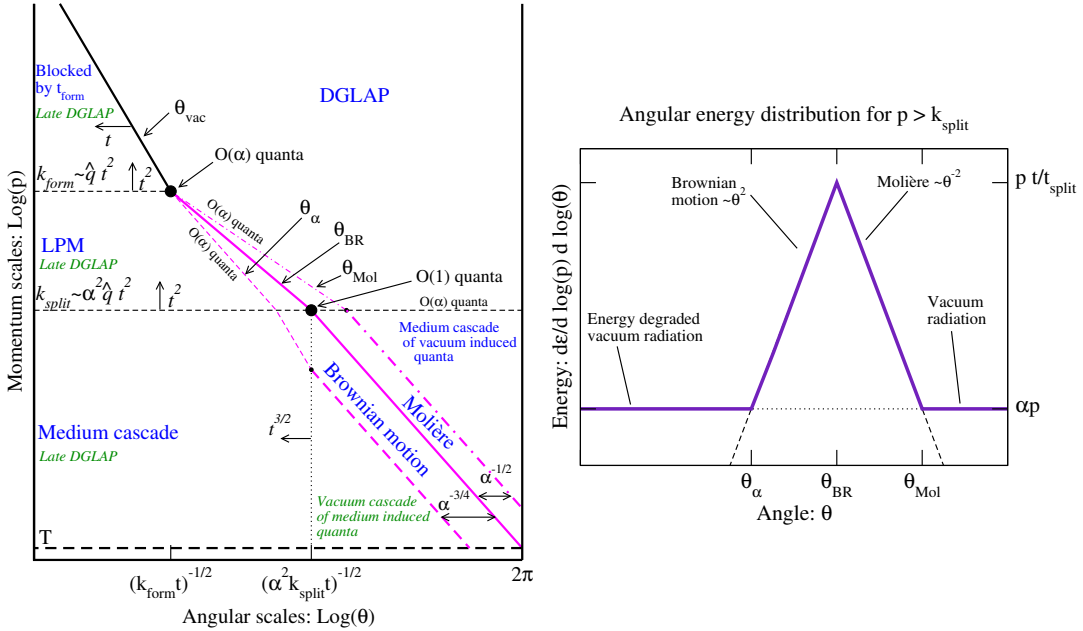


Figure 23: *Left:* Phase space view of dominant contributions in a medium-modified parton cascade. *Right* The distribution of energy as a function of angle for a fixed momentum with $p > k_{\text{split}}$. Large angular scales $\theta > \theta_{\text{Mol}}$ are dominated by DGLAP vacuum radiation from the leading parton at the scale Q . At $\theta < \theta_{\alpha}$ the energy density is dominated by vacuum radiation of the leading parton after it has degraded its energy propagating through the medium. Areas $\theta_{\alpha} < \theta < \theta_{\text{BR}}$ and $\theta_{\text{BR}} < \theta < \theta_{\text{Mol}}$ are dominated by Brownian motion and rare large angle (Molière) scatterings with medium partons [167].

892 Thus the region marked as LPM in Figure 23 is filled by the primary medium-
 893 induced branchings. Fragments with $p \leq k_{\text{split}}$ will have time to split further.
 894 An approximately equal splitting where both splittees get momentum $p/2$ from
 895 the parent will degrade energy the most. These splittees will undergo the next
 896 splitting in an even shorter time scale producing even softer fragments. Momenta
 897 can continue cascading all the way to the thermal scale T of the medium within the
 898 same time scale within which the first splitting occurred. Thus filling the region
 899 marked as Medium cascade in Figure 23. Similarly splittees from vacuum radiation
 900 can cascade inside the medium when they have $p \leq k_{\text{split}}$, filling the bottom right
 901 corner of the $\log p$ - $\log \theta$ -plane.

902 The angular distribution of the medium-induced radiation is driven by two
 903 mechanisms; Multiple soft scatterings give rise to transverse Brownian motion,
 904 which determines the distribution at small angles. The typical angle reached in
 905 the LPM region is

$$\theta_{\text{BR}}(p) \approx \frac{\sqrt{\hat{q}t}}{p}, \text{ for } k_{\text{form}} > p > k_{\text{split}}, \quad (40)$$

906 while in the medium cascade region of the phase space this becomes

$$\theta_{\text{BR}}(p) \approx \left(\frac{T}{p}\right)^{\frac{3}{4}} \quad (41)$$

907 Large angular scales cannot be reached by Brownian motion, but can arise from
908 rare large angle scatterings with partons in the medium, described first by Molière [175].
909 The result is that medium-induced radiation is predominantly located in the
910 bands marked as Brownian motion, where $\theta_\alpha < \theta < \theta_{\text{BR}}$, and Molière, where
911 $\theta_{\text{BR}} < \theta < \theta_{\text{Mol}}$ in Figure 23.

912 The hard parton will naturally continue radiating after it leaves the medium.
913 As there is no longer kinematic limits set by the time scale, the vacuum radiation
914 can extend to smaller angular scales in the phase space. The results is that the
915 regions, where $\theta < \theta_\alpha$, marked as Late DGLAP in Figure 23 will be dominated by
916 the late time vacuum radiation. Naturally also the splittees from medium-induced
917 radiation will undergo the late stage vacuum radiation phase, filling the triangular
918 region with small p and $\theta < \theta_\alpha$.

919 Influence of jet on medium

920 Energy loss of hard partons is well established by experimental observations. Nat-
921 urally energy can't just disappear, but is transferred to daughter partons or the
922 medium. For radiation that stays inside the jet cone energy loss manifests itself
923 as softening and broadening. If a daughter parton loses energy and becomes equi-
924 librated with the medium it may no longer be correlated with the parent parton.
925 This energy would then be distributed at distances far from the jet cone. There is
926 some evidence for out-of-cone radiation by CMS [176], but the interpretation is not
927 clear. Other possible phenomena include the mach cone and Molière scattering,
928 but there is no experimental evidence for these. Evidence for all of these effects
929 is difficult to find as the underlying event gives already a large and fluctuating
930 background. Additionally its unclear how this energy would be different from the
931 underlying event [6].

932 1.5 QGP in Small systems

933 After the existence of QGP in heavy-ion collisions has been established, attention
934 has been turned to small systems. Proton-proton (pp) and proton-Lead ($p\text{-Pb}$)
935 collisions have been studied at LHC and RHIC has studied a host of different
936 collision systems; namely proton-gold ($p\text{-Au}$) [177], deuteron-gold ($d\text{-Au}$) [178–
937 181] and helium³-gold (${}^3\text{He}\text{-Au}$) [182] collisions starting from 2000.

938 Already before the era of modern colliders, collective behaviour in proton-
939 proton collisions was considered by names like Heisenberg, Fermi and Bjorken [7].
940 Eventually there were some experimental searches of QGP in pp and $p\bar{p}$ collisions
941 in E735 at Tevatron [183] and MiniMAX [184]. However no conclusive evidence
942 was found.

943 In the early years of RHIC these small systems were mostly considered as control
944 measurement, for example in constraining nuclear modified parton distribution
945 functions (nPDFs) that determine the initial gluon distributions that determine
946 the first epoch of heavy-ion collisions [185, 186].

947 In 2010 ultrahigh-multiplicity pp collisions were studied at CMS [187]. The
948 study found that particles had a weak but clear preference to be emitted along a
949 common transverse ϕ angle across all rapidities [188]. This seemed like behaviour
950 were similar to AA collisions, but it was argued that it could as well come from
951 momentum correlations present in the earliest moments of the collision.

952 In 2012 LHC ran its first $p\text{-Pb}$ data taking period. Around the same time
953 $d\text{-Au}$ data was re-examined at RHIC. Now it was revealed that most of the flow
954 signatures attributed to hydrodynamic expansion in AA collisions also existed in
955 smaller systems.

956 1.5.1 Collective phenomena

957 The most rugged analysis of collective behaviour concerns the two (or more) particle
958 correlations, often parametrised via the relative azimuthal angle and pseudo-
959 rapidity differences, $\Delta\phi$ and $\Delta\eta$ respectively. Figure 24 shows two-particle cor-
960 relations measurements in Pb-Pb , $p\text{-Pb}$ and pp collisions at the LHC [189]. In
961 Pb-Pb collisions long-range correlations dominate over short-range phenomena.
962 This shows in the two ridges at $\Delta\phi = 0$ and $\Delta\phi = \pi$. At $\Delta\phi \approx \Delta\eta \approx 0$, there is a
963 peak coming from single jet fragmentation. Since the away-side jet can be spread
964 out in $\Delta\eta$, this contribution disappears when compared to the flow contribution
965 at the away side ridge. In $p\text{-Pb}$, and pp the near side peak is more distinguished
966 and the away-side jet contribution starts to show. Still, one can see long-range
967 correlations that seem like flow-like collective behaviour in both systems.

968 In addition to the two particle correlations, correlations have been observed in
969 the form of v_n coefficients both at LHC [190] and at RHIC [177]. The results have

also been described with hydrodynamical models, although the applicability of said models might be questionable, because of the large Reynolds numbers in small systems [191, 192]. Figure 25 shows results for v_2 in different collisions systems at RHIC as measured by PHENIX and Figure 26 shows the eccentricities and the resulting hydrodynamic evolution in the systems. These different systems provide also different initial geometries. d–Au collisions naturally have an ellipsoidal form, while a ^3He –Au collision has a triangular form and thus produces larger triangular flow, v_3 components.

Other observations that produce flow-like results include mass ordered v_2 coefficients [194] and higher order harmonics coming from fluctuations in the initial geometry [190]. Thus all the major collective flow phenomena observed in heavy-ion collisions have been also identified in small systems.

One open question is identifying the point the point, where flow-like correlations end. The question has proved challenging since low multiplicity events are dominated by non-flow phenomena. This makes observations in low multiplicity events model/method dependant. Different methods assess non-flow contributions differently. Thus some methods fail to observe a signal in cases, where others do and it is unclear whether this is true collective motion or it comes from non-flow contributions.

1.5.2 Absence of jet quenching

In A+A collisions, an important confirmation of the standard model comes from the energy loss of high p_T partons traversing the medium, as discussed in Section 1.4.5. Originally the interest in small systems was due to ruling out possible cold nuclear matter effects that might affect the results also in Pb–Pb. In 2003 the jet quenching effect was observed to disappear in d–Au collisions at RHIC [178–181]. This was taken as an indication that no QGP was created. Similarly at LHC no jet modification has been observed in p–Pb collisions. Figure 27

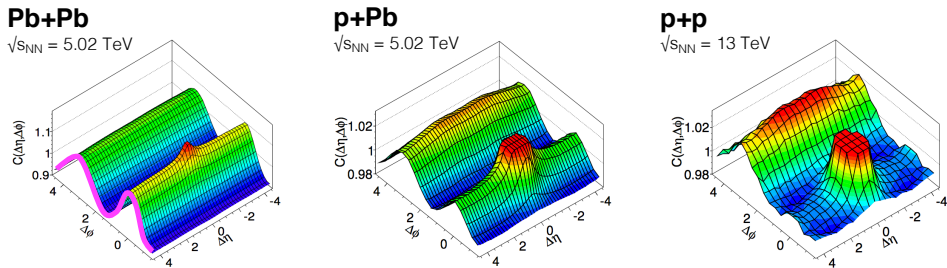


Figure 24: Two-particle correlation results in Pb–Pb, p–Pb, and pp collisions at the LHC [189]

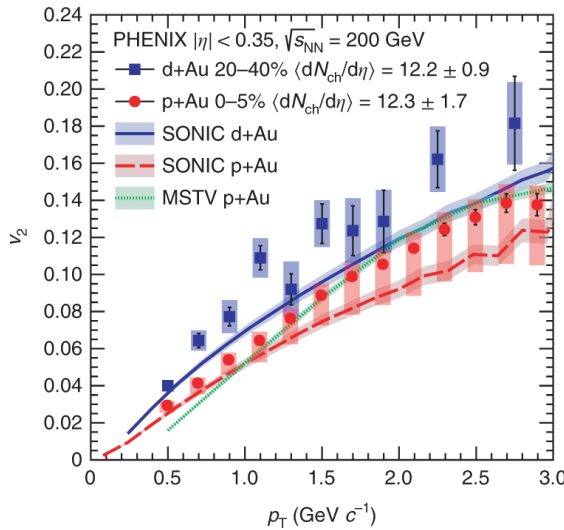


Figure 25: Comparison between hydrodynamic calculations and data from p–Au, d–Au and ${}^3\text{He}$ –Au collisions [193]

997 shows the nuclear modification factor R_{pA} and v_2 in p–Pb collisions as measured
998 at the LHC [195, 196].

999 Now the lack of jet modification seems surprising considering the multitude of
1000 flow observations supporting the existence of QGP in small systems. One possible

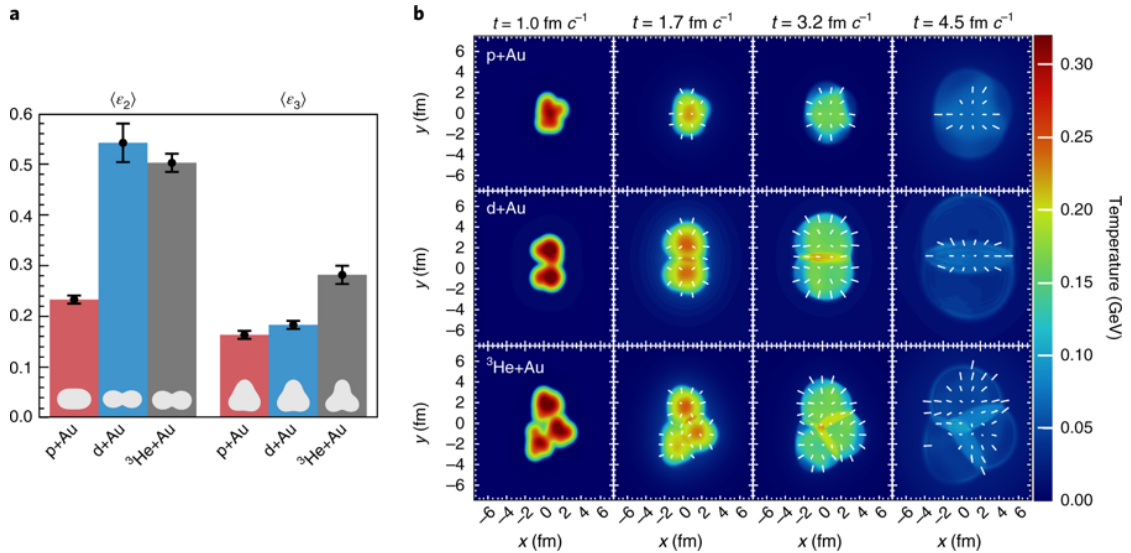


Figure 26: *left:* Eccentricities in different systems. *right:* Calculations of the initial energy density in small collision systems at RHIC and the resulting hydrodynamic evolution [193].

explanation is simply the size of medium. In Pb–Pb collision partons traversing through the medium lose energy to the medium. If the medium is very small there is limited time for interaction with the medium. Reaction plane dependent R_{AA} measurements [142] in Pb–Pb collisions indicated that 2 fm could be the minimum path length required for energy loss.

Some calculations [197–199] indicate that there should be modification in the most central p–Pb collisions, but selecting these in the analysis is complicated [7]. In Pb–Pb collisions most of the particle production comes from the medium and thus the total multiplicity is a good indicator of centrality. However in p–Pb collisions the total multiplicity is smaller and is more strongly influenced by jet phenomena. Events with jets have naturally larger multiplicities and are more likely to be classified as central events.

So far the only observable indicative of jet quenching in p–Pb collisions is the high $p_T v_2$. In heavy-ion collisions this is not explained by hydrodynamics. Instead it is assumed to come from jet quenching with different path lengths through the medium in different directions. In Figure 27 ATLAS [196] and CMS [200] measurements of v_2 in p–Pb and Pb–Pb collisions are shown. The p–Pb results seem to follow a very similar pattern. However, the non-flow effects in this high- p_T region are not fully under control, so the physical interpretation is still under debate.

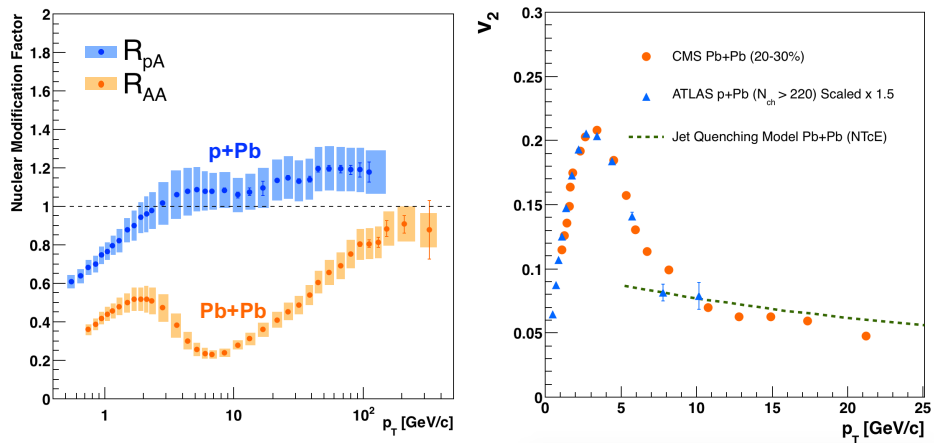


Figure 27: *left:* The nuclear modification factor R_{pA} in p–Pb collisions [195]. Compared to R_{AA} R_{pA} shows no sign of modification. *right:* The v_2 coefficient as a function of p_T in Pb–Pb and p–Pb at the LHC [196, 200]. For shape comparison the p–Pb results have been scaled up by a factor 1.5. The green dotted curve [197] is from a jet quenching calculation where the anisotropy results from the directional dependence of the energy loss, rather than hydrodynamic flow.

1021 1.5.3 Centrality determination in small systems

1022 In lead-lead collisions the total multiplicity of the event is a good indicator of the
 1023 geometric centrality of the collision [86]. In proton-lead collisions the connection
 1024 between multiplicity and centrality is less clear [201]. In p-Pb collisions the im-
 1025 pact parameter is only loosely correlated to N_{part} or N_{coll} . Hence, although one
 1026 uses traditionally the term centrality to refer to these measurements, the relevant
 1027 parameters are N_{part} and N_{coll} [201].

1028 As in Pb-Pb collisions the Glauber model [82] is generally used to calculate
 1029 geometrical quantities of p-Pb collisions. In this model, the impact parameter b
 1030 controls the average number of participating nucleons N_{part} and the corresponding
 1031 number of collisions N_{coll} . It is expected that variations of the amount of matter
 1032 overlapping in the collision region will change the number of produced particles,
 1033 and parameters such as N_{part} and N_{coll} have traditionally been used to describe
 1034 those changes quantitatively, and to relate them to pp collisions. Figure 28 shows
 1035 the measured V0A amplitude distribution in ALICE and the best NBD Glauber
 1036 fit to the distribution [201].

1037 The problem in p-Pb collisions is that fluctuations in multiplicity coming from
 1038 for example hard scatterings are of the same order as the differences in multiplicity
 1039 between centrality classes. In Pb-Pb collisions these multiplicity fluctuations
 1040 have little influence on the centrality determination as the range of N_{part} or N_{coll} is
 1041 large and both $P(M|N_{\text{part}})$ and $P(M|N_{\text{coll}})$ converge quickly to a Gaussian with

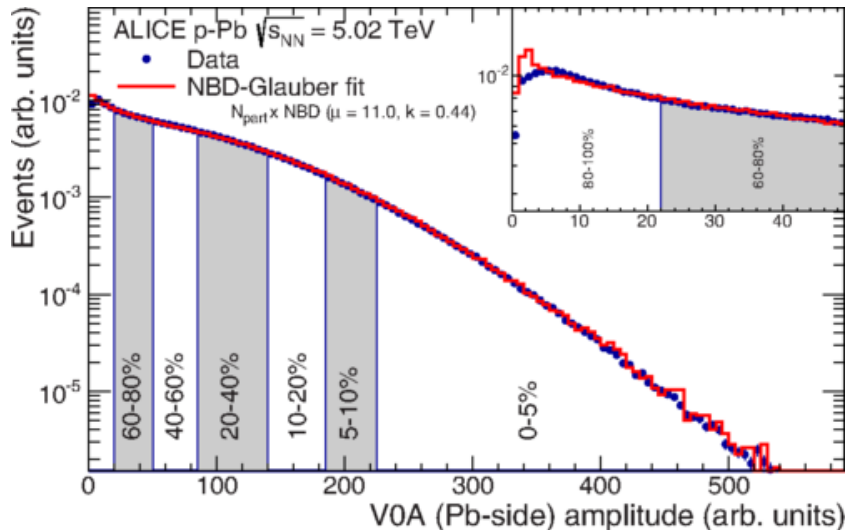


Figure 28: Distribution of the sum of amplitudes in the V0A hodoscopes (Pb-going), as well as the NBD-Glauber fit. Centrality classes are indicated by vertical lines. The inset shows a zoom-in on the most peripheral events. [201]

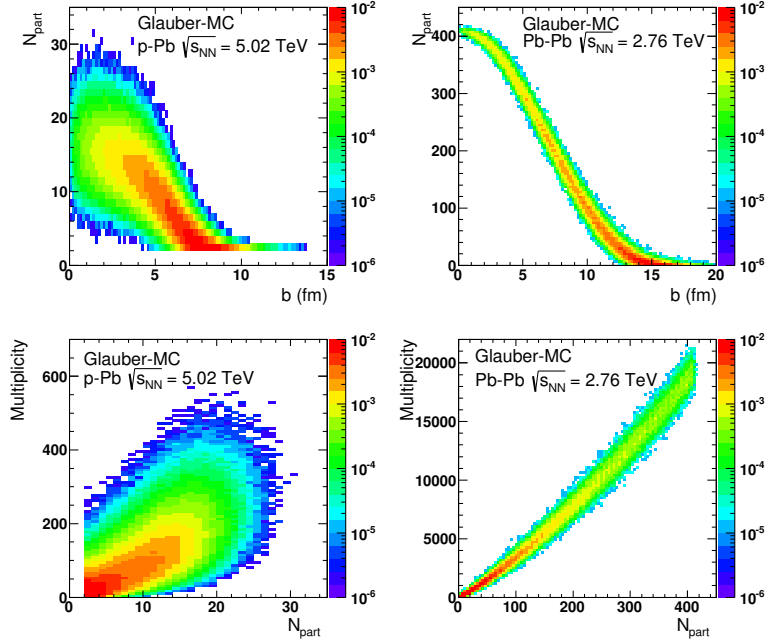


Figure 29: Top: Scatter plot of number of participating nucleons versus impact parameter; Bottom: Scatter plot of multiplicity versus the number of participating nucleons from the Glauber fit for V0A. The quantities are calculated with a Glauber Monte Carlo of p-Pb (left) and Pb-Pb (right) collisions. [201]

a small width relative to the range of $N_{\text{part}}/N_{\text{coll}}$. This is illustrated in Figure 29.
 In practice selecting high multiplicity in p-Pb one chooses not only large average
 N_{part} , but also positive multiplicity fluctuations leading to deviations from the
 binary scaling of hard processes. These fluctuations are partly related to qualitatively
 different types of collisions. High multiplicity nucleon-nucleon collisions
 show a significantly higher mean transverse momentum. They can be understood
 either as harder collisions with larger momentum transfer Q^2 or as nucleon-nucleon
 collisions where multiple parton-parton interactions (MPI) take place.

Of particular interest are estimators from kinematic regions that are causally disconnected after the collision. The measurement of a finite correlation between them unambiguously establishes their connection to the common collision geometry. Typically these studies are performed with observables from well separated pseudorapidity (η) intervals, e.g. at zero-degree (spectators, slow-nucleons, deuteron break-up probability) and multiplicity in the rapidity plateau.

One centrality selection that is argued not to induce a bias on the binary scaling of hard processes is provided by the energy measurement with the Zero Degree Calorimeters (ZDC) in ALICE, due to their large η -separation from the central

1059 barrel detectors. They detect the "slow" nucleons produced in the interaction by
1060 nuclear de-excitation processes or knocked out by wounded nucleons [202].

1061 Additional kinematic biases exist for events containing high- p_T particles, which
1062 arise from the fragmentation of partons produced in parton-parton scattering with
1063 large momentum transfer. Their contribution to the overall multiplicity increases
1064 with increasing parton energy and thus can introduce a trivial correlation between
1065 the centrality estimator and the presence of a high- p_T particle in the event. For
1066 very peripheral collisions, the multiplicity range that governs the centrality for the
1067 bulk of soft collisions can represent an effective veto on hard processes. For the
1068 nuclear modification factor this would lead to $R_{\text{pPb}} < 1$ [201].

1069 2 Experimental Setup

1070 2.1 CERN

1071 The European Organization for Nuclear Research (CERN), established in 1954, op-
1072 erates the largest particle physics laboratory in the world. In 2019 CERN consists
1073 of 22 member states. Additionally CERN has contacts with a number of associate
1074 member states and various individual institutions. The laboratory, also referred
1075 to as CERN, itself is located near Geneva at the border of France and Switzerland
1076 employs about 2500 people. Additionally some 12000 visiting scientists from over
1077 600 institutions in over 70 countries come to CERN for their research. [203]

1078 The laboratory includes a series of accelerators, which are used to accelerate
1079 the particle beams used. A schematic view of the complex as of 2019 is shown
1080 in Figure 30. In the framework of this thesis the most important component is
1081 the Large Hadron Collider (LHC), the largest collider in the world. LHC will be
1082 discussed in more detail in Section 2.2. Other accelerators in the series are used
1083 to inject the particle beams into LHC, but they are also used in itself for various
1084 experimental studies.

1085 The second largest accelerator is the super proton synchrotron (SPS). It is the
1086 final step before the particle beam is injected into LHC. Commissioned in 1976, it
1087 was the largest accelerator at CERN until the the Large Electron-Positron Collider
1088 (LEP) was finished in 1989. Originally it was used as a proton-antiproton collider
1089 and as such provided the data for the UA1 and UA2 experiments, which resulted in
1090 the discovery of the W and Z bosons [205]. At the moment there are several fixed
1091 target experiments utilising the beam from the SPS. These study the structure
1092 (COMPASS citeCOMPASS) and properties (NA61/SHINE [206]) of hadrons, rare
1093 decays of kaons (NA62 [207]) and radiation processes in strong electromagnetic
1094 fields (NA63 [208]). Additionally the AWAKE [209] and UA9 [210] experiments
1095 are used for accelerator research and development.

1096 The third largest accelerator in CERN is the proton synchrotron (PS). Ca-
1097 pable of accelerating beams up to an energy of 25 GeV PS provides the beam to
1098 SPS. Additionally PS has experiments for studying strong force (DIRAC [211]),
1099 the effect of cosmic rays on cloud formation (CLOUD [212]) and neutron-nucleus
1100 interactions (nTOF [213]).

1101 Additionally PS provides the beam to the antiproton decelerator (AD), which
1102 uses the beam and a block of metal to produce antiprotons. These are then
1103 decelerated in AD into a useful low-energy beam, which is provided to a host of
1104 experiments studying the properties of antimatter.

1105 PS gets proton beams from LINAC2 through BOOSTER and ion beams from
1106 LINAC3 through LEIR. From BOOSTER beams are also provided to the On-Line
1107 Isotope Mass Separator (ISOLDE). ISOLDE directs the beam into thick targets

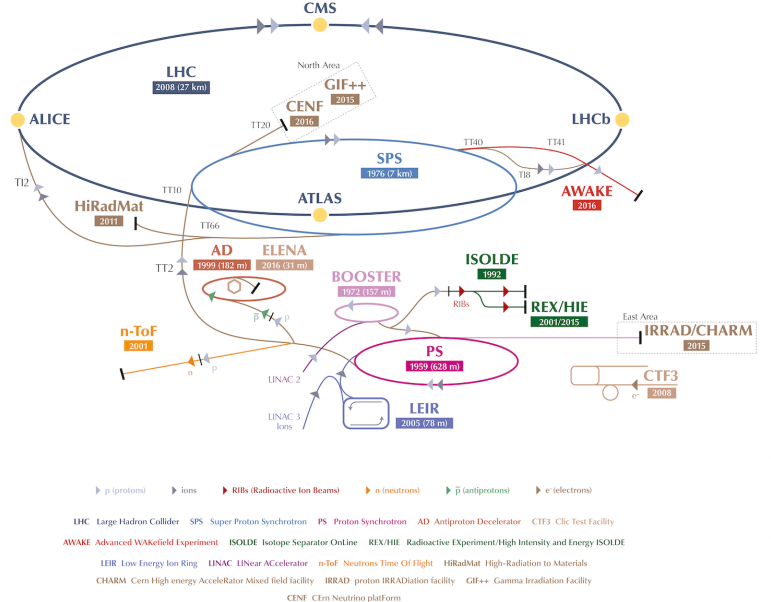


Figure 30: A schematic view of the accelerator complex at CERN. Before particles can be injected into the LHC they require a series of accelerators with increasing size. Until 2018 protons started their journey in LINAC2 (Linear Accelerator) and continue through the Booster, Proton Synchrotron (PS) and Super Proton Synchrotron (SPS). Between 2019 and 2020 LINAC2 will be replaced by LINAC4. [204]

to produce low energy beams of radioactive nuclei. These beams are used to study the properties of even the most exotic of atomic nuclei in a host of experiments.

More information of the various experiments at CERN can be found online in [214].

2.2 Large Hadron Collider

The Large Hadron Collider (LHC) [215, 216] with its circumference of 26.7 km is the largest accelerator at CERN and the largest particle collider ever built. The LHC is designed to accelerate protons up to an energy of 8 TeV and lead ions up to center of mass energies of 5.02 TeV per nucleon. The design luminosity of the LHC is $10^{34} \text{ cm}^{-2}\text{s}^{-1}$. In 2017 it achieved a record peak luminosity of $2 \cdot 10^{34} \text{ cm}^{-2}\text{s}^{-1}$ which was also reached in 2018. For lead beams luminosities of up to $6 \cdot 10^{27} \text{ cm}^{-2}\text{s}^{-1}$ were reached in 2018. All this is achieved with a ring consisting of 1232 superconducting dipole magnets that keep particles in orbit.

1121 The LHC receives beams with energies of 450 GeV from the SPS. In the LHC
1122 the particles are accelerated through the use of radio-frequency (RF) cavities.
1123 Electromagnetic waves become resonant and build up inside the cavity. As they
1124 consist of electromagnetic waves, the field in the RF cavity oscillates. Charges
1125 passing through the cavity feel the overall force and are pushed forward along the
1126 accelerator. Particles must enter the cavity at the correct phase of oscillation to
1127 receive a forward push. When timed correctly, the particles will feel zero acceler-
1128 erating voltage when they have exactly the correct energy. Particles with higher
1129 energies will be decelerated and particles with lower energies will be accelerated.
1130 This focuses particles in distinct bunches. The RF oscillation frequency at the
1131 LHC is 400.8 MHz. Thus RF "buckets" are separated by 2.5 ns. However only 10
1132 % are actually filled with particles, so the bunch spacing in the LHC is 25 ns, at
1133 a bunch frequency of 40 MHz. [215]

1134 With 7 TeV proton beams the dipole magnets used to bend the beam must
1135 produce a magnetic field of 8.33 T. This can be only achieved through making
1136 the magnets superconducting, which requires cooling them down with helium to a
1137 temperature of 1.9 K. The 1232 dipole magnets make up roughly 2/3 of the LHC
1138 circumference. The remaining part is made up of the RF cavities, various sensors
1139 and higher multipole magnets used to keep the beam focused. The most notable
1140 of these are the 392 quadrupole magnets. [215]

1141 The LHC is divided into octants, where each octant has a distinct function.
1142 Octants 2 and 8 are used to inject beam into the LHC from SPS. The 2 beams
1143 are crossed in octants 1,2,5 and 8. The main experiments are built around these
1144 crossing points. Octants 3 and 7 are used for beam cleansing. This is achieved
1145 through collimators that scatter particles with too high momentum or position
1146 offsets off from the beam. The RF cavities used for acceleration are located in
1147 octant 4 and octant 6 is used for dumping the beam. The beam dump is made
1148 up of two iron septum magnets, one for each beam, that will kick the beam away
1149 from machine components into an absorber when needed.

1150 2.2.1 LHC experiments

1151 As of 2018 there are four main experiments at the LHC; ALICE [217], ATLAS [218],
1152 CMS [219] and LHCb [220] and three smaller ones LHCf [221], TOTEM [222] and
1153 MoEDAL [223]. ALICE will be covered in detail in Section 2.3.

1154 ATLAS (A Toroidal LHC ApparatuS) [218] and CMS (Compact Muon Solenoid) [219]
1155 are the two largest experiments at the LHC. They are both multipurpose exper-
1156 iments designed to be sensitive to many different possible new physics signals,
1157 such as extra dimensions and dark matter particles. The biggest discovery made
1158 by these so far is the discovery of the Standard Model Higgs boson, which was
1159 simultaneously published by the experiments in 2012 [224, 225].

1160 The LHCb (LHC beauty) experiment [220] is made for studying the bottom
1161 (beauty) quark. Main physics goals of the LHCb include the measurement of the
1162 parameters of CP violation with decays of hadrons containing the bottom quark.
1163 One of the most important results published by LHCb is the first measurement of
1164 $B_s^0 \rightarrow \mu^+ \mu^-$ decay, which was found to be in line with the Standard Model.

1165 In addition to the four large experiments there are three smaller experiments
1166 along the LHC ring. LHCf (LHC forward) [221] is located at interaction point 1
1167 with ATLAS. It aims to simulate cosmic rays by the particles thrown forwards by
1168 the collisions in ATLAS.

1169 TOTEM (TOTal Elastic and diffractive cross section Measurement) is located
1170 near the CMS experiment at point 5. This allows it to measure particles emerging
1171 from CMS with small angles. The main goals is to measure the total, elastic and
1172 inelastic cross-sections in pp collisions [222].

1173 The MoEDAL (Monopole and Exotics Detector At the LHC) experiment [223]
1174 is located at the interaction point 8 together with the LHCb experiment. MoEDAL
1175 tries to measure signatures of hypothetical particles with magnetic charge, mag-
1176 netic monopoles.

1177 2.3 ALICE

1178 ALICE (A Large Ion Collider Experiment) [226] is the dedicated heavy ion ex-
1179 periment at the LHC. ALICE was designed to cope with the expected very high
1180 multiplicity environment of heavy ion collisions. The design allows measurement
1181 of a large number of low momentum tracks. The different detector subsystems are
1182 optimised to provide high momentum resolution and excellent particle identifica-
1183 tion capabilities over a broad range of momentum.

1184 A schematic view of the ALICE detector in 2018 is presented in Figure 31.
1185 This section will go through the composition of ALICE as it has been during run 2
1186 between 2014 and 2018. The detector will go through significant upgrades during
1187 Long Shutdown 2 (LS2) in 2019-2020.

1188 As in all the major high energy physics experiments the positioning of the de-
1189 tectors follows a layered structure. Closest to the interaction point are the tracking
1190 detectors. The main task of these detectors is to locate the position of the pri-
1191 mary interaction vertex accurately and to record the tracks of charged particles.
1192 To achieve this they need a very good spatial resolution close to the interaction
1193 point. Tracking detectors do not significantly alter the tracks of traversing parti-
1194 cles. Thus they can be located in the innermost layers.

1195 Calorimeters are designed to stop particles hitting them and thus use the ab-
1196 sorption to measure the energy of the particles. Thus they must be located behind
1197 the tracking detectors. ALICE has two separate calorimeter systems, the elec-
1198 tromagnetic calorimeters measure mainly electrons and photons, while the muon

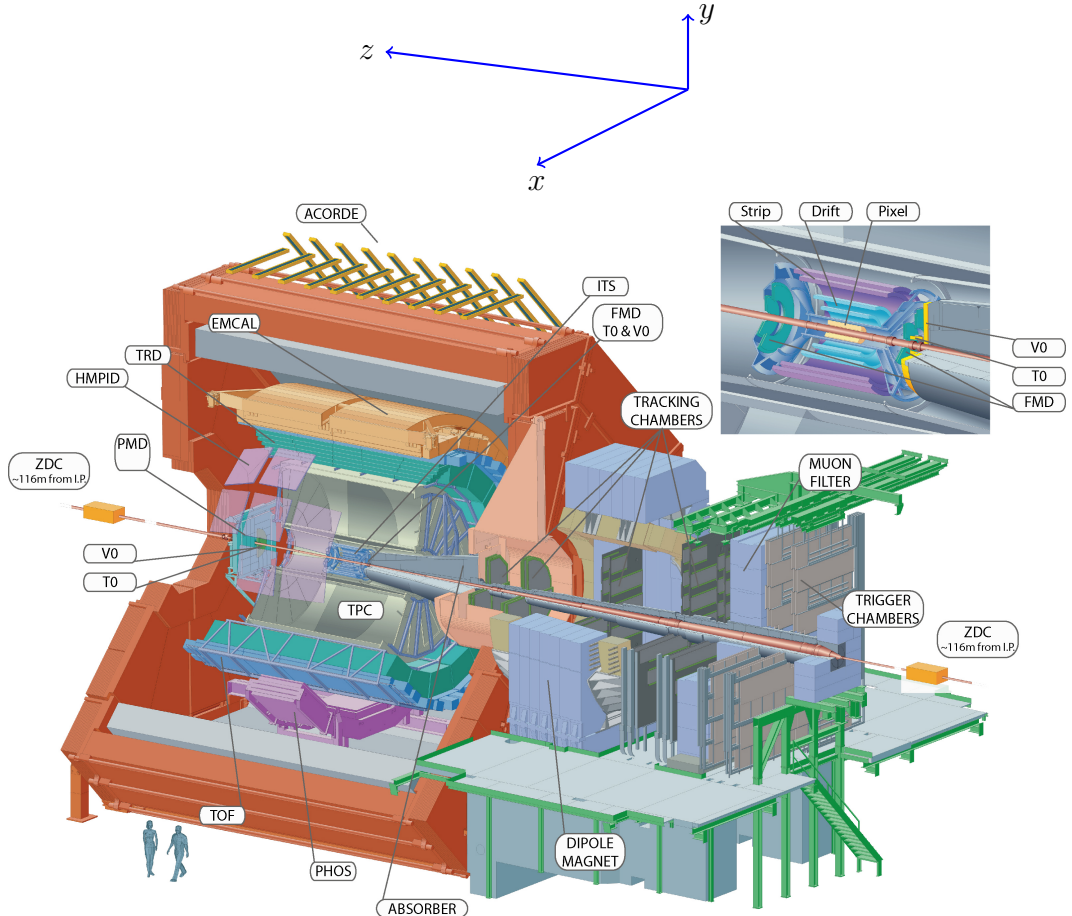


Figure 31: Schematic view of the ALICE detector with the definition of coordinates. The positive direction of z is also referred to as the A side and the negative direction as the C side.

₁₁₉₉ detection system measures muons.

₁₂₀₀ 2.3.1 Tracking

₁₂₀₁ The main design guideline for the tracking detectors in ALICE was the require-
₁₂₀₂ ment to have good track separation and high granularity in the high multiplicity
₁₂₀₃ environment of heavy ion collisions. Before the LHC started heavy ion runs the
₁₂₀₄ wildest estimates put the particle density at 8000 charged particles per unit of ra-
₁₂₀₅ pidity [226]. In reality the particle density turned out to be significantly smaller,
₁₂₀₆ about 1600 charged particles per rapidity unit [227].

₁₂₀₇ The main tracking detector in ALICE is the Time Projection Chamber
₁₂₀₈ (TPC) [228]. TPS is discussed in more detail in Section 2.3.2

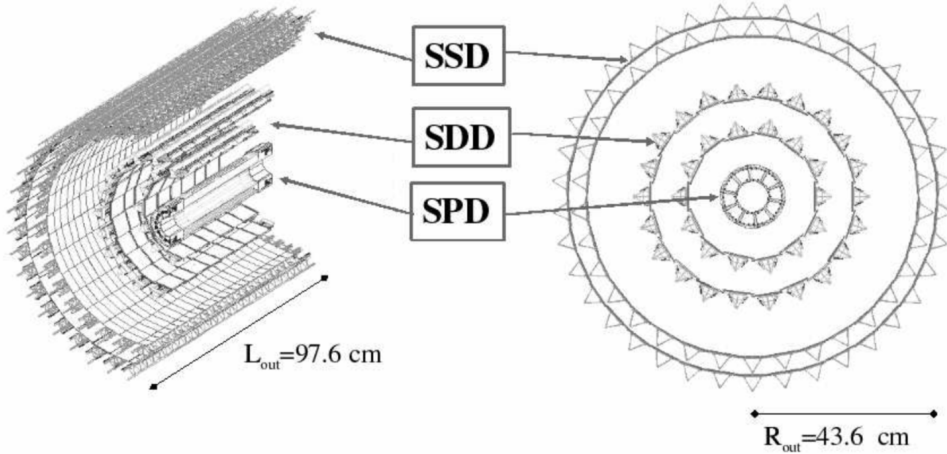


Figure 32: Schematic view of ALICE Inner Tracking System

1209 Between TPC and the beam pipe there is an array of six layers of silicon
 1210 detectors, called the inner tracking system (ITS) [229]. The main tasks of the
 1211 ITS are to locate the primary vertex with a resolution better than $100 \mu m$, to
 1212 reconstruct the secondary vertices from decaying particles, to track and identify
 1213 particles with momenta below 200 MeV and to compliment the momentum and
 1214 angle measurements of TPC. During long shutdown 2 in 2019-2020 the entire ITS
 1215 will be replaced [230]. As of 2018 the two innermost layers are made of the silicon
 1216 pixel detector (SPD). As it is the closest detector to the interaction point it requires
 1217 a very high spatial resolution. Thus the choice of pixel technology is natural. In
 1218 heavy ion collisions the particle density is around 50 particles per cm^2 .

1219 The next two layers together are the silicon drift detector (SDD). The layers
 1220 are made out of homogeneous neutron transmutation doped silicon, that is ionized
 1221 when a charged particle goes through the material. The generated charge then
 1222 drifts to the collection anodes, where it is measured. The maximum drift time in
 1223 SDD is about $5 \mu s$. This design gives very good multi-tracking capabilities and
 1224 provides two out of the four dE/dx samples in the ITS.

1225 The two remaining layers in the ITS are the silicon strip detector (SSD). The
 1226 strips work in a similar way as silicon pixels, but by itself one layer only provides
 1227 good resolution in one direction. Combining two crossing grids of strips provides 2
 1228 dimensional detection. Each charged particle will hit two intervening strips. The
 1229 position of the hit can be deduced from the place where the strips cross each other.

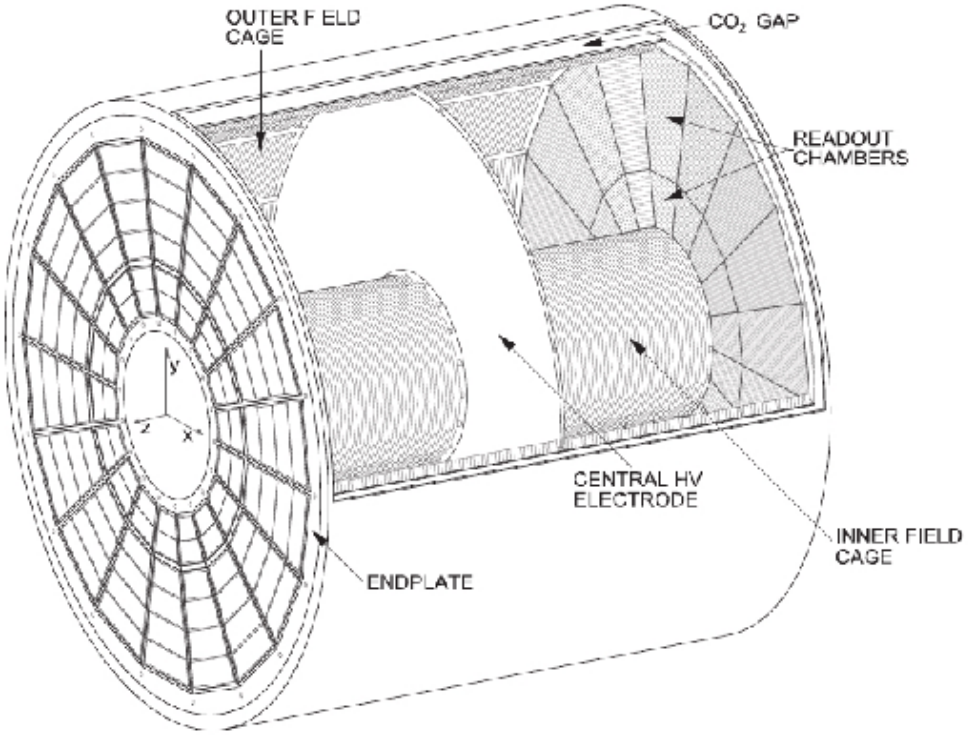


Figure 33: Schematic view of ALICE Time Projection Chamber

1230 2.3.2 TPC

1231 The time projection chamber (TPC) is a cylindrical detector filled with 88 m^3 of
1232 Ne – CO_2 (90/10 %) gas mixture. The gas is contained in a field cage that provides
1233 an uniform electric field of 400 V/cm along the z-axis. The gas content and field
1234 strength have been chosen for optimised charge transport, signal amplification and
1235 transparency for traversing particles [231] Charged particles traversing through
1236 the TPC volume will ionise the gas along their path. This liberates electrons that
1237 drift towards the end plates of the cylinder. A schematic of the TPC is shown in
1238 Figure 33.

1239 The field cage is separated into two detection volumes by the central high
1240 voltage electrode. Both sides have a drift length of 2.5 m and inner and outer
1241 diameters of 1.2 m and 5 m respectively. To provide the uniform electric field of
1242 400 V/cm the central electrode must provide a potential of 100 kV . The maximum
1243 time required for electrons to drift through the chamber is about $90\text{ }\mu\text{s}$.

1244 When electrons reach the end of the main cylinder they enter the readout
1245 chambers. The readout section of both sides consists of 18 outer chambers and

1246 18 inner chambers. Each of them is made of multiwire proportional chambers
1247 with cathode pad readouts. This design has been used in many TPCs before.
1248 During LS2 in 2019-2020, the multiwire chambers will be replaced by Gas Electron
1249 Multipliers (GEMs, see Section 2.4).

1250 **2.3.3 Particle identification**

1251 One guiding principle in the design of ALICE was to achieve good particle iden-
1252 tification (PID) over a large part of phases space and for several different particle
1253 types. In ALICE there are several detectors taking part in the identification of
1254 particles. In addition to the specific particle identification detectors, the general
1255 purpose tracking detectors can be used for identification through the use of specific
1256 energy loss dE/dx of charged particles traversing through a medium and the tran-
1257 sition radiation emitted by charged particles when crossing the boundary between
1258 two materials.

1259 Energy loss measurements are provided by the last four layers of the ITS de-
1260 tector, i.e. the SDD and the SSD, thanks to their analog readout [232]. ITS can
1261 provide particle identification in the low p_T region, up to 1 GeV, and pions re-
1262 constructed in the standalone mode can be identified down to 100 MeV. Similar
1263 to ITS the TPC detector provides specific energy loss measurements. TPC can
1264 identify charged hadrons up to p_T 1 – 2 GeV as well as light nuclei, He3 and He4,
1265 providing the majority of PID information for ALICE.

1266 One of the particle identification detectors is the transition radiation detector
1267 (TRD) [233]. Its main task is identifying electors with momenta larger than 1 GeV.
1268 Transition radiation is produced when highly relativistic particles traverse the
1269 boundary between two media having different dielectric constants. The average
1270 energy of the emitted photon is approximately proportional to the Lorentz factor γ
1271 of the particle, which provides an excellent way of discriminating between electrons
1272 and pion. ALICE TRD is made of a composite layer of foam and fibres. The
1273 emitted photons are then measured in six layers of Xe/CO₂ filled time expansion
1274 wire chambers.

1275 The time of flight (TOF) detector [234] uses a very simple physics principle,
1276 i.e. calculating the velocity of the particle using the time of flight between two
1277 points. Combining this with the momentum of particle, obtained from the tracking
1278 detectors, one can calculate the mass of the particle, which identifies particles. The
1279 TOF detector consists of multigap resistive wire chambers. These are stacks of
1280 resistive plates spaced equally. They allow time of flight measurements in large
1281 acceptance with high efficiency and with a resolution better than 100 ps.

1282 The third specific particle identification detector is the high momentum particle
1283 identification (HMPID) detector [235]. The HMPID uses a ring imaging Cherenkov
1284 counter to identify particles with momenta larger than 1 GeV. Particles moving

1285 through a material faster than the speed of light in the material will produce
1286 Cherenkov radiation. The velocity of the particle determines the angle at which
1287 the radiation is emitted. Measuring this angle gives the velocity of the particle.
1288 This can be again used to calculate the mass of the particle, if the momentum is
1289 known. In HMPID the material is a liquid radiator and the photons are measured
1290 with multiwire proportional chambers in conjunction with photocathodes.

1291 2.3.4 Electromagnetic Calorimeter

1292 Calorimeters are designed to measure the energy of particles. Electromagnetic
1293 calorimeters specialise in detecting particles that interact primarily through the
1294 electromagnetic interaction, namely photons and electrons. They are required in
1295 many neutral meson [236] and direct photon [237] analyses. In addition the energy
1296 information enhances jet measurements [238], as some of jet fragments can't be
1297 detected with trackers.

1298 ALICE has two electromagnetic calorimeters, the photon spectrometer
1299 (PHOS) [239] and the electromagnetic calorimeter (EMCal) [240]. PHOS is a
1300 homogeneous calorimeter that consists of scintillating PbWO_4 crystals, which
1301 generate a bremsstrahlung shower and produce scintillation light. The energy of
1302 the particle determines the amount of light produced. To improve the charged
1303 particle rejection, PHOS includes a charged particle veto detector (CPV) [239].
1304 PHOS is built to have a very fine granularity, making it well suited for measuring
1305 direct photons and neutral mesons.

1306 In comparison to PHOS, EMCal has coarser granularity, but a significantly
1307 larger acceptance, making it suitable for jet physics. The acceptance of EMCal in
1308 the azimuthal angle is $80 \text{ deg} < \phi < 187 \text{ deg}$. During long shutdown 1 in 2013-2015,
1309 EMCal was extended with the di-jet calorimeter (DCal) [241], giving an additional
1310 acceptance region of $260 \text{ deg} < \phi < 320 \text{ deg}$. This provides partial back-to-back
1311 coverage.

1312 EMcal is segmented into 10 full size super modules (SM), 5 for A side and 5 for
1313 C side, and two 1/3 sized SMs, one for each side. This segmentation can be seen
1314 in Figure 34. Each SM is divided into 24 strips, each covering full η (24 towers)
1315 and 2 towers in η . Each strip is composed of 2×2 tower modules. Thus each
1316 full size super module includes 1152 towers and in total the EMCal is made up of
1317 12288 towers.

1318 The build of individual towers is shown in Figure 35. Each tower is built up
1319 from 76 alternating layers of 1.44 mm Pb and 77 layers of 1.76 mm polystyrene base
1320 injection moulded scintillator. The lead tiles produce the shower and scintillator
1321 tiles the light. Each tower scintillator is equipped with reflectors on all sides
1322 to provide better gain and keep the four towers inside one module isolated. The
1323 scintillation photons produced in the active volume of the tower are collected by 36

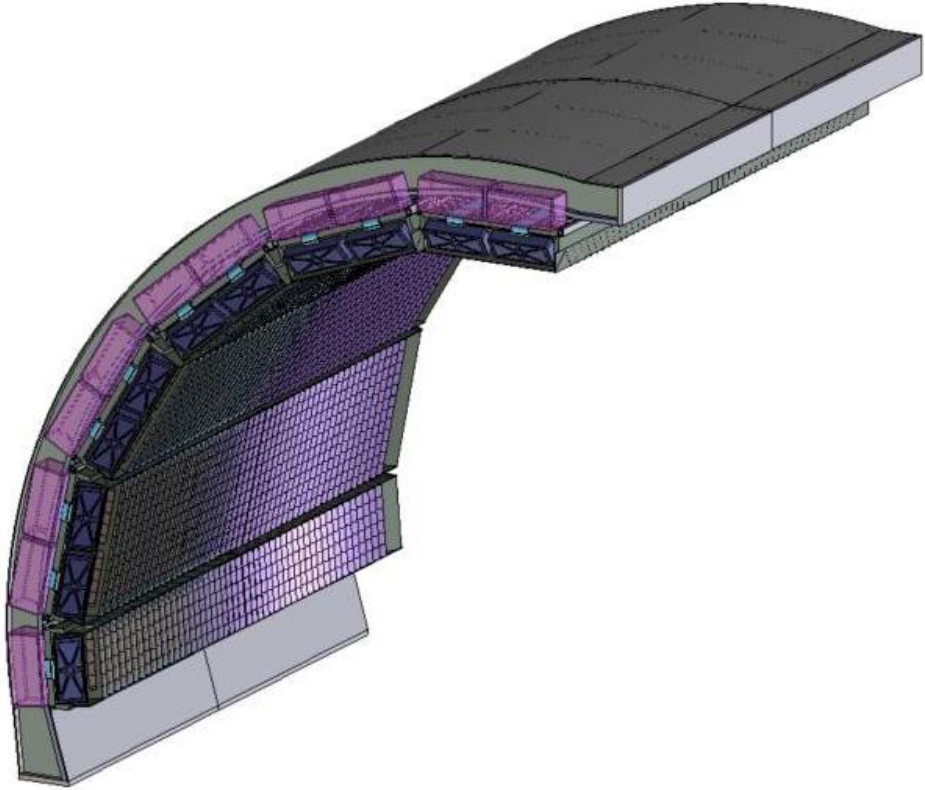


Figure 34: The EMCal detector arc, where the segmentation into 10 full size and 2 $\frac{1}{3}$ -sized (5 and 1 per side) supermodules can be seen.

1324 longitudinally placed wave length shifting light guide fibres. The light is eventually
1325 directed to the Avalanche Photo Diodes (APD) for readout.

1326 2.3.5 Forward and trigger detectors

1327 ALICE includes a few small and specialised detectors of importance. The event
1328 time is determined with very good precision (< 25 ns) by the T0 detector [242].
1329 T0 consists of two sets of Cherenkov counters that are mounted around the beam
1330 pipe on both sides of the interaction point. T0 gives the luminosity measurement
1331 in ALICE.

1332 Another small detector in the forward direction is the V0 detector [242]. This
1333 consists of two arrays of segmented scintillator counters located at $-3.7 < \eta <$
1334 -1.7 and $2.8 < \eta < 5.1$. V0 is used as a minimum bias trigger and for rejection
1335 of beam-gas background. Particle multiplicity in the forward direction can be
1336 related to the event centrality. Thus V0 is the main detector used in centrality

THE EMCAL Module Components

Containment: 88 parts

- 1) Back (holes: 144 thru for fibers + springs + mech. support), 1
- 2) Compression (holes: 144 thru for fibers + springs), 1
- 3) Front Plate (holes: 144 thru for fibers + springs + mech. support), 1
- 4) 5) Plungers (10)
- 6) Belleville washers (75)

Tensioning and Insulation:

40 parts

- 7) Stainless steel straps (4)
- 8) Screws (24)
- 9) Flanges (8)
- 10) Light tight stickers (4)

Sandwich:

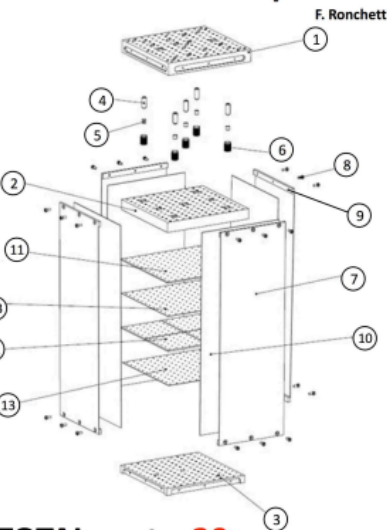
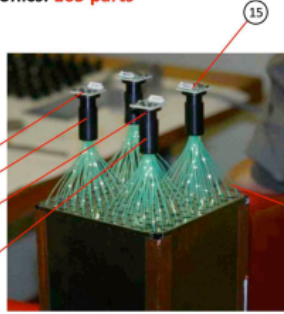
538 parts

- 11) Lead tiles (76)
- 12) Scintillator tiles (308)
- 13) Bond paper sheets (154)

Readout and Electronics:

165 parts

- 14) WLS fibers (144)
- 15) APD (4)
- 16) CSP (4)
- 17) Light guides (4)
- 18) Mount (4)
- 19) Collars (4)
- 20) Diffuser (1)



TOTAL parts: 20

TOTAL components: 831

Plus cabling, GMS and mech. supports

Figure 35: The exploded EMCAL tower view

1337 determination in Pb–Pb collisions.

1338 The multiplicity measurement of V0 is complimented by the forward multiplicity
1339 detector (FMD) [242]. FMD includes five rings of silicon strip detectors that
1340 make up the FMD. FMD gives acceptance in the range $-3.4 < \eta < -1.7$ and
1341 $1.7 < \eta < 5.0$.

1342 During long shutdown 2 in 2019-2020, V0 and T0 will be replaced by the Fast
1343 Interaction Trigger (FIT) detector [243]. For historical reasons elements of FIT are
1344 also referred to as V0+ and T0+. FIT will allow centrality, event plane, luminosity
1345 and interaction time determination in the continuous readout mode, that ALICE
1346 will operate in after 2020.

1347 For photon multiplicity measurement ALICE has the photon multiplicity detector (PMD) [244]. PMD uses two planes of gas proportional counters with a
1348 cellular honeycomb structure. PMD gives the multiplicity and spatial distribution
1349 of photons in the region $2.3 < \eta < 3.7$.

1351 On top of the ALICE magnet there is an array of 60 large scintillators called
1352 the ALICE cosmic ray detector (ACORDE) [245]. ACORDE is used as a trigger
1353 for cosmic rays for calibration and alignment.

1354 The only hadronic calorimeters in ALICE are the zero degree calorimeters

1355 (ZDC) [246], which are located next to the beam pipe in the machine tunnel
1356 about 116 m from the interaction point. There are two sets of calorimeters. One
1357 is made of tungsten, specialising in measuring neutrons, while the other, made of
1358 brass, is specialised in measuring protons. ZDC is meant to detect spectators, i.e.
1359 parts of the colliding ions that do not take part in the interaction. If there are more
1360 spectators, the collisions is likely to be more peripheral. Thus ZDC gives informa-
1361 tion about the centrality of the event especially in proton-lead collisions [201], but
1362 also in Pb–Pb collisions [86].

1363 A new detector installed during the long shutdown 1 is the ALICE diffractive
1364 detector (AD) [247]. AD consists of two assemblies, one in each side of the interac-
1365 tion point, both made of two layers of scintillators. These assemblies are situated
1366 about 17 m and 19.5 m away from the interaction points. The pseudorapidity cov-
1367 erage is $-6.96 < \eta < -4.92$ and $4.78 < \eta < 6.31$. AD greatly enhances ALICE’s
1368 capability for diffractive physics measurements that require a large pseudorapidity
1369 gap. During long shutdown 2 AD will be updated and integrated as a part of the
1370 FIT detector.

1371 2.3.6 Muon spectrometer

1372 Outside the main magnet, ALICE has a spectrometer dedicated to measuring
1373 muons [248]. In heavy ion physics muons are mainly used to measure the produc-
1374 tion of the heavy quark resonances J/ψ , Ψ' , Υ , Υ' and Υ'' .

1375 The muon spectrometer consists of three parts, the absorber, the muon tracker
1376 and the muon trigger. The absorber is meant to remove the hadronic background
1377 as efficiently as possible. After the absorber there are ten plates of thin cathode
1378 strip tracking stations with high granularity, the muon tracker. After the muon
1379 tracker there is a layer of iron to filter out any remaining particles, other than
1380 muons. The muon trigger is located behind this layer. The trigger consists of four
1381 resistive plate chambers.

1382 2.3.7 Triggers

1383 High energy physics experiments need triggers to select interesting physics. Ex-
1384 periments such as CMS and ATLAS at CERN look for extremely rare events. To
1385 produce these rare events LHC provides up to 40 million events each second. Such
1386 amounts can’t be recorded real-time as many detectors require some time for the
1387 readout, up to 1 ms/event in ALICE. Thus one uses triggers, i.e. a set of very fast
1388 hardware based decisions on which events are to be saved. Additionally one needs
1389 some confirmation that an event has even occurred to tell other detectors that the
1390 event needs to be recorded.

1391 For ALICE the target event rates are 1 MHz for pp collisions, 0.1-2 kHz for
1392 Pb–Pb collisions and 200 kHz for the 2013 p–Pb collisions.

1393 At ALICE the main system responsible for the trigger decisions is the AL-
1394 ICE Central Trigger Processor (CTP) [249]. The CTP generates three levels of
1395 hierarchical hardware triggers - Level 0, Level 1 and Level 2, (L0, L1 and L2 re-
1396 spectively) before an event is accepted and transmitted to the Data Acquisi-
1397 tion system (DAQ). Afterwards additional software assessments are performed by the
1398 High Level Trigger (HLT).

1399 Triggers can be roughly put into two classes, minimum bias triggers that make
1400 sure no empty events are recorded, and rare triggers that require specific signatures
1401 in ALICE detectors, such as large energy deposits in EMCal or two muons in the
1402 muon arm acceptance.

1403 Minimum bias trigger

1404 Several of the ALICE detectors are used to make the initial minimum bias trigger
1405 decisions. These include the SPD layers of ITS, V0 and T0. SPD can count the
1406 number of hits in the first two layers of ITS. Minimum bias pp collisions typically
1407 require at least one hit in either SPD or V0A/V0C. Similarly Pb–Pb triggers look
1408 at both V0 and SPD hits. The p–Pb data has been mainly triggered using V0
1409 information.

1410 EMCal trigger

1411 In addition to the minimum bias triggers, the most relevant trigger for this thesis
1412 is the EMCal trigger. Parts of the EMCal trigger has been developed at the
1413 University of Jyväskylä. Extensive details of the trigger and the development
1414 work can be found in the thesis of Jiří Král [250]. Personally I have contributed
1415 to the maintenance of the level 0 trigger.

1416 ALICE EMCal provides two levels of trigger signal, L0 and L1, which allows
1417 triggering on either single shower deposits or integrated energy deposits in larger
1418 ares, i.e. jets [251]. As inputs the trigger gets exclusive sets of 2×2 EMCal towers,
1419 to limit the number of channels that need to be processed. The L0 trigger then
1420 checks for energy deposits within a rolling window of 2×2 trigger channels (4×4
1421 towers). Areas of 4×4 towers most probably will contain only a single shower or
1422 two adjacent showers coming from a single decayed π^0 . Thus the trigger is called
1423 the single shower trigger.

1424 For L0 the trigger decision is done in Trigger Region Units (TRU) that each
1425 cover 4×42 channels (8×48 towers). The amplitude from the sliding window
1426 is compared to a constant threshold. Additionally a peak finding algorithm is
1427 implemented to define correctly the time of the signal maximum. A single bit OR

1428 decision of all individual TRUs is forwarded to the CTP as the EMCAL L0 trigger
1429 decision.

1430 The L0 information is additionally forwarded to the L1 trigger, which recom-
1431 putes similar 2×2 channel decisions to produce the single shower trigger, but L1
1432 can perform the calculation also on the borders between trigger units. In addition
1433 the L1 trigger can check for energy deposits inside a larger 16×16 channel (32×32
1434 towers) window, which is considered to be the jet trigger.

1435 The L1 trigger can compare up to two thresholds for each single shower and
1436 jet trigger. There is a dedicated link in between the V0 detector and EMCAL STU,
1437 which can provide centrality information that is used to compute a dynamical
1438 threshold as a function of the V0 multiplicity.

1439 The trigger subsystem provides both the L0 and L1 decisions to the CTP and
1440 DAQ.

1441 2.4 TPC upgrade

1442 2.4.1 ALICE upgrade during LS2

1443 During LS2 in 2019-2020 ALICE will go through significant modifications. The
1444 goal is to be able have continuous readout [252] in heavy ion collisions at an
1445 interaction rate of 50 kHz. ALICE will add a new Forward Interaction trigger
1446 (FIT) [253] to provide trigger and timing replacing the V0 and T0 detectors. Also
1447 the current FMD and AD detectors will be dismantled and their roles will be taken
1448 over by FIT.

1449 Additionally the current inner tracking system (ITS) will be completely re-
1450 placed. The current layered structure with three different technologies will be
1451 replaced by a detector that uses pixel technology in all layers and with signifi-
1452 cantly reduced pixel size. Additionally the first layer will be brought closer to the
1453 beam pipe. The new ITS will have better tracking efficiency and better impact
1454 parameter resolution [230].

1455 The muon detection will be complimented by the Muon Forward Tracker
1456 (MFT) [254]. Based on the same technology as the new ITS, MFT will be placed
1457 before the hadron absorber that sits in front of the existing muon spectrometer.
1458 MFT should significantly increase the signal/background ratio in heavy quark
1459 measurements [254].

1460 2.4.2 TPC upgrade

1461 Many subdetectors will make small improvements to enhance the readout rate.
1462 The central trigger processor will be replaced and ALICE will introduce a new
1463 framework O^2 that combines both online data acquisition and offline analysis.

1464 The detector restricting the readout the most at the moment is the TPC.
1465 The current wire chamber based system limits the readout rate to 3.5 kHz. To
1466 achieve the 50 kHz readout rate goal the wire chambers will be replaced by a Gas
1467 Electron Multiplier (GEM) based system. The GEMs are designed to minimise
1468 ion backflow to allow continuous, ungated and untriggered readout. I have made
1469 a personal contribution to the quality assurance of the new GEM readout of TPC.

1470 TPC has a total of 36 inner and 36 outer readout chambers. Each of these will
1471 consist of 4 layers of GEM foils. The inner chambers will only have one foil for
1472 each layer. The outer chambers are separated into three sections, each with its
1473 own layer of foils. Each GEM foil is made up of a 50 μm thick resistive capton
1474 layer, coated on both sides by 5 μm thick layers of copper. Each foils is separated
1475 into a number (20-24 depending on the size of the foil) of distinct active areas.
1476 The active areas are pierced densely with holes. They have 50-100 holes in the
1477 area of a single mm^2 . The density of holes changes from layer to layer. The two
1478 middle layers of foils have a larger (double) pitch (smaller hole density) while the
1479 top and bottom layers have a smaller (normal) pitch (larger hole density).

1480 The purpose of the multilayered structure is to reduce the ion backflow [255,
1481 256]; not only one layer of GEM foils will be installed, but a 4 layer stack. In the
1482 stack there are 2 standard pitch GEM foils, where the pitch size, i.e. the separation
1483 of the holes inside a foil is around 140 μm , and 2 large pitch GEM foils, there the
1484 hole spacing is two times larger, 280 μm . The two outer layers will have standard
1485 pitch and the two middle layers have large pitch. The middle layers with large
1486 pitch serve as extra insulator against the ion backflow. Additionally the setup
1487 allows operating individual GEM foils at lower voltages and still have an increase
1488 in the gain of a few orders of magnitude [257].

1489 The holes have a conical shape which they acquire during a two step chemical
1490 etching process. The designed inner and outer diameters of the holes are $50 \pm 5 \mu\text{m}$
1491 and $70 \pm 5 \mu\text{m}$ respectively. Figure 36 shows the cross-section of a hole alongside
1492 with the operation principle of a GEM foil.

1493 The working principle of these foils is based on the Townsend avalanche phe-
1494 nomenon [258], which is also used in proportional counters such as Geiger counters.
1495 There is a large potential difference (140-400 V) applied to the two sides of the
1496 foil, which results in large field in each hole. Electrons gain energy in the field and
1497 if the electric field is strong enough, the free electron can gain sufficient velocity
1498 (energy) to liberate another electron when it next collides with a molecule. The
1499 two free electrons then travel along the electric field and can gain sufficient energy
1500 from the electric field to cause further impact ionisations, and so on, leading to a
1501 chain reaction. Under the right conditions a single electron entering any hole will
1502 create an avalanche containing 100–1000 electrons; this is the gain of the GEM
1503 foil.

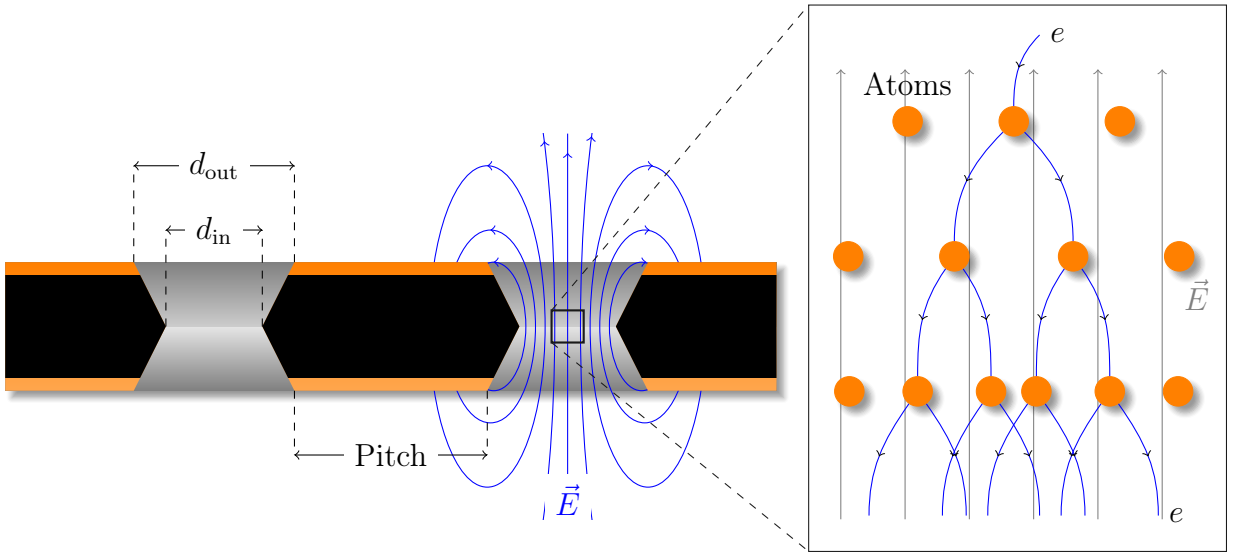


Figure 36: *left* Cross-section of a GEM foil. (Not to scale). The hole diameters are $d_{in} = 50 \pm 5 \mu\text{m}$ and $d_{out} = 70 \pm 5 \mu\text{m}$ and pitch is either 140 or 280 μm . *right* The amplification of a GEM foil is based on the Townsend avalanche phenomenon [258]. Electrons entering the electric field inside the hole are accelerated. If they gain enough energy before colliding with atoms they can liberate additional electrons, which are further accelerated leading to a chain reaction.

1504 As opposed to wire chambers, which typically have one voltage setting, a GEM-
 1505 based detector requires several independent voltage settings: there is a drift voltage
 1506 which drives the electrons from the ionisation point to the GEM, an amplification
 1507 voltage, and an extraction voltage that brings electrons from the GEM exit to the
 1508 readout plane. In a multilayer system this is further complicated. The voltages
 1509 between layers of foils can be tuned individually optimising amplification and
 1510 preventing ion backflow.

1511 Quality Assurance of the GEM foils

1512 The GEM foils are produced at CERN, where they will undergo a basic QA (QA-B)
 1513 procedure, that includes a coarse optical inspection for any large defects ($\gtrsim 1 \text{ mm}$)
 1514 and a short term high voltage measurement. Afterwards the foils are sent for an
 1515 advanced quality assurance (QA-A) procedure which is performed in one of the
 1516 two QA-A centers, one in the Helsinki Institute of Physics (HIP) and one in the
 1517 Wigner Research Centre in Budapest. Details of the QA-A procedure can be found
 1518 in the thesis of Márton Vargyas [259] and in [260]. In the QA-A centers all foils
 1519 are put through a detailed optical scanning process and a long term high voltage
 1520 measurement. I was personally performing the QA production in Helsinki for the

1521 final 6 months of the project.

1522 The optical scan is performed with the help of a scanning robot. The setup
1523 along with most of the software was developed at the Detector Laboratory of the
1524 Helsinki Institute of Physics [261]. The optical scan is able to distinguish every
1525 single hole on the GEM foil and measure their properties. The purpose of the
1526 scan is two-fold; to catch defects that could affect the performance and classify the
1527 foils based on their hole parameters. It is expected that these are connected with
1528 the foil's electric properties [261]. For example, smaller holes create more intense
1529 and focused fields, which would result in larger amplification of their avalanche
1530 electrons, i.e. the local gain is expected to be larger.

1531 After the optical scanning, the foils are subjected to a long term (5-12 hours)
1532 high voltage leakage current measurement. Each segment of the GEM foil is con-
1533 nected to a high voltage of 500 V and the leakage current is measured separately
1534 for each segment. The accepted leakage current in each segment is 0.16 nA. Foils
1535 that fail the criteria are sent to CERN for recleaning or repairing, after which they
1536 will go through the QA pipeline again.

1537 Additionally some foils will be put through a gain mapping procedure. This
1538 process is time consuming and can only be performed in the QA-A center in
1539 Budapest. Thus it was done for only a small subset of foils. However, by measuring
1540 the gain in some foils the gain can be correlated with foil properties. Thus the
1541 single foil gain can be predicted based on the results of the optical scan. Details
1542 can be found in [259].

3 Event and track selection

The $\sqrt{s_{\text{NN}}} = 5.02$ TeV p–Pb ($1.3 \cdot 10^8$ events, $\mathcal{L}_{\text{int}} = 62 \text{ nb}^{-1}$) collisions were recorded in 2013 by the ALICE detector [217]. The details of the performance of the ALICE detector during LHC Run 1 (2009–2013) are presented in Ref. [262].

3.1 Event selection

This analysis uses both a minimum bias trigger and an EMCal based trigger to select the analysed events. For the 2013 p–Pb collisions minimum bias events are required to have signals in both V0A and V0C. The timing difference between the two stations is also used to reduce the contamination of the data sample from beam-gas events [262].

EMCal is used to provide the jet trigger used in triggered datasets. EMCal can be used to trigger on single shower deposits or energy deposits integrated over a larger area. Latter case is used for jet triggers. The EMCal trigger definition in the 2013 p–Pb collisions requires an energy deposit of either 10 GeV for the low threshold trigger or 20 GeV for the high threshold trigger in a 32×32 patch size. Triggers, V0 and EMCal are discussed in more detail in sections 2.3.5, 2.3.7 and 2.3.4.

3.2 Track reconstruction

The analysis uses charged tracks that are reconstructed with the Inner Tracking System (ITS) [263] and the Time Projection Chamber (TPC) [231]. These are discussed in sections 2.3.1 and 2.3.2. A detailed overview of track reconstruction in ALICE can be found from [262].

The track reconstruction procedure is shown in Figure 37. The figure shows only one track, but in reality the reconstruction has to deal with many tracks. The main reconstruction of tracks starts in TPC. There are 159 tangential pad rows in the TPC readout chambers. The track reconstruction starts from the outermost layer and the hits are paired with hits in the next layer inwards, taking into account a proximity cut. When this track finding procedure hits the innermost pad row in TPC, this information is used as an initial seed for the track finding in ITS. Similar procedure of pairing adjacent layers with a proximity cut is repeated in ITS.

After the reconstruction of tracks in ITS is completed, all the tracks are extrapolated to their point of closest approach to the preliminary interaction vertex. Then the second track fitting step begins, this time starting from the interaction point and proceeding outwards. A Kalman filter [264] technique is used to do the new fit using the hits found in the previous stage. This time the tracks are matched

1579 also to the other detectors in the central barrel beyond TPC. When this step is
1580 complete, a final refit from the outermost TPC pad rows towards the interaction
1581 point is performed. The final track parameters come from this refit.

1582 With the final track parameters the primary vertex can be determined with
1583 better accuracy than with only SPD information. The tracks are extrapolated to
1584 the nominal beam line and a weighted average of the points of closest approach
1585 determines the accurate primary vertex position.

1586 The final step of the track reconstruction is the determination of the secondary
1587 vertices. For this, all the tracks whose distance of closest approach (DCA) to
1588 the primary vertex is larger than a defined minimum value are selected. For these
1589 tracks, points of closest approaches are determined for pairs of tracks. If the tracks
1590 are sufficiently close to each other and show characteristics of short lived particle
1591 decays, these points are identified as secondary vertices.

1592 Combining the information from the ITS and the TPC provides a resolution
1593 ranging from 1 to 10 % for charged particles with momenta from 0.15 to 100 GeV/c.
1594 For tracks without the ITS information, the momentum resolution is comparable
1595 to that of ITS+TPC tracks below transverse momentum $p_T = 10 \text{ GeV}/c$, but for
1596 higher momenta the resolution reaches 20 % at $p_T = 50 \text{ GeV}/c$ [262, 266].

1597 Track selection

1598 In p–Pb collisions the tracks are selected following the hybrid approach [267]
1599 which ensures a uniform distribution of tracks as a function of azimuthal angle
1600 (φ). The parameters in the approach are summarised in Table 2.

1601 The first requirements are on the quality of the track fit in ITS and TPC.
1602 The ITS requirement only removes tracks that are clear outliers. For TPC the
1603 requirement is much more strict. For step 1 it is required that a track has 3 out
1604 of the 6 possible hits in ITS, one of which must be in the SPD. In step 2 this
1605 is replaced by an additional vertex constraint, where the primary vertex itself is
1606 added as a point to the track to improve the momentum resolution.

1607 For the TPC, 70 crossed pad rows out of the maximum 159 is required. This
1608 measures the effective track length inside the TPC. This takes into account the
1609 possibility of having pad rows missing in the middle of the track due to charge in
1610 these clusters being below the threshold for some reason. Additionally it is required
1611 that the ratio between crossed rows and findable clusters is at least 0.8. Findable
1612 clusters are defined as the number of geometrically possible clusters which can be
1613 assigned to a track, taking into account dead zones due to chamber boundaries
1614 and limited η -acceptance. For both steps of the hybrid cut it is required that the
1615 fraction of clusters shared with several tracks is less than 40%.

1616 The remaining cuts are meant to make sure that the measured tracks are really
1617 produced in the primary collision. A track might gain a kink due to a particle

Table 2: Parameters in the hybrid track cut

Track Cut	Step 1	Step 2
$\chi^2 / \text{ITS cluster}$	< 36	< 36
$\chi^2 / \text{ITS cluster}$	< 4	< 4
Hits in ITS	3	0
ITS hit requirements	1 in SPD	No requirement
Vertex constraint	No	Yes
Number of crossed rows in TPC	70	70
TPC crossed rows over findable clusters	> 0.8	> 0.8
Fraction of shared TPC clusters	< 0.4	< 0.4
Kink daughters	Rejected	Rejected
DCA_{xy}	< 3.2 cm	< 3.2 cm
DCA_z	< 2.4 cm	< 2.4 cm
Other		Rejected by step 1

1618 scattering decay. The particle after such a kink, a kink daughter, is rejected in
 1619 the cuts, as it no longer describes the properties of the primary collisions. The
 1620 final cuts are on the distance of closest approach (DCA) of the track to primary
 1621 vertex. To have confidence that the track comes from the primary collision, the
 1622 track must be close enough to the primary vertex. The cuts are different for the
 1623 distance along (DCA_z) and perpendicular to (DCA_{xy}) the beam axis.

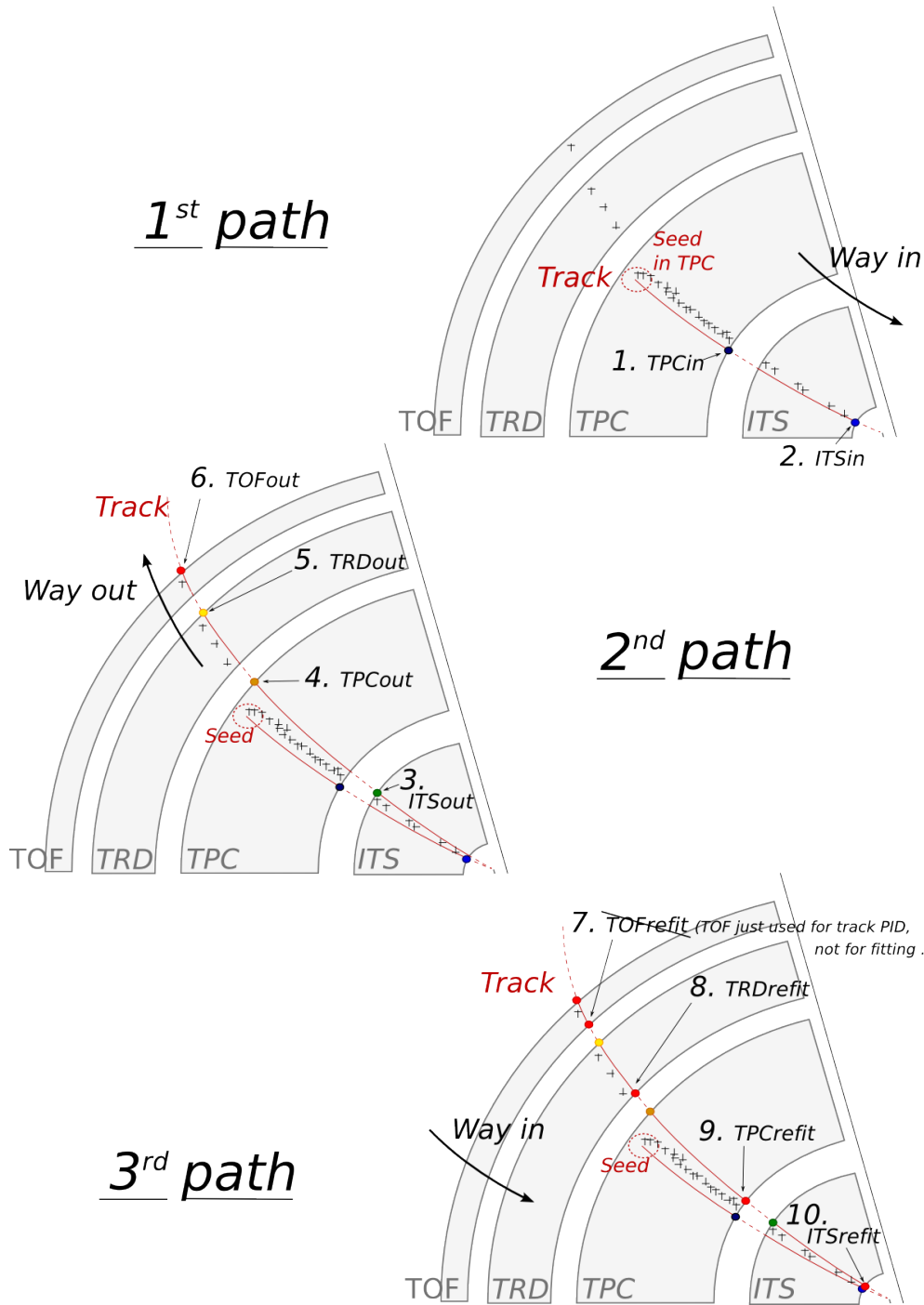


Figure 37: Principles of tracking in the ALICE experiment, showing the three successive paths allowing to build a track and refine its parameters. Numbers ranging from 1 to 10 mention the bits that are activated in case of success during the propagation of the Kalman filter at the considered stage. Figure from [265]

1624 3.3 Cluster selection

1625 Neutral particles used in jet reconstruction are reconstructed by the Electromagnetic
 1626 Calorimeter (EMCal) [240]. The EMCal covers an area with a range of
 1627 $|\eta| < 0.7$ in pseudorapidity and 100 deg in azimuth. EMCal is complimented with
 1628 the Dijet Calorimeter (DCal) [241] and Photon Spectrometer (PHOS) [239] that
 1629 are situated opposite of the EMCal in azimuth. PHOS covers 70 degrees in azimuth
 1630 and $|\eta| < 0.12$. The DCal is technologically identical to EMCal. The DCal
 1631 coverage spans over 67 degrees in azimuth, but in pseudorapidity the mid region
 1632 is occupied by the PHOS. In between PHOS and DCal active volumes, there is a
 1633 gap of 10 cm. DCal is fully back-to-back with EMCal.

1634 The clusters used in the analysis were obtained from the EMCal clusteriser.
 1635 The parameters used in the clusteriser are summarised in Table 3. The clusteriser
 1636 searches for a tower with energy deposit greater than a defined seed energy and
 1637 merges all surrounding (sharing a side) towers with energy deposit higher than a
 1638 defined threshold. In the next step all towers sharing a side with already included
 1639 towers are added, again requiring that the energy deposits exceeds the threshold.
 1640 The algorithm can identify local minima and halts the clustering in case that the
 1641 neighbouring tower energy is higher. Already clustered towers are removed from
 1642 the pool, so one tower can only be clustered once.

1643 Highly energetic calorimeter hits should spread into several towers as the elec-
 1644 tromagnetic shower evolves. However, some clusters with high energy have their
 1645 energy located in a single tower. These are believed to come from a slow neutron
 1646 hitting the APD readout of the towers. They are referred to as exotic clusters.
 1647 The measure of exotoxicity is denoted as

$$1 - \frac{E_{\text{cross}}}{E_{\text{max}}}, \quad (42)$$

1648 where E_{max} is the energy in the most energetic tower and E_{cross} is the sum of the
 1649 four towers neighbouring the most energetic one. The closer this is to 1, the more

Table 3: Parameters used in the EMCal clusteriser

Setting	Value
Clusteriser seed	0.2 MeV
Clusteriser cutoff	0.05 MeV
Cells in cluster	> 1
Track matching radius	0.025
Fiducial cut	1 tower
Exotic cut	0.97
Minimal cluster Energy	0.3 GeV

1650 exotic the cluster is and the larger the probability that it is fake. Cut of 0.97 has
1651 been adopted as default for analyses using EMCal, including the one presented in
1652 this thesis. Any clusters above this cut are removed.

1653 A method of matching the cluster position to TPC track extrapolation is used
1654 to suppress charged hadron contribution to hits in EMCal. Tracks identified by the
1655 tracking detectors are extrapolated close to the EMCal surface, where the closest
1656 cluster is found and the track extrapolation is continued until reaching the same
1657 depth as the cluster. The remaining distance in between the extrapolated track
1658 and the cluster is then used to reject hadronic hits. Clusters matched to charged
1659 tracks are removed from the analysis as well as clusters being identified as fake.

1660 4 Analysis method

1661 4.1 Jet Finding

1662 The analysis uses reconstructed jets as estimates of the original parton. Jet recon-
1663 struction essentially combines nearby tracks into jets.

1664 Collisions between hadrons are never as clean as electron-electron collisions.
1665 Even for a proton-proton collision there are participant partons, that will produce
1666 a soft background in addition to the hard scattering products. Jet reconstruction
1667 must deal with this soft background. The reconstruction is never perfect, one can
1668 have uncorrelated tracks that get included in the jet and some tracks originating
1669 from the parton are missed by the reconstruction. There are several methods to
1670 perform the reconstruction, all of which require some kind of size parameter, which
1671 cuts out jet participants too far from the jet axis. The tracks that are grouped
1672 into a jet are referred to as jet constituents.

1673 In each collision event, the jets are reconstructed using FastJet [268] with the
1674 anti- k_T algorithm [269]. Jets for $R=0.4$ are selected in $|\eta| < 0.25$ to satisfy the
1675 fiducial acceptance of the EMCAL. In jet reconstruction both charged tracks with
1676 $p_T > 0.15 \text{ GeV}/c$ and neutral clusters with $p_T > 0.30 \text{ GeV}/c$ are considered. Clus-
1677 ters that match charged tracks are removed before jet reconstruction. The analysis
1678 is then performed by analysing the charged jet constituents and results are pre-
1679 sented in terms of the jet transverse momentum $p_{T,\text{jet}}$.

1680 4.1.1 Anti k_T algorithm

1681 Jets are reconstructed using the anti- k_T algorithm [269]. The algorithm works by
1682 trying to undo the splittings through combining protojets. First the algorithm
1683 creates a list of protojets. At the beginning the list is populated by converting
1684 each track in the event into a protojet. Then the algorithm proceeds by combining
1685 these protojets. A simplified picture of the process for a limited number of tracks
1686 is shown in Figure 38

1687 The algorithm calculates distance measures for each individual protojet and
1688 for each possible pair of protojets. For individual protojets this depends on the
1689 transverse momentum of the track.

$$k_{T,i}^2 = p_{T,i}^{2p} \quad (43)$$

1690 For each pair of protojets the distance measure is calculated as

$$k_{Ti,j}^2 = \min(p_{Ti}^{2p}, p_{Tj}^{2p}) \frac{\Delta R_{i,j}^2}{D^2}, \quad (44)$$

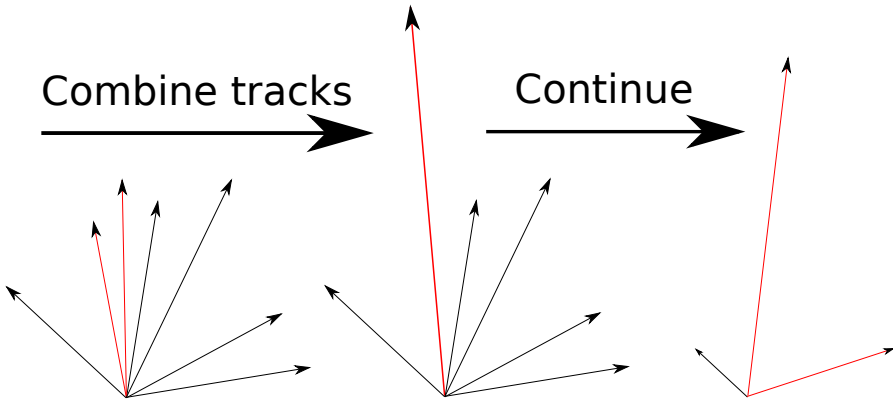


Figure 38: A simple example of the antil- k_T algorithm in progress. The red tracks in the leftmost figure are identified to have the smallest $k_{T,i}$ in the event and are combined into the red track of the middle figure. As this continues the remaining tracks are added to this or other jets. One tracks was deemed to be isolated enough to be counted as a protojet by itself. Note that the rightmost figure is zoomed out.

1691 where

$$R_{i,j} = (\phi_i - \phi_j)^2 + (y_i - y_j)^2. \quad (45)$$

1692 If k_{Ti} is the smallest quantity then the protojet is a jet and it is removed from
1693 further consideration. If $k_{Ti,j}$ is the smallest quantity the two protojets i and j are
1694 merged. This is repeated until no protojets are left.

1695 The choice of the power p in the distance measure depends on the algorithm
1696 used

- 1697 • $p = 1$: k_T algorithm
- 1698 • $p = 0$: Cambridge Aachen algorithm
- 1699 • $p = -1$: anti- k_T algorithm

1700 With the choice $p = -1$ in anti- k_T algorithm, the softest splittings are un-
1701 done first. One consequence of the power choice in the anti- k_T algorithm is that
1702 reconstructed jets have a shape close to circular.

1703 4.2 Definition of j_T

1704 The reconstructed jet axis is used for j_T reference. Any charged track within a
1705 fixed cone with radius R is taken as a jet constituent, as opposed to using the
1706 constituent list provided by the jet algorithm. Anti- k_T produces jets that are

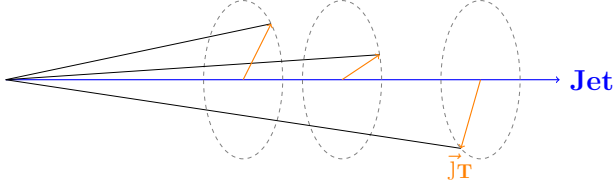


Figure 39: Illustration of \vec{j}_T . The jet fragmentation transverse momentum, \vec{j}_T , is defined as the transverse momentum component of the track momentum, \vec{p}_{track} , with respect to the jet momentum, \vec{p}_{jet} .

very circular in shape. Thus this doesn't change the constituent list considerably.
Calorimeter clusters are used only in jet reconstruction.

The jet fragmentation transverse momentum, \vec{j}_T , is defined as the component of the constituent track momentum, \vec{p}_{track} , transverse to the jet momentum, \vec{p}_{jet} . It represents the transverse kick with respect to the initial hard parton momentum that is given to a fragmenting particle during the fragmentation process, which is a measure of the momentum spread of the jet fragments.

The resulting \vec{j}_T is illustrated in Fig. 39. The length of the \vec{j}_T vector is

$$j_T = \frac{|\vec{p}_{\text{jet}} \times \vec{p}_{\text{track}}|}{|\vec{p}_{\text{jet}}|}. \quad (46)$$

Resulting j_T distributions are shown as

$$\frac{1}{j_T} \frac{dN}{dj_T} \quad (47)$$

distributions. The logic behind this is that j_T is inherently a two-dimensional observable, comprised of j_{Tx} and j_{Ty} components. So the actual physical observable would be

$$\frac{d^2N}{dj_{Tx} dj_{Ty}} \quad (48)$$

Changing into polar coordinates with $j_{Tr} = j_T$ and θ gives

$$\frac{d^2N}{j_T dj_T d\theta}, \quad (49)$$

where j_T over the azimuth θ should stay constant and it can be integrated over, which gives

$$\frac{1}{2\pi} \frac{dN}{j_T dj_T}. \quad (50)$$

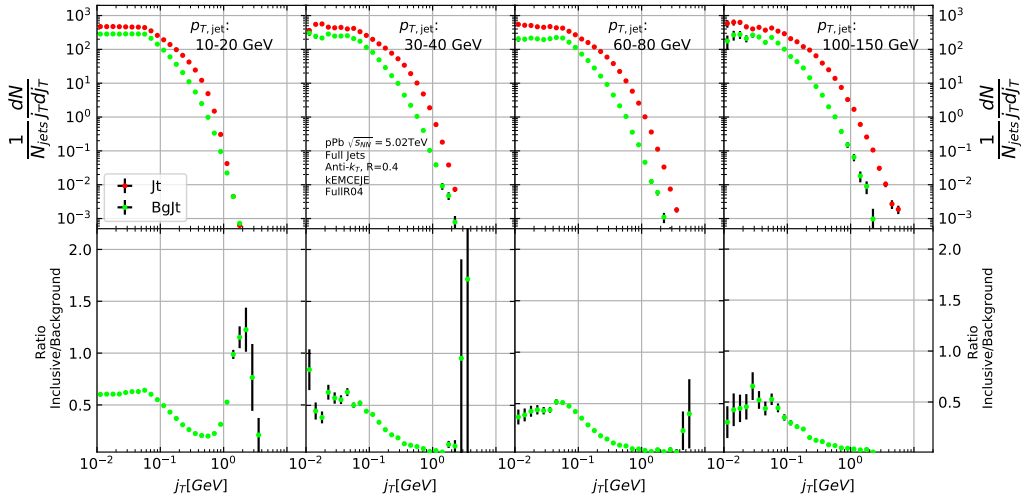


Figure 40: Inclusive j_T with background

1722 Results of the raw inclusive j_T distribution in four $p_{T,\text{jet}}$ bins with background
 1723 are shown in Figure 40. Background, i.e. the contribution from the underlying
 1724 event, is further discussed in Section 4.4

1725 4.3 Unfolding detector effects

1726 The raw inclusive j_T distributions are corrected for the detector inefficiency with
 1727 an unfolding procedure. The procedure uses response matrices obtained from a
 1728 PYTHIA [270] simulation.

1729 Measured distributions are affected by two main factors; Limited acceptance -
 1730 The probability to observe a given event is less than one and limited resolution -
 1731 Quantity x cannot be determined exactly, but there is a measurement error. True
 1732 $f(x)$ and measured $g(y)$ distributions are connected by a convolution integral.
 1733 Including statistical fluctuations this becomes

$$\hat{g}(y) = \int_a^b A(y, x) f(x) dx + \epsilon(y), \quad (51)$$

1734 where A is the detector response obtained by (for example) Monte Carlo simula-
 1735 tions and $\epsilon(y)$ is the term coming from statistical fluctuations. If x and y are
 1736 discrete variables we have

$$\hat{g}_i = \sum_{j=1}^m A_{ij} f_j + \epsilon_i, \quad (52)$$

₁₇₃₇ where i and j give the j_T bins in the true and measured distributions. f_j and
₁₇₃₈ g_i give the counts in these bins. Or in matrix form

$$\hat{g} = Af + \epsilon, \quad (53)$$

₁₇₃₉ where \hat{g} and f are vectors corresponding to the measured and true histograms. If
₁₇₄₀ the only detector effect is limited acceptance, A is a diagonal matrix, i.e. $A_{ij} =$
₁₇₄₁ 0 for $i \neq j$. We want to deduce the true distribution f , when the measured
₁₇₄₂ distribution g is known. In a general discrete case the (naive) solution is obtained
₁₇₄₃ by the inverse matrix

$$\hat{f} = A^{-1}\hat{g} \quad (54)$$

₁₇₄₄ However this usually leads to oscillating solutions and determining the inverse
₁₇₄₅ matrix can be difficult.

₁₇₄₆ Two common methods to perform this inversion are Bayesian and SVD unfold-
₁₇₄₇ ing methods. Often the solution requires some additional *a priori* information.
₁₇₄₈ For example the solution should be smooth in most cases.

₁₇₄₉ 4.3.1 Bayesian unfolding

₁₇₅₀ The bayesian (iterative) method is based on the Bayes formula [271].

$$P(C_i|E_j) = \frac{P(E_j|C_i) P_0(C_i)}{\sum_{l=1}^{n_C} P(E_j|C_l) P_0(C_l)}, \quad (55)$$

₁₇₅₁ i.e. the probability of Cause C_i ("truth") given Effect E_j ("observed") is propor-
₁₇₅₂ tional to the probability of observing E_j given C_i , $P(E_j|C_i)$ (response matrix) and
₁₇₅₃ the true distribution $P_0(C_i)$.

₁₇₅₄ In the unfolding procedure P_0 is given some starting distribution, either a
₁₇₅₅ uniform distribution or some guess of the final distribution. Taking into account
₁₇₅₆ the inefficiency this gives

$$\hat{n}(C_i) = \frac{1}{\epsilon_i} \sum_{j=1}^{n_E} n(E_j) P(C_i|E_j), \quad (56)$$

₁₇₅₇ where

$$P(C_i|E_j) = \frac{P(E_j|C_i) P_0(C_i)}{\sum_{l=1}^{n_C} P(E_j|C_l) P_0(C_l)}, \quad (57)$$

₁₇₅₈ and $n(E_j)$ are the observed frequencies. First $P(C_i|E_j)$ is calculated with the
₁₇₅₉ uniform distribution or best guess of the shape of the distribution. This is then
₁₇₆₀ used to calculate the new distribution $\hat{P}(C_i)$

$$\hat{N}_{true} = \sum_{i=1}^{n_C} \hat{n}(C_i), \quad \hat{P}(C_i) = P(C_i|\hat{n}(E)) = \frac{\hat{n}(C_i)}{\hat{N}_{true}} \quad (58)$$

1761 P_0 is then replaced with \hat{P} and the procedure is repeated until an acceptable
1762 solution is found. One way to gauge the acceptability is measuring the change
1763 between iterations. Initially there is a large change between iterations, but it
1764 should get small when close to the final distribution. The number of iterations
1765 should be as low as possible, as the errors increase when going further in the
1766 iterations, but the number of iterations must be high enough so that the correct
1767 distribution is extracted.

1768 The bayesian procedure alongside with the SVD unfolding method are imple-
1769 mented in the RooUnfold package [272], which is used to perform the unfolding
1770 in practice. SVD unfolding is another procedure that utilises the Singular Value
1771 Decomposition (SVD) of the response matrix to find the inverse of the response
1772 matrix [273].

1773 Error propagation in the Bayesian procedure

1774 The measured distribution has some statistical uncertainty, this should be reflected
1775 in the unfolded distribution. Additionally the response matrix may have some
1776 uncertainty if the statistics used in the Monte Carlo simulation were limited.

1777 For errors originating from the measured distribution RooUnfold uses the error
1778 propagation matrix

$$\frac{\partial \hat{n}(C_i)}{\partial n(E_j)} = M_{ij} + \frac{\hat{n}(C_i)}{n_0(C_i)} \frac{\partial n_0(C_i)}{\partial n(E_j)} - \sum_{k=1}^{n_E} \sum_{l=1}^{n_C} \frac{n(E_k) \epsilon_l}{n_0(C_l)} M_{ik} M_{lk} \frac{\partial n_0(C_l)}{\partial n(E_j)}, \quad (59)$$

1779 where $\hat{n}(C_i)$ is the unfolded result from Eq. 58. This depends upon the matrix
1780 $\frac{\partial n_0(C_i)}{\partial n(E_j)}$, which is $\frac{\partial \hat{n}(C_i)}{\partial n(E_j)}$ from the previous iteration. In the first iteration, $\frac{\partial n_0(C_i)}{\partial n(E_j)} = 0$
1781 and $\frac{\partial \hat{n}(C_i)}{\partial n(E_j)} = M_{ij}$.

1782 The error propagation matrix V is used to obtain the covariance matrix on the
1783 unfolded distribution

$$V(\hat{n}(C_k), \hat{n}(C_l)) = \sum_{i,j=1}^{n_E} \frac{\partial \hat{n}(C_k)}{\partial n(E_i)} V(\hat{n}(E_i), \hat{n}(E_j)) \frac{\partial \hat{n}(C_l)}{\partial n(E_j)}, \quad (60)$$

1784 where $V(\hat{n}(E_i), \hat{n}(E_j))$ is the covariance matrix of the measurements. In count-
1785 ing experiments common in particle physics, each bin is independently Poisson
1786 distributed, with

$$V(\hat{n}(E_i), \hat{n}(E_j)) = n(E_i) \delta_{ij} \quad (61)$$

1787 The error propagation matrix for the response matrix is

$$\frac{\partial \hat{n}(C_i)}{\partial P(E_j|C_k)} = \frac{1}{\epsilon_i} \left(\frac{n_0(C_i) n(E_j)}{f_j} - \hat{n}(C_i) \right) \delta_{ik} - \frac{n_0(C_k) n(E_j)}{f_j} M_{ij} + \\ \frac{\hat{n}(C_i)}{n_0(C_i)} \frac{\partial n_0(C_i)}{\partial P(E_j|C_k)} - \frac{\epsilon_i}{n_0(C_i)} \sum_{l=1}^{n_E} \sum_{r=1}^{n_C} n(E_l) M_{il} M_{rl} \frac{\partial n_0(C_r)}{\partial P(E_j|C_k)}, \quad (62)$$

where $\frac{\partial n_0(C_i)}{\partial P(E_j|C_k)}$ is the error propagation matrix from the previous iteration, $\frac{\hat{n}(C_i)}{\partial P(E_j|C_k)}$. For the first iteration, this is zero and the final two terms in Eq. 62 disappear.

The covariance matrix due to these errors is given by

$$V(\hat{n}(C_k), \hat{n}(C_l)) = \sum_{j,s=1}^{n_E} \sum_{i,r=1}^{n_C} \frac{\partial \hat{n}(C_k)}{\partial P(E_j|C_i)} V(P(E_j|C_i), P(E_s|C_r)) \frac{\partial \hat{n}(C_l)}{\partial P(E_s|C_r)}, \quad (63)$$

where $V(P(E_j|C_i), P(E_s|C_r))$ can be taken as multinomial, Poisson or other distribution.

4.3.2 Toy Monte Carlo

A toy Monte Carlo simulation was performed to see the performance of unfolding in an ideal case. The simulations samples jet p_T values from the observed p_T distribution. Starting from this p_T the simulations starts creating tracks with

$$p_{\text{track}} = z_{\text{track}} p_{T,\text{jet}} \quad (64)$$

where z_{track} is sampled from the observed z distribution. Tracks are given random η and ϕ values from uniform distributions centred at 0. All tracks below 0.15 GeV are discarded. Sampling is continued until the sum of the track transverse momenta exceeds the jet transverse momentum. The sum of all the track momenta is calculate. This is sum is then defined to be the jet.

Simultaneously a p_T dependant observation efficiency is applied to the tracks and a separate observed jet is calculated using only the observed tracks. Additionally a set of fake tracks is added to the observed jet. Fake tracks are generated identically to normal tracks, except for $p_{T,\text{track}}$, which is taken from an uniform distribution between 0.15 GeV and 1 GeV. Tracks are always either observed or not at the true momentum. No smearing is added to the observed momentum.

Afterwards the tracks are looped over for j_T calculation. For observed tracks we calculate j_T with respect to both the true jet axis and the observed jet. 2D Response matrix is filled with

$$(j_T^{\text{obs}}, p_{T,\text{jet}}^{\text{obs}}, j_T^{\text{true}}, p_{T,\text{jet}}^{\text{true}}) \quad (65)$$

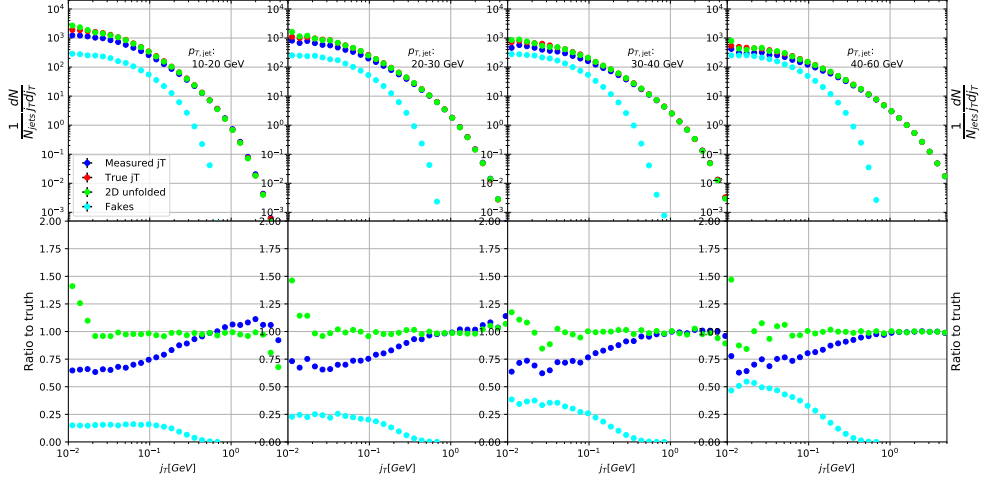


Figure 41: Results from unfolding in Toy Monte Carlo

1812 In practice this is done with a set of 3D histograms, where $p_{T,\text{jet},\text{true}}$ determines
 1813 the histogram index and the remaining three values the bin in the 3D histogram.

1814 After creating the response matrices, an identical procedure is carried out to
 1815 the create testing data. Now instead of filling response matrices, 2D histograms
 1816 are filled with $(j_T^{\text{obs}}, p_{T,\text{jet}}^{\text{obs}})$ and $(j_T^{\text{true}}, p_{T,\text{jet}}^{\text{true}})$

1817 The observed distributions are unfolded using the 2D Bayesian (iterative) algo-
 1818 rithm of RooUnfold. Results are shown in Figure 41. Aside from some discrepancy
 1819 at very low j_T the true distribution is retrieved well.

1820 4.3.3 Pythia Response matrices

1821 A PYTHIA 6 simulation was carried out to determine the response matrices. The
 1822 simulation used the Perugia 2011 [274] tune with $\sqrt{s_{NN}}=5.02$ TeV. The detector
 1823 response of the particle level tracks was simulated using GEANT3 [275, 276].

1824 Response matrices are filled through correlation between MC detector and
 1825 particle level jets and tracks. When creating the response matrices detector level
 1826 tracks in each event are first analysed using the same procedure as for data, but
 1827 their j_T values are stored in an array. This is only done for tracks that are closer
 1828 than the cone size, R , to a jet. Thus most tracks in the event will not have their
 1829 j_T values calculated. The analysis then moves to particle level (MC) tracks. There
 1830 are analysed similarly, but for each track the code checks whether a corresponding
 1831 detector level track existed and if that track had a j_T value. Finally the code
 1832 checks for detector level tracks that don't have corresponding particle level track
 1833 with a j_T value.

1834 There are several possibilities that have to be taken into account:

- We find a corresponding track with a j_T value. Response matrix is filled normally with $(j_T^{\text{obs}}, p_{T,\text{jet}}^{\text{obs}}, j_T^{\text{true}}, p_{T,\text{jet}}^{\text{true}})$
- We don't find a corresponding track. Record $(j_T^{\text{true}}, p_{T,\text{jet}}^{\text{true}})$ as a miss
- We find a corresponding track, but it didn't have j_T value. Most likely because it was not part of a jet in the detector level set. Similary record $(j_T^{\text{true}}, p_{T,\text{jet}}^{\text{true}})$ as a miss
- For detector level tracks that have no correspondence in particle level set the code records $(j_T^{\text{obs}}, p_{T,\text{jet}}^{\text{obs}})$ as a fake

In the analysis code the response matrix is made of an array of 3 dimensional histograms, with $(j_T^{\text{obs}}, p_{T,\text{jet}}^{\text{obs}}, j_T^{\text{true}})$ as axes. The histogram index gives the $p_{T,\text{jet}}^{\text{true}}$ value. The ranges in the response matrices of both j_T and $p_{T,\text{jet}}$ match the ranges used for the end results. For j_T the range is between 0.01 GeV and 20 GeV and $p_{T,\text{jet}}$ between 5 GeV and 500 GeV. The ranges are the same in detector and particle level.

As a primary method unfolding is performed with an iterative (bayesian) algorithm using the RooUnfold [272] package. The number of iterations used is 4. As a default the true j_T distribution from the PYTHIA simulation is used as the prior.

4.3.4 Unfolding closure test

The PYTHIA set is divided into 2 halves. First is used to fill the response matrices, as well as record missed and fake tracks. Second half is used to test the effectiveness of the unfolding method. Jet p_T distributions and response matrix are shown in Figure ???. For the range where this analysis is performed, $40 \text{ GeV} < p_{T,\text{jet}} < 150 \text{ GeV}$, the $p_{T,\text{jet}}$ distribution is recovered well. At low $p_{T,\text{jet}}$ the true distribution can't be recovered. The primary reason is that jet with $p_{T,\text{obs}} < 5 \text{ GeV}$ are not considered, although $p_{T,\text{true}}$ would have been above 5 GeV. Thus these are missing from the response matrix and their contribution can't be unfolded. At high $p_{T,\text{jet}}$ the situation is opposite. Jets with $p_{T,\text{true}} > 500 \text{ GeV}$ are lost due to histogram limits. Thus jets just below this limit are overrepresented in the response matrix for $p_{T,\text{obs}} \approx 500 \text{ GeV}$.

Response matrices within single jet p_T bins are shown in Figure 43. Results from the closure test are shown in Figure 44. In the lowest jet p_T bins unfolding fails to recover the true distribution. The lowest jet p_T bins are dominated by combinatorial jets and thus the true detector response is likely not retrieved.

Above $30 \text{ GeV} < p_{T,\text{jet}} < 40 \text{ GeV}$ the distribution is recovered well in the mid j_T region. At $j_T < 0.1 \text{ GeV}$ there is clear discrepancy and hence the final results are shown only for $j_T > 0.1 \text{ GeV}$. Additionally there is some discrepancy at very high j_T . This is taken into account in the unfolding systematics.

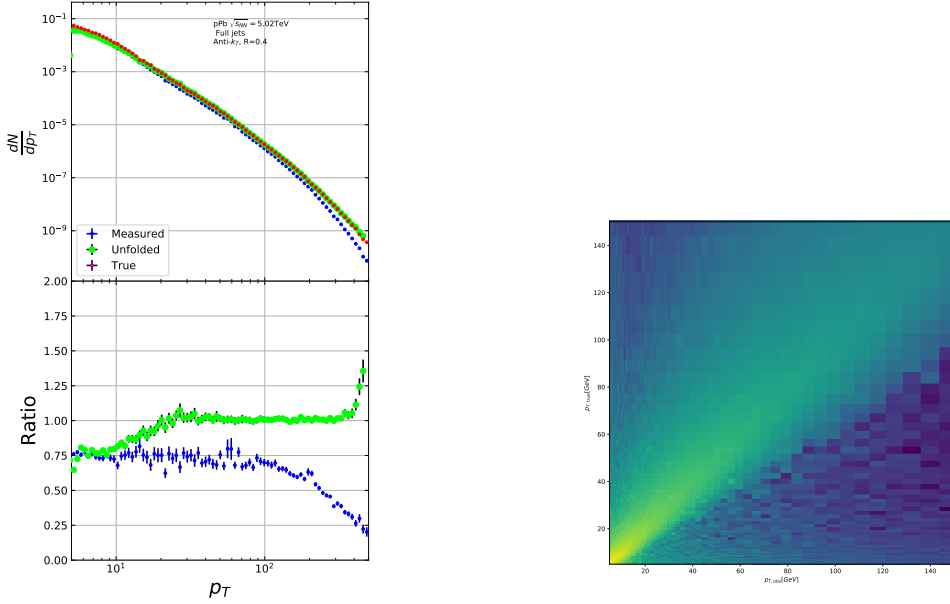


Figure 42: *left*: Unfolded jet p_T distribution in PYTHIA closure test *right*: Jet p_T response matrix from unfolding closure test

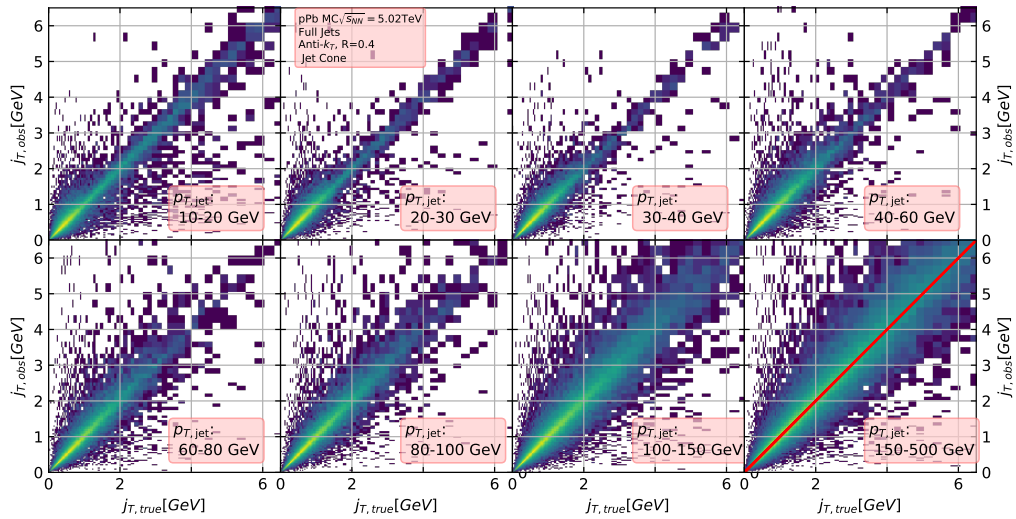


Figure 43: j_T Response matrices in individual $p_{T,\text{jet}}$ bins

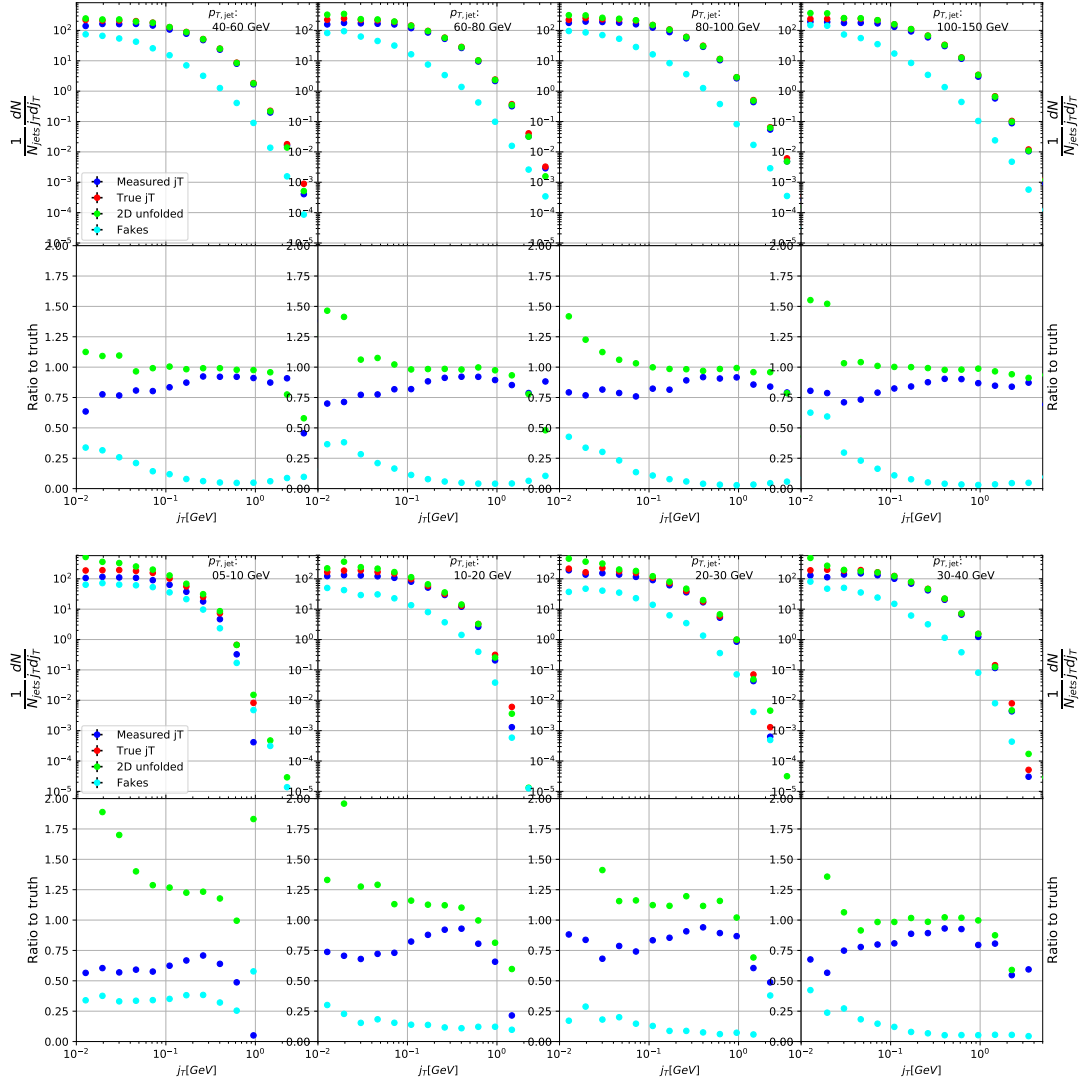


Figure 44: Pythia closure test results. Fake tracks include also tracks that do exist in the true dataset, but for one reason or another were not given j_T values. j_T is only calculated for tracks that are associated with jets.

1872 4.4 Background

1873 When calculating j_T distributions for jet constituents there is a contribution from
 1874 the underlying event (UE), i.e. tracks that just happen to be close to the jet axis.
 1875 To find the signal coming from the actual jet we need to subtract the background
 1876 (UE) contribution. On a jet-by-jet basis this is difficult to achieve reliably, so
 1877 one must estimate the background contribution in the inclusive distribution. A
 1878 schematic view of the background contribution is shown in Figure 45.

1879 We have two methods for background estimation. In the first we look at the
 1880 direction perpendicular to the jet. This is assumed to be the region least likely to
 1881 contain jet contributions. In the second method we randomly assign the tracks of
 1882 event new ϕ and η values. The result is thus guaranteed to be uncorrelated.

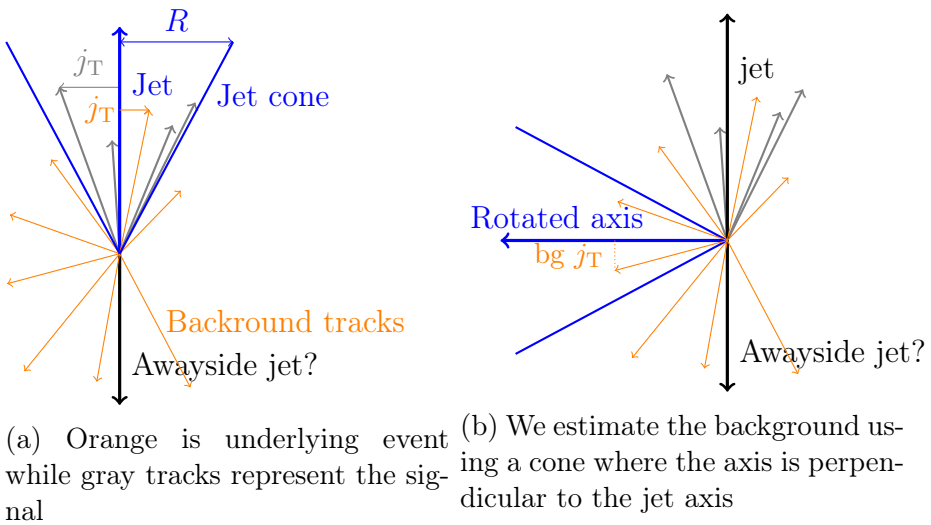


Figure 45: Background estimation

1883 4.4.1 Perpendicular cone background

1884 As a primary method to estimate the background we look at regions of the detector
 1885 where there are no tracks from jets, but only uncorrelated tracks from the under-
 1886 lying event. The underlying event is thus estimated by looking at an imaginary
 1887 jet cone perpendicular to the observed jet axis ($\frac{\pi}{2}$ Rotation in ϕ).

1888 After calculating the j_T values for tracks in the jet, we rotate the jet axis by $\frac{\pi}{2}$
 1889 in positive ϕ direction. We check that there are no other jets closer than $2R$ to the
 1890 rotated axis. Otherwise background calculation is skipped for this jet. Probability
 1891 of this happening is 1-2% depending on the jet p_T bin.

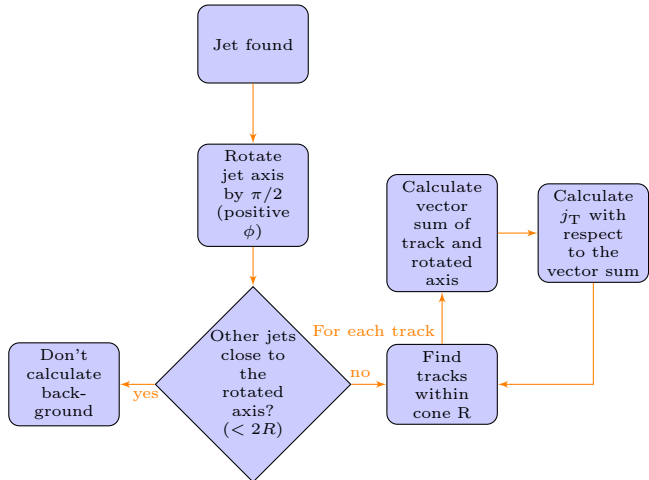


Figure 46: Flowchart representation of the perpendicular cone background procedure

1892 If we don't find other jets in the vicinity we move on to estimate the background.
 1893 We find all tracks within a cone of radius R around the rotated axis and calculate
 1894 j_T of these tracks with respect to the rotated axis.

1895 This background procedure is a part of the reason for using charged tracks
 1896 inside a fixed size cone, instead of jet constituents. To be representative of the
 1897 actual underlying event contribution the size and shape of the background estima-
 1898 tion region should match the area where j_T is calculated. The irregular shape of
 1899 a jet would be hard to take into account when calculating background. Thus the
 1900 regions are made to match by considering fixed size cones for j_T .

1901 One additional consideration is the issue of auto-correlations as the jet axis is
 1902 simply a vector sum of all its constituents. Thus having an additional track in the
 1903 jet from the underlying event moves the jet axis towards this track. Since the axis
 1904 is now closer to the track, it has a smaller j_T value. Assuming a 1 GeV background
 1905 track at the edge of a $R = 0.4$ cone the j_T value would be 0.4 GeV. If this is added
 1906 to a 5 GeV jet, the j_T value becomes 0.33 GeV after the jet axis moves. In a 50 GeV
 1907 jet it would be 0.39 GeV. This is a region where the inclusive j_T distribution is
 1908 dominated by background. The distribution is also steeply falling. Overestimating
 1909 the background can lead to a situation where the background estimation exceeds
 1910 the inclusive distribution.

1911 To take this effect into account we can't use a fixed axis for background, but
 1912 it has to behave like a jet would when additional tracks are added. Thus before
 1913 calculating j_T values we make a vector sum of the track and the axis used for back-
 1914 ground, which is either the perpendicular cone axis or the random axis depending
 1915 on the background method. In each case the momentum of this background axis

1916 is assumed to be the same as the jet which initiated the background estimation.
1917 In p–Pb data there is on average about one underlying event track in a $R = 0.4$
1918 cone. If there would be more, one should consider taking the vector sum of all
1919 tracks inside the cone. As there is usually only one track and if there are more it's
1920 unlikely that more than one has high momentum, taking the vector sum track-by-
1921 track should be enough.

1922 4.4.2 Random background

1923 In the random background method we look at all tracks in the event, except for
1924 tracks close to jets found by the jet algorithm. We randomly assign new η and ϕ
1925 values to all tracks using uniform distributions with $|\eta| < 1.0$. p_T values are kept
1926 the same. To increase statistics there is a possibility to create a number of random
1927 tracks for each actual track. In the analysis we do this 10 times for each track.
1928 Again the track p_T value is kept the same.

1929 We create a random jet cone from uniform η and ϕ distributions. Here $|\eta| <$
1930 0.25. Now we calculate j_T of the random tracks with respect to the random cone
1931 axis. As in the perpendicular cone method auto-correlations are added before
1932 calculating j_T .

1933 Comparison between perpendicular cone and random background in Figure 47.
1934 The advantage of the random background method is that the procedure can be
1935 repeated several times for each event, which allows producing additional statistics.
1936 However, it seems that, especially in the highest $p_{T,jet}$ bins there is some jet con-
1937 tribution left at the high end. Naturally there is no correlation between the tracks
1938 and the background axis, but if some high momentum tracks originating from jets
1939 were not subtracted and happen to hit the edge of the background cone, they can
1940 increase the high j_T yield in the background estimation.

1941 We observe that the results from perpendicular cone background show no ob-
1942 servable change between $p_{T,jet}$ bins. It is a good indication that the background is
1943 actually dominated by the underlying event over the entire j_T region.

1944 Thus as a primary method of background estimation the perpendicular cone
1945 method is used. The random background method is used to estimate systematic
1946 contributions by comparing the final results obtained with this method to the
1947 results obtained from the perpendicular cone method.

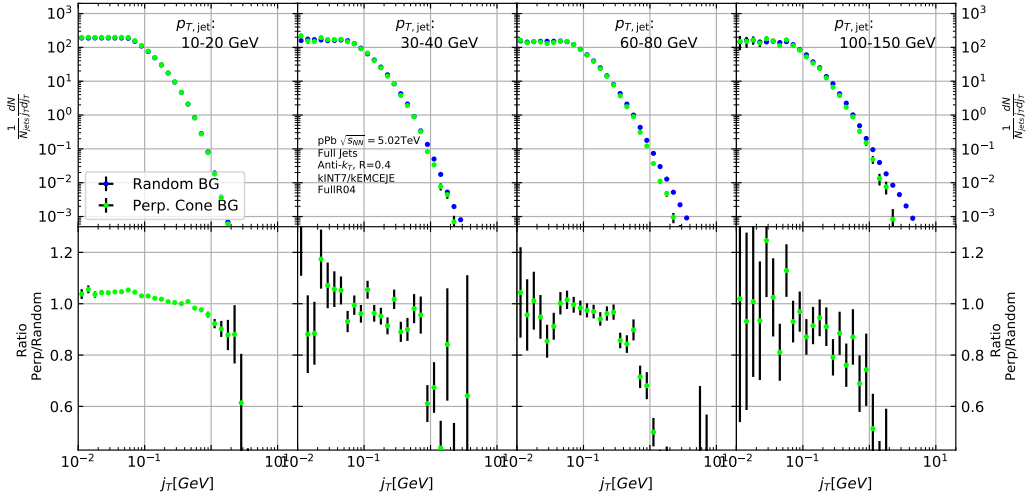


Figure 47: j_T background with two different methods

1948 4.5 Fitting

1949 After unfolding and background subtraction the resulting signal distributions are
 1950 fitted with a 2 component function shown in Eq. 66. Gaussian distribution is used
 1951 for low j_T and an inverse gamma function is used for high j_T . The Gaussian is
 1952 taken to have the center at $j_T = 0$. In total this gives 5 parameters. The fitting
 1953 procedure was inspired by the dihadron j_T analysis by ALICE [277]. The complete
 1954 fitting function is

$$\frac{1}{N_{\text{jets}} j_T \text{d}j_T} \frac{\text{d}N}{\text{d}j_T} = \frac{B_2}{B_1 \sqrt{2\pi}} e^{-\frac{j_T^2}{2B_1^2}} + \frac{B_3 B_5^{B_4}}{\Gamma(B_4)} e^{-\frac{B_5}{j_T^{B_4+1}}}. \quad (66)$$

1955 To achieve stable results the fitting is performed in two steps. First both
 1956 components are fitted separately. Gaussian component is fitted to the low end of
 1957 j_T . Inverse gamma component is fitted to j_T above 1 GeV/c. After getting the
 1958 results from the individual fits they are combined into a single function with initial
 1959 values from the individual results and an additional fit is performed.

1960 After getting the fit function $\sqrt{\langle j_T^2 \rangle}$ (RMS) and yield values are extracted
 1961 separately from each component. The narrow component RMS is

$$\sqrt{\langle j_T^2 \rangle} = \sqrt{2} B_1, \quad (67)$$

1962 and the wide component RMS value is calculated as

$$\sqrt{\langle j_T^2 \rangle} = \frac{B_5}{\sqrt{(B_4 - 2)(B_4 - 3)}}, \quad (68)$$

¹⁹⁶³ where it is required that $B_4 > 3$.

¹⁹⁶⁴ The statistical errors can be calculated with the general error propagation
¹⁹⁶⁵ formulas. As a result one gets errors for the narrow component RMS

$$\delta \sqrt{\langle j_T^2 \rangle} = \sqrt{2} \delta B_1 \quad (69)$$

¹⁹⁶⁶ and for the wide component RMS

$$\delta \sqrt{\langle j_T^2 \rangle} = \sqrt{\left(\frac{(5 - 2B_4) B_5 \delta B_4}{(2(B_4 - 2)(B_4 - 3))^{\frac{3}{2}}} \right)^2 + \left(\frac{\delta B_5}{\sqrt{(B_4 - 2)(B_4 - 3)}} \right)^2} \quad (70)$$

5 Systematic uncertainties

The main systematic uncertainties in this analysis come from the background estimation, the unfolding procedure and uncertainty in the tracking efficiency. The systematics in background estimation were studied using an alternative method to extract the background, the random background method and the uncertainty in tracking was studied by varying tracking efficiencies in a PYTHIA simulation.

The systematic uncertainty that arises from the unfolding procedure is estimated by performing the unfolding with two separate methods. Data corrected by the iterative unfolding method are used as the results and the SVD unfolding method is employed to estimate the uncertainty. In a PYTHIA closure test the true distribution was in general found to be between the unfolded distributions from the iterative and SVD method. The difference between the methods when unfolding data should give a reasonable estimate of the unfolding uncertainty. The resulting uncertainty is below 8% for both wide and narrow component RMS.

5.1 Background

The uncertainty coming from background calculation is estimated by subtracting the background separately for the perpendicular cone and random background methods. Comparisons of the resulting signal distributions are shown in Figure 48.

Fits are then performed on both perpendicular cone and random background signals. Difference between them is taken as the systematic uncertainty. The fits for individual bins from the random background method are shown in Figure 49. Resulting differences between the methods for different components are shown in Figure 50. The dotted lines are put at $\pm 5\%$ for the narrow component and at $\pm 8\%$ for the wide component. These are taken as systematic estimates for the entire $p_{T,jet}$ range.

5.2 Unfolding

Unfolding is the second major source of systematic uncertainty. To estimate the uncertainty related to the unfolding procedure several checks are performed. The main systematic uncertainty estimation comes from comparing results performed using both SVD and Bayesian unfolding. Difference between the methods is taken as the systematic uncertainty. Since SVD unfolding does not have a two dimensional option, the unfolding is done bin by bin.

As in the background systematic estimation, fits are performed for both cases separately. Resulting differences between the methods for different components are shown in Figure 51. The dotted lines are at $\pm 8\%$ for both components. These are taken to be the systematic uncertainty related to unfolding.

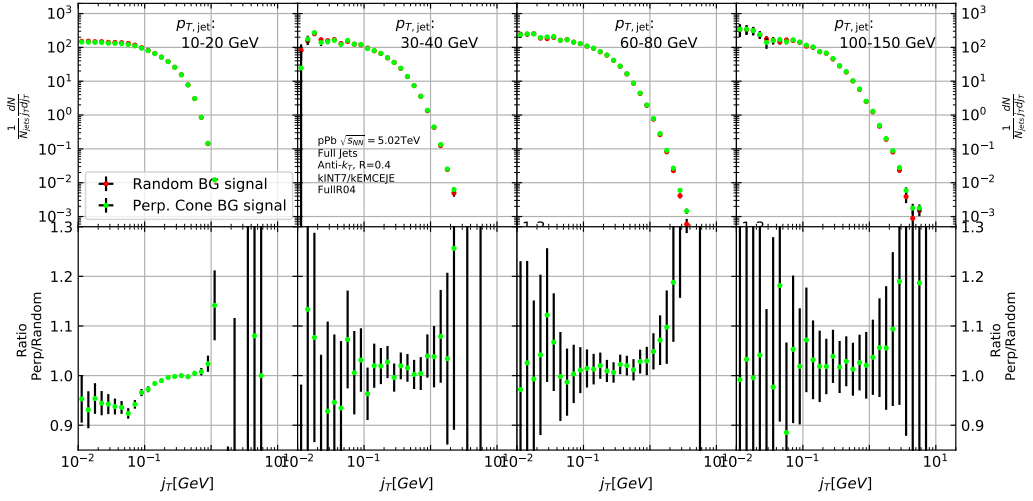


Figure 48: Comparison of the effect of background method on j_T signal

Several other systematic checks were performed with the Bayesian unfolding procedure. They are described in the following sections. As these are small compared to the main uncertainty they are not included separately.

5.2.1 Effect of number of iterations

The iterative unfolding algorithm permits the change of number of iterations. The unfolding procedure was carried out using different numbers of iterations. The results from these different cases are shown in Figure 52. The results are compared to the default unfolding algorithm with 4 iterations. The difference in results between the different cases is mostly less than 2.5%.

5.2.2 Effect of different prior

The iterative algorithm requires a prior estimate of the shape of the distribution. As a default prior the truth (particle level) distribution is used. To test the effect of changing the prior we instead use the unfolded j_T distribution as prior. The results are compared to the unfolding algorithm with the default prior. This is shown in Figure 53. The difference in results between the different cases is mostly less than 2.5%.

5.2.3 Effect of p_T truncation

As an additional check the unfolding is carried out with different $p_{T,jet}$ truncation values. By default the full range of $p_{T,jet} > 5\text{GeV}$ is used. We test the unfolding

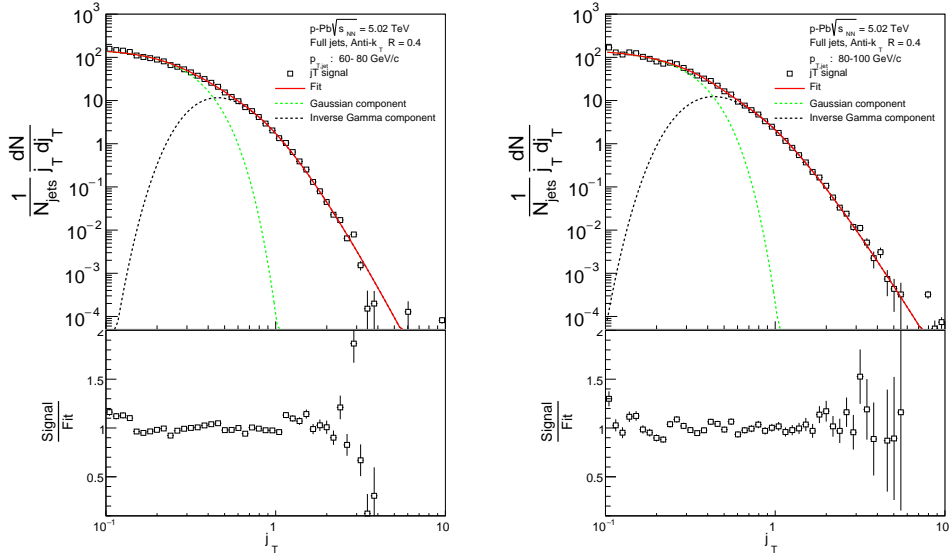


Figure 49: j_T signal with random background subtraction fits in different jet p_T bins

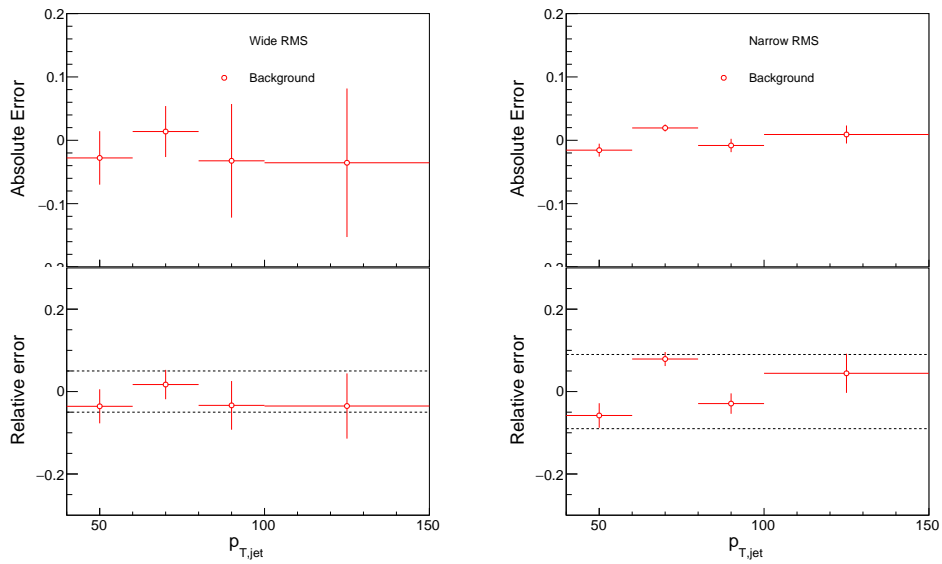


Figure 50: Differences between perpendicular cone and random background subtraction in the resulting RMS values

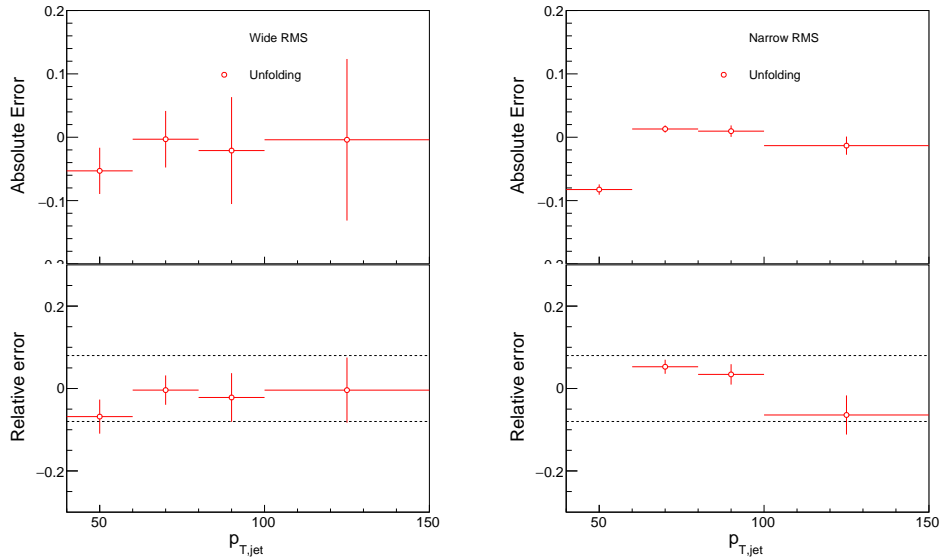


Figure 51: Differences between Bayesian and SVD unfolding in the resulting RMS values

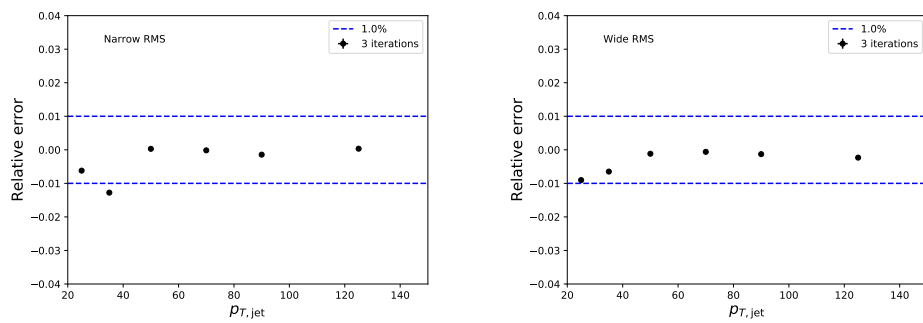


Figure 52: Unfolding with different number of iterations

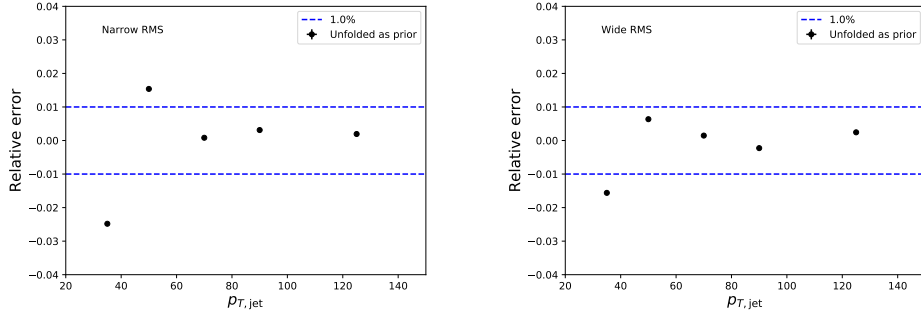


Figure 53: Effect of changing prior from true distribution in PYTHIA to the unfolded distribution

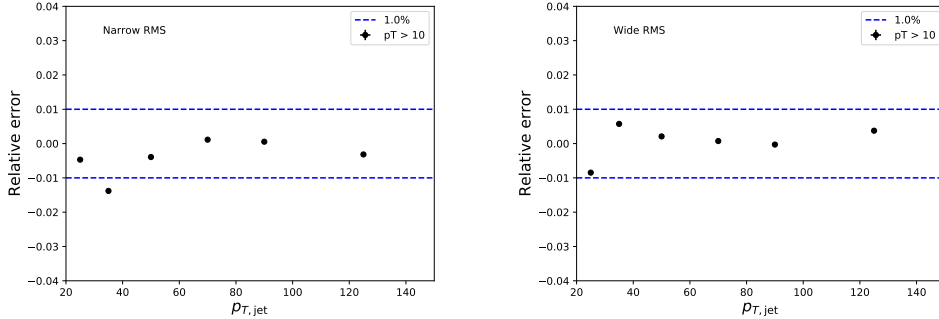


Figure 54: Effect of changing minimum jet p_T used in unfolding from 5 to 10 GeV

2022 by only using the response matrix for $p_{T,\text{jet}} > 10 \text{ GeV}$. The results of this test are
2023 shown in Figure 54. The effects are strongest in the lower $p_{T,\text{jet}}$ bins. Also in this
2024 case the difference is less than 2.5 % in all $p_{T,\text{jet}}$ bins.

2025 5.3 Tracking

2026 Systematic effects originating from uncertainty in the tracking efficiency are es-
2027 timated through a PYTHIA simulation, where an artificial inefficiency of 3% is
2028 introduced i.e. 3 % of tracks are randomly removed from each event. The effect
2029 of this artificial inefficiency is shown in Figure 55. The systematic uncertainties
2030 assigned to tracking efficiency are 4% for the narrow component and 5% for the
2031 wide component.

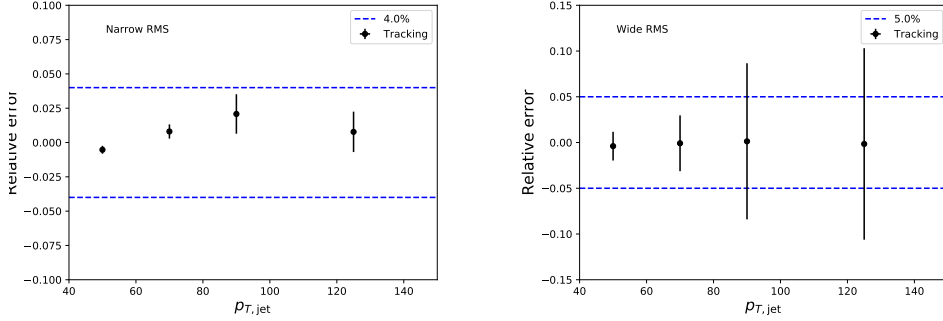


Figure 55: Relative systematic uncertainties resulting from uncertainty in tracking efficiency

2032 5.4 EMCAL clusters

2033 The analysis uses EMCAL clusters only in the reconstruction of jets. Thus the only
 2034 way uncertainty in EMCAL performance can affect the results is through modifica-
 2035 tion of jet momentum or axis.

2036 Uncertainty related to the EMCAL energy scale was estimated by scaling cluster
 2037 energies up and down by 2 % in a PYTHIA particle level simulation. Similarly
 2038 the jet momentum was scaled by $\pm 2\%$ when determining the jet p_T bin. In this
 2039 analysis EMCAL is used only in jet reconstruction, not for calculating j_T . The only
 2040 ways EMCAL uncertainty can affect the analysis are changes in jet energy and jet
 2041 axis. Jet axis shouldn't significantly change, so the main contribution should be
 2042 changes in jet p_T bin.

2043 The resulting differences in the inclusive j_T distributions are shown in Fig-
 2044 ure 56. Qualitatively the effect of scaling cluster energies is the same as scaling
 2045 the jet energies.

2046 Like in the previous cases fits are performed for the unscaled case and for cases
 2047 with $\pm 2\%$ scaling. The resulting systematic uncertainties are shown in Figure 57.
 2048 The uncertainty is taken to be 1% for both components.

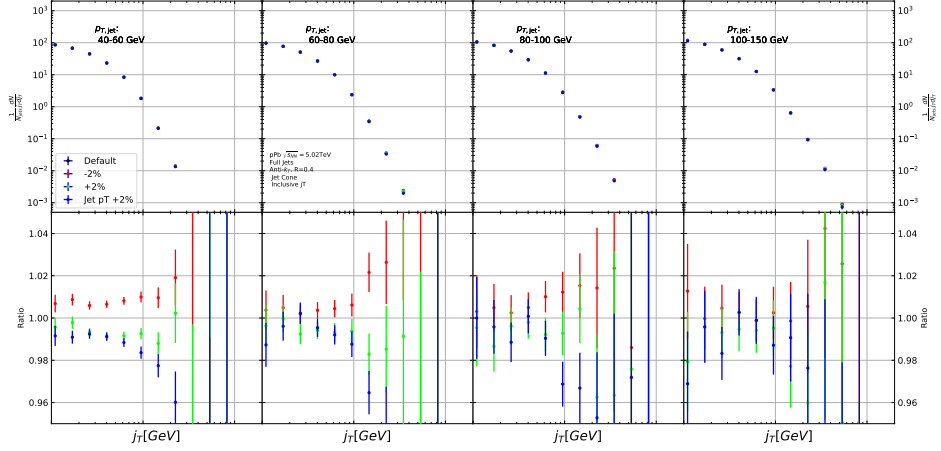


Figure 56: Results from PYTHIA simulations with Cluster energies scaled up and down by 2 %. Additionally jet momenta were scaled by 2 % when determining the jet p_T bin.

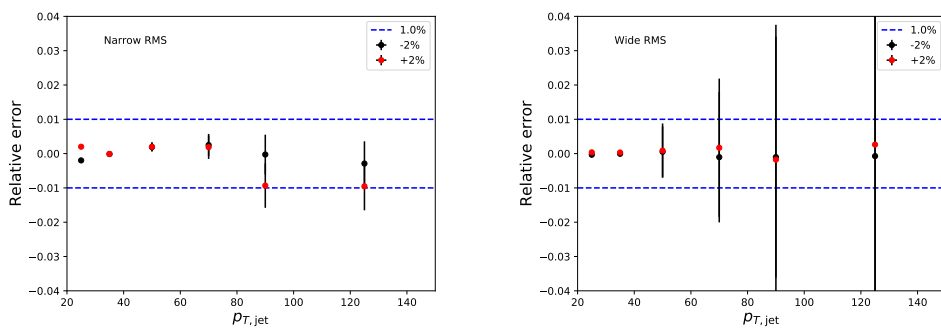


Figure 57: Relative systematic uncertainties resulting from cluster energy uncertainty.

2049 5.5 Summary of systematic uncertainties

2050 The different source of the systematic uncertainty are considered as uncorrelated
2051 and the values of each source are summed in quadrature. Resulting systematic
2052 uncertainties are shown in Table 4. The different source of the systematic un-
2053 certainty are considered to be uncorrelated and are thus combined bin-by-bin in
2054 quadrature to get the total systematic uncertainties. The resulting uncertainty
2055 is approximately 10 % for the wide component RMS and 13 % for the narrow
2056 component RMS.

Table 4: Summary of systematic uncertainties

Systematic	Wide RMS	Narrow RMS
Background	5 %	9 %
Unfolding	8 %	8 %
Tracking	4 %	5 %
EMCal	1 %	1 %
Total	10 %	13%

6 Results

In this section I present the final results for j_T signals. After unfolding and subtracting the background contribution we get the final j_T distributions. Figure 58 shows j_T distributions for two different $p_{T,jet}$ bins with $60 \text{ GeV} < p_{T,jet} < 80 \text{ GeV}$ and $100 \text{ GeV} < p_{T,jet} < 150 \text{ GeV}$. The distributions get wider with increasing $p_{T,jet}$. In part this is explained by kinematics; In a jet cone the cone size sets limits on the possible j_T values. For a given $p_{T,track}$ the maximum j_T value is approximately

$$j_{T\max} \approx R \cdot p_{T,track}, \quad (71)$$

using the small angle approximation.

We fit the distribution using the two component fit function presented in Section 4.5. These are also shown in Figure 58. Fitting a Gaussian alone to the entire j_T distribution will produce a similar result as the Gaussian component in the two component fit. Thus the gaussian fit alone can't describe the full jet j_T distribution.

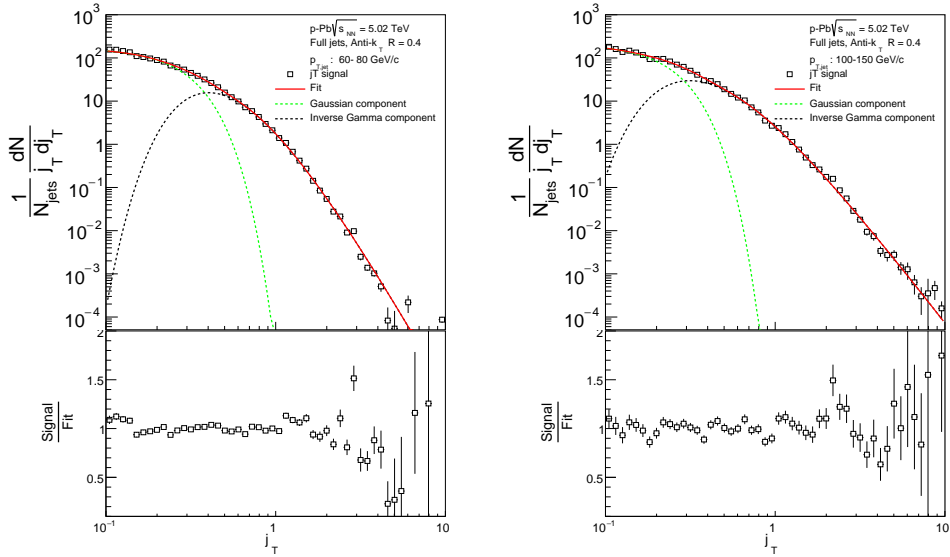


Figure 58: j_T signal distributions fitted with the two component model are shown in different jet p_T bins.

To characterise the widening of the j_T distribution we can then extract the RMS, i.e. $\sqrt{\langle j_T^2 \rangle}$, values of the fits. Resulting RMS values with systematic errors are shown separately for the two components in Figure 59. Here it is seen that the width of the narrow component shows only a weak dependence on the transverse

momentum of the jet, $p_{T,jet}$. The RMS value of the wide component on the other hand increases with increasing $p_{T,jet}$.

The RMS values for both components are compared to PYTHIA and Herwig simulations as shown in Figure 60. All the PYTHIA models reproduce the data well, both the wide and narrow component. For the narrow component Herwig gives RMS values comparable to the data. On the other hand, Herwig produces larger wide component $\sqrt{\langle j_T^2 \rangle}$ values than data and PYTHIA, and this difference seems to get larger with increasing $p_{T,jet}$.

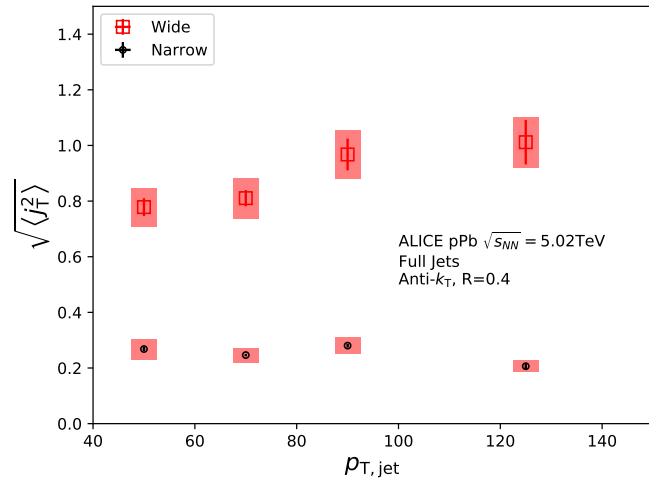


Figure 59: RMS values extracted from the fits are shown for the Gaussian (narrow) and inverse gamma (wide) components.

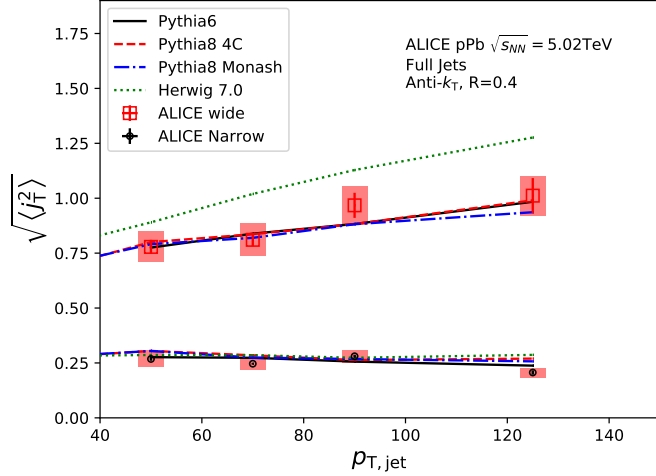


Figure 60: RMS values extracted from the fits are compared to Monte Carlo models. PYTHIA reproduces the data well for both the narrow and wide components. Herwig produces wider distributions.

2082 6.1 High multiplicity events

2083 The analysis was repeated taking only events with high multiplicity. Three dif-
 2084 ferent multiplicity percentile cuts were used; 10 %, 1 % and 0.1 %. The centrality
 2085 estimations were given by V0A. Resulting j_T signal distributions are shown in Fig-
 2086 ure 61. From the figure one can observe no modification within the errors when
 2087 tighter multiplicity cuts are introduced.

2088 As described in Section 1.5 no conclusive evidence of jet modification in
 2089 p–Pb collisions has been observed. However, all previous observations have been
 2090 done for minimum bias events. Most observables are based on measuring yield
 2091 instead of jet shape and are thus sensitive to biases in the centrality selection.
 2092 No previous jet shape measurements have been performed in high multiplicity
 2093 p–Pb events, where collective motion was observed.

2094 As the statistics are limited in the high multiplicity runs, it was hard to achieve
 2095 stable fits to the distributions. Thus the RMS values are not shown.

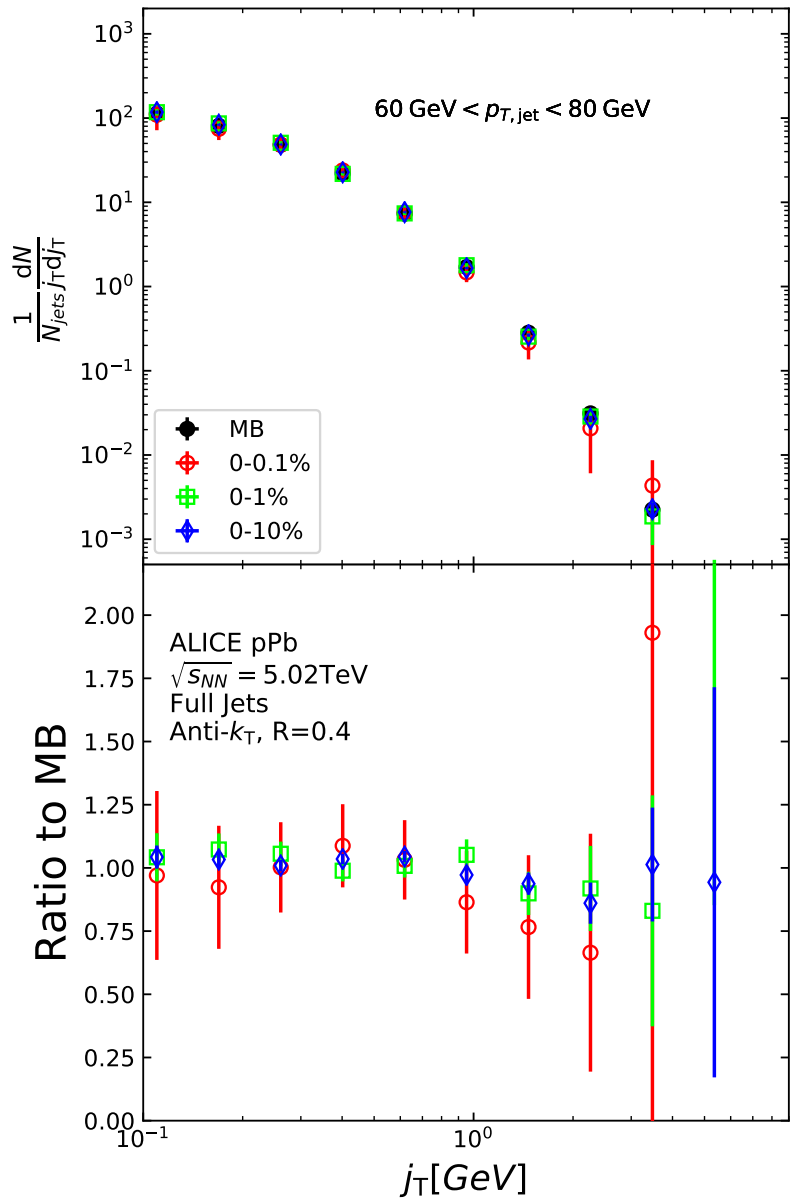


Figure 61: j_T distributions are shown for various multiplicity bins in p–Pb collisions.

2096 7 Discussions

2097 7.1 Comparing dihadron and jet j_T results

2098 The jet fragmentation transverse momentum j_T has been studied previously at
2099 ALICE using dihadron correlations [277]. The study took the leading hadron in
2100 each event and calculated j_T for any near-side tracks with respect to the leading
2101 hadron. Thus there is no kinematical limit to j_T from the jet cone. In the analysis
2102 the background shape is estimated using pairs with large $\Delta\eta$. The normalisation of
2103 the background is done when fitting the j_T distribution. The inclusive distribution
2104 is fitted with a three component function, where one of the components is the
2105 background contribution. After subtracting the background, what remains is the
2106 signal distribution characterised by the two components. The resulting signal
2107 distribution from the analysis is shown in Figure 62. The analysis was the first to
2108 introduce this factorisation of j_T into components.

2109 To constrain the effects from kinematical differences between $p_{T,\text{trigger}}$ bins the
2110 analysis used bins of the fragmentation variable x_{\parallel} , which is the projection of the
2111 associated particle momentum to the trigger particle normalised by the trigger
2112 particle momentum

$$x_{\parallel} = \frac{\vec{p}_t \cdot \vec{p}_a}{\vec{p}_t^2}. \quad (72)$$

2113 The RMS results from the fitting in both pp and p–Pb collisions are shown in
2114 Figure 63. Qualitatively the results are similar to jet j_T results. The RMS value
2115 of the wide component has an increasing trend with respect to $p_{T,t}/p_{T,jet}$, while
2116 the RMS value of the narrow component stays constant. Both components are
2117 well described by PYTHIA simulations. As seen in the figures there is no difference
2118 between minimum bias pp and p–Pb results in the dihadron analysis.

2119 Comparison between RMS values in dihadron j_T [277] and jet j_T is shown in
2120 Figure 64. The dihadron trigger p_T bins are converted to jet p_T bins and vice versa.
2121 Bin-by-bin comparison is still not possible, but general features can be identified.

2122 The trends are similar in dihadron and jet j_T results. Wide component RMS
2123 values tend to increase with increasing $p_{T,\text{trigger}}/p_{T,jet}$. For $x_{\parallel} < 0.4$ Narrow com-
2124 ponent RMS increases slightly at low $p_{T,\text{trigger}}$ in dihadron analysis. This trend
2125 changes between x_{\parallel} bins; In larger x_{\parallel} bins the narrow component RMS is closer
2126 to constant as is the case for jet j_T .

2127 The most striking difference is that dihadron j_T gives wider distributions with
2128 larger RMS values. There are several possible causes for this difference. First, in
2129 jet analysis the cone size limits width and thus the RMS values. The effect of this
2130 limitation can be studied by changing the cone size as is described in Section 7.1.1.

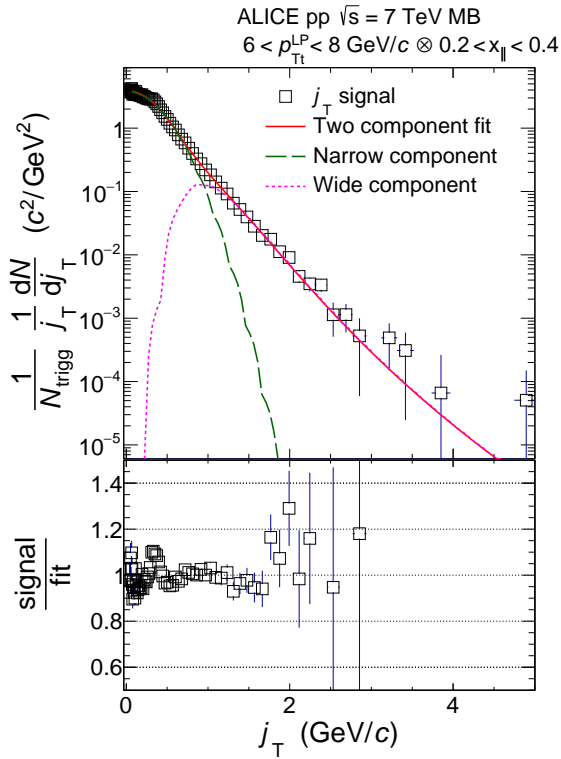


Figure 62: Measured j_T signal distribution using dihadron correlations is shown for $6 < p_{Tt} < 8$ and $0.2 < x_{||} < 0.4$. The distribution is fitted with the same two component model used in this thesis.

2131 Second, the leading track is an imperfect estimate of the jet/original parton.
 2132 Because the leading track in general is at an angle compared to the jet axis, the
 2133 resulting j_T values are different. In practice the jet axis found by the jet finding
 2134 algorithm tends to minimize the average j_T of jet constituents. Thus the yield
 2135 at high j_T is limited and the RMS values are smaller. The effect of having the
 2136 leading hadron as reference instead of the jet axis is discussed in Section 7.1.2

2137 Third, the results from the dihadron analysis are done in $p_{T,\text{trigger}}$ bins. This
 2138 favours hard jets, i.e. jets where the leading hadron carries a large momentum
 2139 fraction and the jet multiplicity is small. In $p_{T,\text{jet}}$ bins jets are more likely to be
 2140 soft, i.e. they have a small leading momentum fraction and high multiplicity jets.

2141 7.1.1 Different R parameters

2142 The size of the jet cone gives a limit for j_T . For a track with a fixed momentum
 2143 p this is a hard limit. This is conveniently seen as $j_{T,\text{max}}$ can be given in terms of
 2144 cone size R and momentum p . In the small angle approximation limit

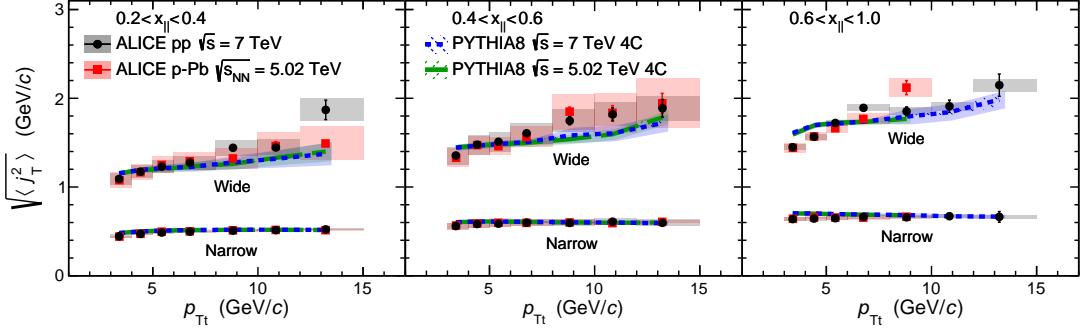


Figure 63: RMS values of the narrow and wide j_T components in the dihadron correlation analysis. Results from pp collisions at $\sqrt{s} = 7$ TeV (circular symbols) and from p–Pb collisions at $\sqrt{s_{NN}} = 5.02$ TeV (square symbols) are compared to PYTHIA 8 tune 4C simulations at $\sqrt{s} = 7$ TeV (short dashed line) and at $\sqrt{s} = 5.02$ TeV (long dashed line). Different panels correspond to different x_{\parallel} bins with $0.2 < x_{\parallel} < 0.4$ on the left, $0.4 < x_{\parallel} < 0.6$ in the middle, and $0.6 < x_{\parallel} < 1.0$ on the right. The statistical errors are represented by bars and the systematic errors by boxes. [277]

$$j_{T,\max} \approx p \cdot R. \quad (73)$$

2145 Thus for tracks with $p_{T,\text{track}} < p_{T0}$, must be $j_T < p_{T0} \cdot R$. This illustrated in
2146 Figure 65.

2147 We studied the effect of cone sizes on j_T distribution with a PYTHIA simulation.
2148 Distributions with different cone sizes in different $p_{T,\text{jet}}$ bins are shown in Figure 66.
2149 The increase of high j_T with increasing cone size, R , is clearly seen in the individual
2150 j_T distributions. At low j_T there is no change within the errors.

2151 When looking at the RMS values from wide component we see an increase
2152 or decrease of about 10% when going from $R = 0.4$ to $R = 0.5$ or $R = 0.3$,
2153 respectively. This is seen in Figure 67. The message from narrow component RMS
2154 values is less clear. At low jet p_T the behaviour is similar, but at high p_T the order
2155 is reversed.

2156 7.1.2 Leading tracks versus jet as reference

2157 In comparison to the leading hadron the jet axis from jet reconstruction should
2158 provide a better estimate of the original parton. The assumption is that because
2159 the leading hadron is an imperfect estimate of the jet axis, low j_T tracks should
2160 on average be shifted to higher j_T .

2161 Because the leading track is at an angle compared to the jet axis, the resulting
2162 j_T values are different. In practice the jet axis found by the jet finding algorithm

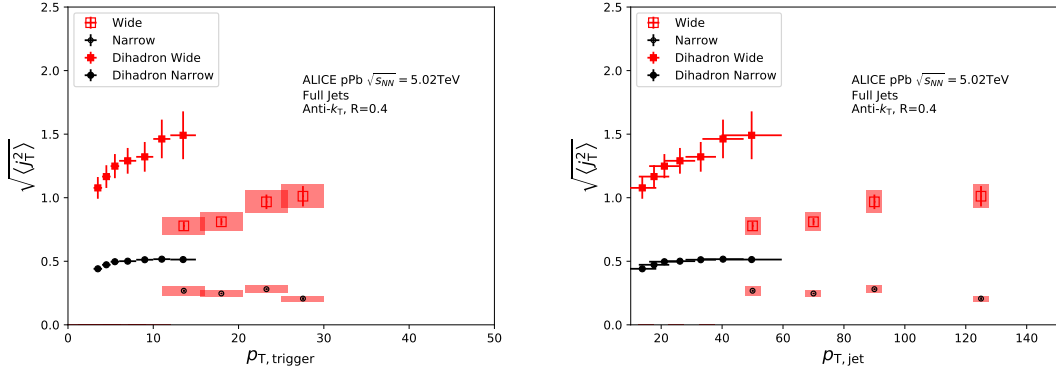


Figure 64: Jet j_T results are compared to results obtained in the dihadron analysis. Dihadron trigger p_T bins are converted to jet p_T bins using observed mean $p_{T,jet}$ values in $p_{T,trigger}$ bins. Dihadron results are for $0.2 < x_{||} < 0.4$.

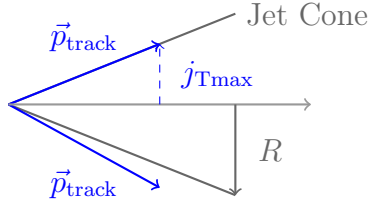


Figure 65: j_T has maximum value defined by the cone size and track momentum \vec{p}_{track}

tends to minimise the average j_T of jet constituents, as at least the hardest constituents should be close to the jet axis. Thus the yield at high j_T is reduced and the RMS values get smaller. On the other hand, when using the leading hadron as a reference, it is naturally missing from the set of tracks for which j_T is calculated. This causes a decrease in the yield at low j_T .

We performed a PYTHIA study where j_T was calculated with respect to the leading track momentum, instead of the jet axis. The results are shown in Figure 68. The resulting j_T distributions are significantly wider than j_T distributions from using the jet axis as reference. The effect seems to be larger than that seen in comparing different R values.

A direct comparison between jet and dihadron j_T measurements is not possible. But combined with the R dependence of $\sqrt{\langle j_T^2 \rangle}$ the difference between $\sqrt{\langle j_T^2 \rangle}$ values in jet and dihadron analyses can be quantitatively understood.

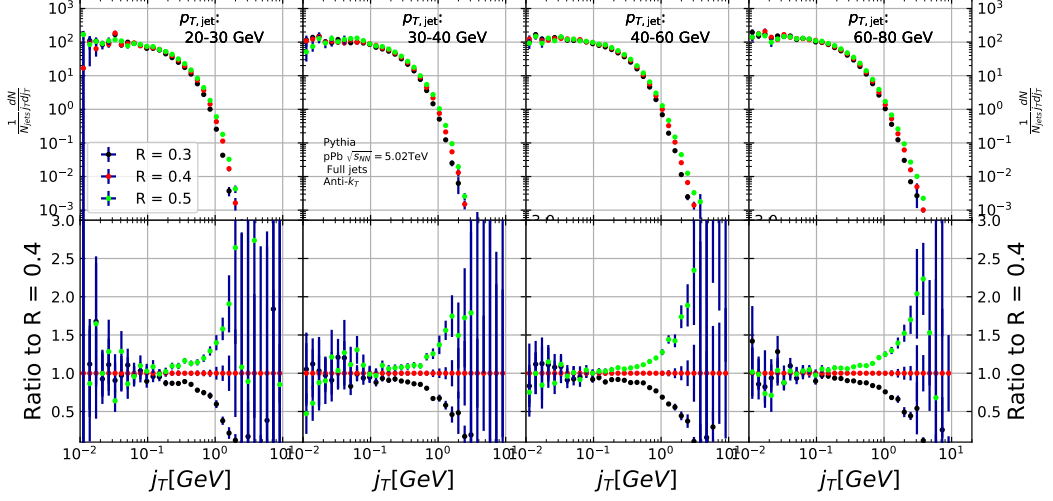


Figure 66: Effect of changing cone size on j_T distributions. The change is done both for the R parameter in the anti- k_T algorithm, and for the size of the cone where j_T is calculated.

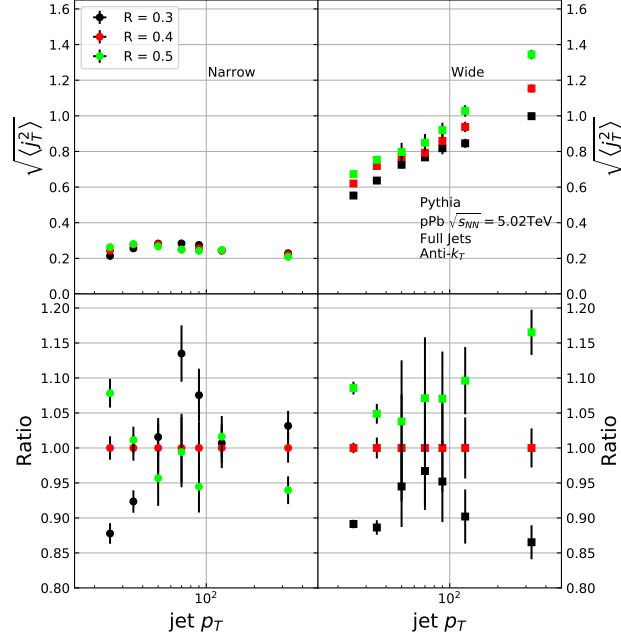


Figure 67: Effect of changing R parameter in jet finding on narrow and wide component RMS values. Wide component RMS values increase with increasing cone size.

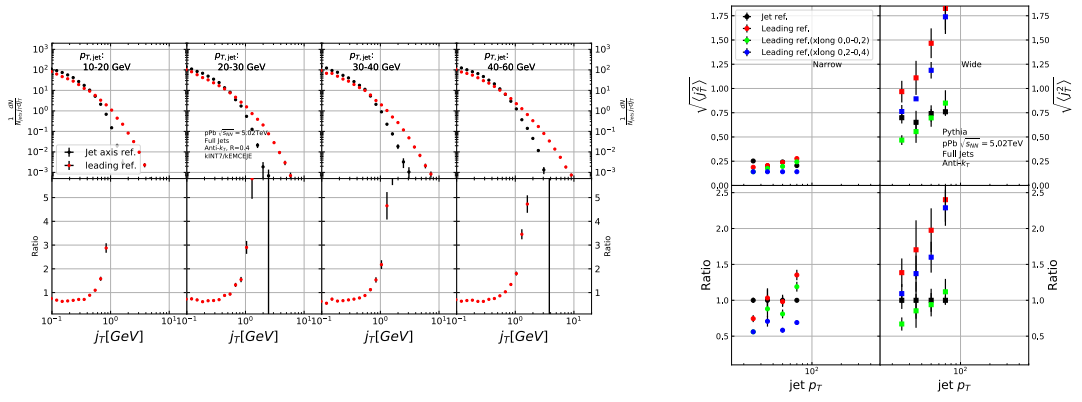


Figure 68: Results of calculating j_T with respect to the leading hadron, instead of the jet axis in a PYTHIA simulation are shown.

2176 8 Summary

2177 In this thesis I have studied the jet fragmentation transverse momentum at
2178 $\sqrt{s_{NN}} = 5.02$ TeV in p–Pb collisions. The analysis was performed using jets
2179 reconstructed with the anti- k_T algorithm. The resulting j_T distributions were
2180 fitted with a two component model, which allows us to separate two distinct
2181 components. The width of the narrow component was found to depend weakly
2182 on jet p_T . The narrow component has been associated with the non-perturbative
2183 hadronisation process. This is consistent with the assumption that hadronisation
2184 is universal, i.e. it doesn't depend on the hard scattering.

2185 The width of the wide component was found to get larger with increasing
2186 $p_{T,jet}$. This is in part explained by the changing kinematical limits when going
2187 to higher $p_{T,jet}$ which allows higher $p_{T,track}$. Additionally the larger phase space
2188 allows stronger parton splitting.

2189 Both the narrow and wide component RMS values were well described by
2190 PYTHIA , but Herwig gave larger RMS values for the wide component than data. In
2191 the narrow component there was no difference between the models. Both describe
2192 the data well. This component was associated with hadronisation. At least in
2193 this context the different hadronisation algorithms of PYTHIA (string model) and
2194 Herwig (cluster model) give similar results.

2195 Similar analysis has been performed with dihadron correlations [277]. Although
2196 a direct comparison between the results is not possible, they are qualitatively com-
2197 patible with each other. The difference is understood to come from the different j_T
2198 reference, the cone size limitation in jet j_T analysis and the kinematical bias that
2199 arises from using $p_{T,trigger}$ bins which favours harder jets than using $p_{T,jet}$ bins. The
2200 dihadron analysis saw no difference between results in pp and p–Pb datasets and
2201 concluded that there were no cold nuclear matter effects. The same is expected
2202 to be true for the jet j_T . This is further supported by the agreement between
2203 PYTHIA and data as PYTHIA results are for pp collisions.

2204 To study possible QGP effects in high multiplicity p–Pb collisions the analysis
2205 was repeated using different multiplicity selections. So far no jet observables have
2206 shown conclusive evidence of modification in p–Pb events. However these are
2207 primarily based on measuring yield, which makes them vulnerable to biases when
2208 selecting for multiplicity. Thus these measurements have been only performed in
2209 minimum bias events. As j_T is based on shape on a per-jet basis, it should not
2210 be sensitive to these selection biases. No effect was seen in any of the multiplicity
2211 selections. However, with the statistics available, the effect should be quite large
2212 ($\gtrsim 20\%$) to be visible.

2213 Naturally the next step would be extending the analysis to Pb–Pb data to
2214 gain better understanding of jet modification. Jet analysis in a heavy-ion collision
2215 with significant contributions from the underlying event has proved challenging [6].

2216 However, experimental methods have improved in recent years. For the j_T analysis
2217 presented in this thesis the main challenge would be the background subtraction
2218 method. Because of anisotropic flow in heavy ion collisions the background inside
2219 the jet cone and a cone perpendicular to it would be different. It's unclear if the
2220 perpendicular cone method can be modified or if a completely new approach is
2221 required.

2222 It has been shown that in Pb–Pb collisions jets become softer and wider because
2223 of medium-induced radiation [6]. On the other hand, the hot medium suppresses
2224 gluon jets more than quark jets. This has the opposite effect, narrowing jets, as
2225 gluon jets are naturally wider than quark jets [278]. How these different effects
2226 combine in j_T needs to be studied.

2227 References

- 2228 [1] D. J. Gross and F. Wilczek, “Asymptotically free gauge theories. i,”
2229 *Physical Review D* **8** no. 10, (1973) 3633.
- 2230 [2] **Particle Data Group** Collaboration, M. Tanabashi *et al.*, “Review of
2231 Particle Physics,” *Phys. Rev.* **D98** no. 3, (2018) 030001.
- 2232 [3] M. L. Perl, E. R. Lee, and D. Loomba, “A Brief review of the search for
2233 isolatable fractional charge elementary particles,” *Mod. Phys. Lett.* **A19**
2234 (2004) 2595–2610.
- 2235 [4] E. Shuryak, “Quantum chromodynamics and the theory of superdense
2236 matter,” *Phys. Reps.* **61** (1980) 71.
- 2237 [5] D. H. Perkins, *Introduction to high energy physics*. 1982.
- 2238 [6] M. Connors, C. Nattrass, R. Reed, and S. Salur, “Jet measurements in
2239 heavy ion physics,” *Rev. Mod. Phys.* **90** (2018) 025005, [arXiv:1705.01974](https://arxiv.org/abs/1705.01974)
2240 [[nucl-ex](#)].
- 2241 [7] J. L. Nagle and W. A. Zajc, “Small System Collectivity in Relativistic
2242 Hadronic and Nuclear Collisions,” *Ann. Rev. Nucl. Part. Sci.* **68** (2018)
2243 211–235, [arXiv:1801.03477](https://arxiv.org/abs/1801.03477) [[nucl-ex](#)].
- 2244 [8] E. S., “Entwurf einer verallgemeinerten relativitätstheorie und einer theorie
2245 der gravitation,” *Monatshefte für Mathematik und Physik* **26** no. 1, (Dec,
2246 1915) A38–A38. <https://doi.org/10.1007/BF01999515>.
- 2247 [9] P. A. M. Dirac and N. H. D. Bohr, “The quantum theory of the emission
2248 and absorption of radiation,” *Proceedings of the Royal Society of London.*
2249 *Series A, Containing Papers of a Mathematical and Physical Character*
2250 **114** no. 767, (1927) 243–265,
2251 <https://royalsocietypublishing.org/doi/pdf/10.1098/rspa.1927.0039>.
2252 <https://royalsocietypublishing.org/doi/abs/10.1098/rspa.1927.0039>.
- 2253 [10] S. Tomonaga, “On a relativistically invariant formulation of the quantum
2254 theory of wave fields,” *Prog. Theor. Phys.* **1** (1946) 27–42.
- 2255 [11] J. S. Schwinger, “Quantum electrodynamics. 2. Vacuum polarization and
2256 selfenergy,” *Phys. Rev.* **75** (1948) 651. [,59(1948)].
- 2257 [12] J. S. Schwinger, “Quantum electrodynamics. I A covariant formulation,”
2258 *Phys. Rev.* **74** (1948) 1439. [,36(1948)].
- 2259

- 2260 [13] R. P. Feynman, “Relativistic cutoff for quantum electrodynamics,” *Phys.*
2261 *Rev.* **74** (1948) 1430–1438.
- 2262 [14] M. L. Krauss, *The Greatest Story Ever Told—So Far: Why Are We Here?*
2263 2017.
- 2264 [15] S. L. Glashow, J. Iliopoulos, and L. Maiani, “Weak Interactions with
2265 Lepton-Hadron Symmetry,” *Phys. Rev.* **D2** (1970) 1285–1292.
- 2266 [16] A. Salam and J. C. Ward, “Electromagnetic and weak interactions,” *Phys.*
2267 *Lett.* **13** (1964) 168–171.
- 2268 [17] S. Weinberg, “A Model of Leptons,” *Phys. Rev. Lett.* **19** (1967) 1264–1266.
- 2269 [18] G. P. S. Occhialini and C. F. Powell, “Nuclear disintegration produced by
2270 slow charged particles of small mass.”. [Nature159,186(1947)].
- 2271 [19] C. M. G. Lattes, G. P. S. Occhialini, and C. F. Powell, “Observations on
2272 the Tracks of Slow Mesons in Photographic Emulsions. 1,” *Nature* **160**
2273 (1947) 453–456. [,99(1947)].
- 2274 [20] R. Bjorklund, W. Crandall, B. J. Moyer, and H. York, “High energy
2275 photons from proton-nucleon collisions,” *Phys. Review* **77** (1950) 213–218.
- 2276 [21] O. Chamberlain, E. Segre, C. Wiegand, and T. Ypsilantis, “Observation of
2277 Anti-protons,” *Phys. Rev.* **100** (1955) 947–950.
- 2278 [22] B. Cork, G. R. Lambertson, O. Piccioni, and W. A. Wenzel, “Anti-neutrons
2279 Produced From Anti-protons in Charge Exchange Collisions,” *Phys. Rev.*
2280 **104** (1957) 1193–1197.
- 2281 [23] L. W. Alvarez, P. Eberhard, M. L. Good, W. Graziano, H. K. Ticho, and
2282 S. G. Wojcicki, “Neutral Cascade Hyperon Event,” *Phys. Rev. Lett.* **2**
2283 (1959) 215–219.
- 2284 [24] R. Armenteros, K. Barker, C. Butler, A. Cachon, and C. York, “Lvi. the
2285 properties of charged v-particles,” *The London, Edinburgh, and Dublin*
2286 *Philosophical Magazine and Journal of Science* **43** no. 341, (1952) 597–611,
2287 <https://doi.org/10.1080/14786440608520216>.
2288 <https://doi.org/10.1080/14786440608520216>.
- 2289 [25] A. Bonetti, R. L. Setti, M. Panetti, and G. Tomasini, “On the existence of
2290 unstable charged particles of hyperprototic mass,” *Il Nuovo Cimento*
2291 (*1943-1954*) **10** no. 12, (Dec, 1953) 1736–1743.
2292 <https://doi.org/10.1007/BF02781667>.

- 2293 [26] R. Plano, N. Samios, M. Schwartz, and J. Steinberger, “Demostration of
 2294 the existence of the σ_0 hyperon and a measurement of its mass,” *Il Nuovo*
 2295 *Cimento (1955-1965)* **5** no. 1, (Jan, 1957) 216–219.
 2296 <https://doi.org/10.1007/BF02812828>.
- 2297 [27] W. B. Fowler, R. P. Shutt, A. M. Thorndike, and W. L. Whittemore,
 2298 “Production of V10 Particles by Negative Pions in Hydrogen,” *Phys. Rev.*
 2299 **91** no. 5, (1953) 1287.
- 2300 [28] W. Heisenberg, “Uber den bay der atomkerne,” *Zeitschrift für Physik* **77**
 2301 (1932) 1–11.
- 2302 [29] M. Gell-Mann, “Symmetries of baryons and mesons,” *Phys. Rev.* **125**
 2303 (1962) 1067.
- 2304 [30] V. E. Barnes *et al.*, “Confirmation of the existence of the Ω^- hyperon,”
 2305 *Phys. Lett.* **12** (1964) 134–136.
- 2306 [31] M. Gell-Mann, “A schematic model of baryons and mesons,” *Phys. Lett.* **8**
 2307 (1964) 214.
- 2308 [32] G. Zweig, “An SU(3) model for strong interaction symmetry and its
 2309 breaking. Version 2,” in *DEVELOPMENTS IN THE QUARK THEORY*
 2310 *OF HADRONS. VOL. 1. 1964 - 1978*, D. Lichtenberg and S. P. Rosen,
 2311 eds., pp. 22–101. 1964.
- 2312 [33] O. Greenberg, “Spin and unitary spin independence in a paraquark model
 2313 of baryons and mesons,” *Phys. Rev. Lett.* **13** (1964) 598–602.
- 2314 [34] H. Fritzsch and M. Gell-Mann, “Current algebra: Quarks and what else?”,
 2315 *eConf C720906V2* (1972) 135–165, [arXiv:hep-ph/0208010](https://arxiv.org/abs/hep-ph/0208010) [hep-ph].
- 2316 [35] **Crystal Ball Collaboration** Collaboration, D. Williams *et al.*,
 2317 “Formation of the Pseudoscalars π^0 , η and η' in the Reaction $\gamma\gamma \rightarrow \gamma\gamma$,”
 2318 *Phys. Rev.* **D38** (1988) 1365.
- 2319 [36] W. Krolikowski, “Vector Gluon Dominance and Rising Drell Ratio for e-
 2320 e+ Annihilation,” *Nuovo Cim.* **A27** (1975) 194.
- 2321 [37] E. D. Bloom *et al.*, “High-Energy Inelastic e p Scattering at 6-Degrees and
 2322 10-Degrees,” *Phys. Rev. Lett.* **23** (1969) 930–934.
- 2323 [38] M. Breidenbach, J. I. Friedman, H. W. Kendall, E. D. Bloom, D. H.
 2324 Coward, H. C. DeStaeler, J. Drees, L. W. Mo, and R. E. Taylor,
 2325 “Observed Behavior of Highly Inelastic electron-Proton Scattering,” *Phys.*
 2326 *Rev. Lett.* **23** (1969) 935–939.

- 2327 [39] “The nobel prize in physics 1990.”
2328 [Https://www.nobelprize.org/prizes/physics/1990/summary/](https://www.nobelprize.org/prizes/physics/1990/summary/). Accessed:
2329 Mon. 8 Apr 2019.
- 2330 [40] J. D. Bjorken, “Asymptotic Sum Rules at Infinite Momentum,” *Phys. Rev.* **179** (1969) 1547–1553.
- 2332 [41] J. D. Bjorken and E. A. Paschos, “Inelastic Electron Proton and gamma
2333 Proton Scattering, and the Structure of the Nucleon,” *Phys. Rev.* **185**
2334 (1969) 1975–1982.
- 2335 [42] R. P. Feynman, “Very high-energy collisions of hadrons,” *Phys. Rev. Lett.*
2336 **23** (1969) 1415–1417. [,494(1969)].
- 2337 [43] D. J. Gross and F. Wilczek, “Ultraviolet behavior of non-abelian gauge
2338 theories,” *Physical Review Letters* **30** no. 26, (1973) 1343–1346.
- 2339 [44] H. D. Politzer, “Reliable perturbative results for strong interactions?,”
2340 *Physical Review Letters* **30** no. 26, (1973) 1346–1349.
- 2341 [45] D. J. Gross and F. Wilczek, “Asymptotically free gauge theories. ii,”
2342 *Physical Review D* **9** no. 4, (1974) 980.
- 2343 [46] H. Georgi and H. D. Politzer, “Electroproduction scaling in an
2344 asymptotically free theory of strong interactions,” *Physical Review D* **9**
2345 no. 2, (1974) 416.
- 2346 [47] “The nobel prize in physics 2004.”
2347 [Https://www.nobelprize.org/prizes/physics/2004/summary/](https://www.nobelprize.org/prizes/physics/2004/summary/). Accessed:
2348 Mon. 8 Apr 2019.
- 2349 [48] H. Fritzsch, M. Gell-Mann, and H. Leutwyler, “Advantages of the color
2350 octet gluon picture,” *Physics Letters B* **47** no. 4, (1973) 365–368.
- 2351 [49] **SLAC-SP-017** Collaboration, J. E. Augustin *et al.*, “Discovery of a
2352 Narrow Resonance in e^+e^- Annihilation,” *Phys. Rev. Lett.* **33** (1974)
2353 1406–1408. [Adv. Exp. Phys.5,141(1976)].
- 2354 [50] **E598** Collaboration, J. J. Aubert *et al.*, “Experimental Observation of a
2355 Heavy Particle J ,” *Phys. Rev. Lett.* **33** (1974) 1404–1406.
- 2356 [51] C. Bacci *et al.*, “Preliminary Result of Frascati (ADONE) on the Nature of
2357 a New 3.1-GeV Particle Produced in e+ e- Annihilation,” *Phys. Rev. Lett.*
2358 **33** (1974) 1408. [Erratum: Phys. Rev. Lett.33,1649(1974)].

- 2359 [52] “The nobel prize in physics 1976.”
 2360 <Https://www.nobelprize.org/prizes/physics/1976/summary/>. Accessed:
 2361 Mon. 8 Apr 2019.
- 2362 [53] J. D. Bjorken and S. L. Glashow, “Elementary Particles and SU(4),” *Phys.
 2363 Lett.* **11** (1964) 255–257.
- 2364 [54] I. Flegel and P. Söding, “Twenty-five years of gluons,” *CERN courier* (2004)
 2365 . <http://cerncourier.com/cws/article/cern/29201>.
- 2366 [55] **TASSO** Collaboration, R. Brandelik *et al.*, “Evidence for Planar Events in
 2367 e+ e- Annihilation at High-Energies,” *Phys. Lett.* **86B** (1979) 243–249.
- 2368 [56] J. K. L. MacDonald, “Successive approximations by the rayleigh-ritz
 2369 variation method,” *Phys. Rev.* **43** (May, 1933) 830–833.
 2370 <http://link.aps.org/doi/10.1103/PhysRev.43.830>.
- 2371 [57] C. Berger *et al.*, “Evidence for gluon bremsstrahlung in e+e annihiliations
 2372 at high energies,” *Physics Letters B* **86** no. 3–4, (1979) 418 – 425. <http://www.sciencedirect.com/science/article/pii/0370269379908694>.
- 2374 [58] M. Kobayashi and T. Maskawa, “CP Violation in the Renormalizable
 2375 Theory of Weak Interaction,” *Prog. Theor. Phys.* **49** (1973) 652–657.
- 2376 [59] “The nobel prize in physics 2008.”
 2377 <Https://www.nobelprize.org/prizes/physics/2008/summary/>. Accessed:
 2378 Mon. 8 Apr 2019.
- 2379 [60] S. W. Herb *et al.*, “Observation of a Dimuon Resonance at 9.5-GeV in
 2380 400-GeV Proton-Nucleus Collisions,” *Phys. Rev. Lett.* **39** (1977) 252–255.
- 2381 [61] **CDF** Collaboration, F. Abe *et al.*, “Observation of top quark production in
 2382 $\bar{p}p$ collisions,” *Phys. Rev. Lett.* **74** (1995) 2626–2631,
 2383 [arXiv:hep-ex/9503002](https://arxiv.org/abs/hep-ex/9503002) [hep-ex].
- 2384 [62] **D0** Collaboration, S. Abachi *et al.*, “Search for high mass top quark
 2385 production in $p\bar{p}$ collisions at $\sqrt{s} = 1.8$ TeV,” *Phys. Rev. Lett.* **74** (1995)
 2386 2422–2426, [arXiv:hep-ex/9411001](https://arxiv.org/abs/hep-ex/9411001) [hep-ex].
- 2387 [63] J. Collins and M. Perry, “Superdense matter: Neutrons or asymptotically
 2388 free quarks?,” *Phys. rev. Lett.* **34** (1975) 1353.
- 2389 [64] K. Rajagopal, “Free the quarks,” *SLAC Beam Line* **31-2** (2001) 9–15.

- 2390 [65] P. Kovtun, D. Son, and A. Starinets, “Viscosity in strongly interacting
 2391 quantum field theories from black hole physics,” *Phys. Rev. Lett.* **94** (2005)
 2392 111601, [arXiv:hep-th/0405231](https://arxiv.org/abs/hep-th/0405231) [hep-th].
- 2393 [66] R. A. Lacey, N. N. Ajitanand, J. M. Alexander, P. Chung, W. G.
 2394 Holzmann, M. Issah, A. Taranenko, P. Danielewicz, and H. Stöcker, “Has
 2395 the qcd critical point been signaled by observations at the bnl relativistic
 2396 heavy ion collider?,” *Phys. Rev. Lett.* **98** (Mar, 2007) 092301.
 2397 <http://link.aps.org/doi/10.1103/PhysRevLett.98.092301>.
- 2398 [67] E. Lofgren, *ACCELERATOR DIVISION ANNUAL REPORTS, 1 JULY*
 2399 *1972 12/31/1974*. Oct, 1975.
 2400 <http://www.osti.gov/scitech/servlets/purl/937059>.
- 2401 [68] D. S. Barton, “Heavy ion program at bnl: Ags, rhic,” in *Proc. 1987 Particle*
 2402 *Accelerator Conference, Washington, D.C., March, 1987.* 1987.
- 2403 [69] I. Vitev and M. Gyulassy, “High p_T tomography of $d + \text{Au}$ and $\text{Au}+\text{Au}$ at
 2404 SPS, RHIC, and LHC,” *Phys. Rev. Lett.* **89** (2002) 252301,
 2405 [arXiv:hep-ph/0209161](https://arxiv.org/abs/hep-ph/0209161) [hep-ph].
- 2406 [70] A. Kovalenko, A. Baldin, A. Malakhov, *et al.*, “Status of the nuclotron,” in
 2407 *Proceedings of EPAC*, vol. 94, pp. 161–164. 1994.
- 2408 [71] “New state of matter created at cern.”
 2409 [Https://home.cern/news/press-release/cern/new-state-matter-created-cern](https://home.cern/news/press-release/cern/new-state-matter-created-cern).
 2410 Accessed: Sat. 6 Apr 2019.
- 2411 [72] **NA61/SHINE** Collaboration, K. Grebieszkow, “Highlights from the
 2412 NA61/SHINE experiment at the CERN SPS,” *PoS CPOD2013* (2013)
 2413 004.
- 2414 [73] **PHENIX** Collaboration, K. Adcox *et al.*, “Formation of
 2415 dense partonic matter in relativistic nucleus-nucleus collisions at RHIC:
 2416 Experimental evaluation by the PHENIX collaboration,” *Nucl.Phys.* **A757**
 2417 (2005) 184–283, [arXiv:nucl-ex/0410003](https://arxiv.org/abs/nucl-ex/0410003) [nucl-ex].
- 2418 [74] **STAR** Collaboration, J. Adams *et al.*, “Experimental and
 2419 theoretical challenges in the search for the quark gluon plasma: The STAR
 2420 Collaboration’s critical assessment of the evidence from RHIC collisions,”
 2421 *Nucl.Phys.* **A757** (2005) 102–183, [arXiv:nucl-ex/0501009](https://arxiv.org/abs/nucl-ex/0501009) [nucl-ex].
- 2422 [75] **BRAHMS** Collaboration, I. Arsene *et al.*, “Quark gluon
 2423 plasma and color glass condensate at RHIC? The Perspective from the

- 2424 BRAHMS experiment,” *Nucl.Phys.* **A757** (2005) 1–27,
 2425 arXiv:nucl-ex/0410020 [nucl-ex].
- 2426 [76] B. Back, M. Baker, M. Ballintijn, D. Barton, B. Becker, *et al.*, “The
 2427 PHOBOS perspective on discoveries at RHIC,” *Nucl.Phys.* **A757** (2005)
 2428 28–101, arXiv:nucl-ex/0410022 [nucl-ex].
- 2429 [77] **LHCb** Collaboration, E. Maurice, “Fixed-target physics at LHCb,” in *5th*
 2430 *Large Hadron Collider Physics Conference (LHCP 2017) Shanghai, China,*
 2431 *May 15-20, 2017.* 2017. arXiv:1708.05184 [hep-ex].
- 2432 [78] S. A. Voloshin, A. M. Poskanzer, and R. Snellings, “Collective phenomena
 2433 in non-central nuclear collisions,” arXiv:0809.2949 [nucl-ex].
- 2434 [79] S. A. Voloshin, A. M. Poskanzer, A. Tang, and G. Wang, “Elliptic flow in
 2435 the Gaussian model of eccentricity fluctuations,” *Phys.Lett.* **B659** (2008)
 2436 537–541, arXiv:0708.0800 [nucl-th].
- 2437 [80] H. Holopainen, H. Niemi, and K. J. Eskola, “Event-by-event
 2438 hydrodynamics and elliptic flow from fluctuating initial state,” *Phys.Rev.*
 2439 **C83** (2011) 034901, arXiv:1007.0368 [hep-ph].
- 2440 [81] **ALICE Collaboration** Collaboration, “Centrality determination of pb-pb
 2441 collisions at $\sqrt{s_{NN}} = 2.76$ tev with alice,” *Phys. Rev. C* **88** (Oct, 2013)
 2442 044909. <http://link.aps.org/doi/10.1103/PhysRevC.88.044909>.
- 2443 [82] M. L. Miller, K. Reygers, S. J. Sanders, and P. Steinberg, “Glauber
 2444 modeling in high energy nuclear collisions,” *Ann.Rev.Nucl.Part.Sci.* **57**
 2445 (2007) 205–243, arXiv:nucl-ex/0701025 [nucl-ex].
- 2446 [83] R. Glauber, “Lectures in theoretical physics,” 1959.
- 2447 [84] A. Białłas, M. Błeszyński, and W. Czyż, “Multiplicity distributions in
 2448 nucleus-nucleus collisions at high energies,” *Nuclear Physics B* **111** no. 3,
 2449 (1976) 461 – 476. <http://www.sciencedirect.com/science/article/pii/0550321376903291>.
- 2451 [85] H. De Vries, C. W. De Jager, and C. De Vries, “Nuclear charge and
 2452 magnetization density distribution parameters from elastic electron
 2453 scattering,” *Atom. Data Nucl. Data Tabl.* **36** (1987) 495–536.
- 2454 [86] **ALICE Collaboration**, B. Abelev *et al.*, “Centrality determination of
 2455 Pb-Pb collisions at $\sqrt{s_{NN}} = 2.76$ TeV with ALICE,” *Phys. Rev.* **C88** no. 4,
 2456 (2013) 044909, arXiv:1301.4361 [nucl-ex].

- 2457 [87] **PHENIX Collaboration** Collaboration, S. Afanasiev *et al.*, “High-pT pion
 2458 Production with Respect to the Reaction Plane in Au + Au Collisions at
 2459 $s_{NN}^{**}(1/2) = 200\text{-GeV},$ ” *Phys. Rev.* **C80** (2009) 054907,
 2460 arXiv:0903.4886 [nucl-ex].
- 2461 [88] D. Kharzeev, E. Levin, and M. Nardi, “Color glass condensate at the LHC:
 2462 Hadron multiplicities in pp, pA and AA collisions,” *Nucl. Phys.* **A747**
 2463 (2005) 609–629, arXiv:hep-ph/0408050 [hep-ph].
- 2464 [89] W.-T. Deng, X.-N. Wang, and R. Xu, “Hadron production in p+p, p+Pb,
 2465 and Pb+Pb collisions with the HIJING 2.0 model at energies available at
 2466 the CERN Large Hadron Collider,” *Phys. Rev.* **C83** (2011) 014915,
 2467 arXiv:1008.1841 [hep-ph].
- 2468 [90] **TOTEM Collaboration**, G. Antchev *et al.*, “First measurement of elastic,
 2469 inelastic and total cross-section at $\sqrt{s} = 13\text{ TeV}$ by TOTEM and overview
 2470 of cross-section data at LHC energies,” *Eur. Phys. J.* **C79** no. 2, (2019)
 2471 103, arXiv:1712.06153 [hep-ex].
- 2472 [91] B. Alver, M. Baker, C. Loizides, and P. Steinberg, “The PHOBOS Glauber
 2473 Monte Carlo,” arXiv:0805.4411 [nucl-ex].
- 2474 [92] P. Romatschke, “New Developments in Relativistic Viscous
 2475 Hydrodynamics,” *Int.J.Mod.Phys.* **E19** (2010) 1–53, arXiv:0902.3663
 2476 [hep-ph].
- 2477 [93] K. A. *et al.* [ALICE Collaboration], “Centrality dependence of the
 2478 charged-particle multiplicity density at mid-rapidity in pb-Pb collisions at
 2479 $\sqrt{s_{NN}} = 2.76\text{ TeV},$ ” *Phys. Rev. Lett.* **106** (2011) . 032301.
- 2480 [94] J.-Y. Ollitrault, “Anisotropy as a signature of transverse collective flow,”
 2481 *Phys. Rev. D* **46** (Jul, 1992) 229–245.
 2482 <http://link.aps.org/doi/10.1103/PhysRevD.46.229>.
- 2483 [95] J.-Y. Ollitrault, “Determination of the reaction plane in ultrarelativistic
 2484 nuclear collisions,” *Phys. Rev. D* **48** (1993) 1132–1139,
 2485 arXiv:hep-ph/9303247 [hep-ph].
- 2486 [96] U. Heinz and P. Kolb, “Early thermalization at rhic,” *Nucl. Phys.* **A702**
 2487 (2002) 269.
- 2488 [97] S. Voloshin and Y. Zhang, “Flow study in relativistic nuclear collisions by
 2489 Fourier expansion of Azimuthal particle distributions,” *Z.Phys.* **C70** (1996)
 2490 665–672, arXiv:hep-ph/9407282 [hep-ph].

- 2491 [98] B. Alver and G. Roland, “Collision geometry fluctuations and triangular
 2492 flow in heavy-ion collisions,” *Phys.Rev.* **C81** (2010) 054905,
 2493 arXiv:1003.0194 [nucl-th].
- 2494 [99] A. Mocsy and P. Sorensen, “The Sound of the Little Bangs,”
 2495 arXiv:1008.3381 [hep-ph].
- 2496 [100] A. P. Mishra, R. K. Mohapatra, P. Saumia, and A. M. Srivastava,
 2497 “Super-horizon fluctuations and acoustic oscillations in relativistic
 2498 heavy-ion collisions,” *Phys.Rev.* **C77** (2008) 064902, arXiv:0711.1323
 2499 [hep-ph].
- 2500 [101] T. Abbott *et al.*, “Azimuthal asymmetries of particles emitted in relativistic
 2501 heavy-ion collisions,” *Phys. Rev. Lett.* **70** (Mar, 1993) 1393–1396.
 2502 <http://link.aps.org/doi/10.1103/PhysRevLett.70.1393>.
- 2503 [102] B. Schenke, S. Jeon, and C. Gale, “Anisotropic flow in $\sqrt{s} = 2.76$ TeV
 2504 Pb+Pb collisions at the LHC,” *Phys.Lett.* **B702** (2011) 59–63,
 2505 arXiv:1102.0575 [hep-ph].
- 2506 [103] K. A. *et al.* [ALICE Collaboration], “Higher harmonic anisotropic flow
 2507 measurements of charged particles in pb-pb collisions at
 2508 $\sqrt{s_{NN}} = 2.76$ TeV,” *Phys. Rev. Lett.* **107** (2011) . 032301.
- 2509 [104] K. Aamodt *et al.*, “Harmonic decomposition of two particle angular
 2510 correlations in pb–pb collisions at,” *Physics Letters B* **708** no. 3–5, (2012)
 2511 249 – 264. <http://www.sciencedirect.com/science/article/pii/S0370269312001013>.
- 2513 [105] L. LD, “On the multiparticle production in high-energy collisions,” *Izv.
 2514 Akad. Nauk Ser. Fiz.* **17** (1953) 51.
- 2515 [106] J. D. Bjorken, “Highly relativistic nucleus-nucleus collisions: The central
 2516 rapidity region,” *Phys. Rev. D* **27** (Jan, 1983) 140–151.
 2517 <https://link.aps.org/doi/10.1103/PhysRevD.27.140>.
- 2518 [107] G. Baym, B. L. Friman, J. P. Blaizot, M. Soyeur, and W. Czyz,
 2519 “Hydrodynamics of Ultrarelativistic Heavy Ion Collisions,” *Nucl. Phys.*
 2520 **A407** (1983) 541–570.
- 2521 [108] H. von Gersdorff, L. McLerran, M. Kataja, and P. V. Ruuskanen, “Studies
 2522 of the hydrodynamic evolution of matter produced in fluctuations in
 2523 p^-p collisions and in ultrarelativistic nuclear collisions,” *Phys. Rev. D* **34**
 2524 (Aug, 1986) 794–810.
 2525 <https://link.aps.org/doi/10.1103/PhysRevD.34.794>.

- 2526 [109] H. Niemi, K. J. Eskola, and R. Paatelainen, “Event-by-event fluctuations in
 2527 a perturbative QCD + saturation + hydrodynamics model: Determining
 2528 QCD matter shear viscosity in ultrarelativistic heavy-ion collisions,” *Phys.
 2529 Rev.* **C93** no. 2, (2016) 024907, [arXiv:1505.02677](https://arxiv.org/abs/1505.02677) [hep-ph].
- 2530 [110] R. Paatelainen, K. J. Eskola, H. Holopainen, and K. Tuominen,
 2531 “Multiplicities and p_T spectra in ultrarelativistic heavy ion collisions from a
 2532 next-to-leading order improved perturbative QCD + saturation +
 2533 hydrodynamics model,” *Phys. Rev.* **C87** no. 4, (2013) 044904,
 2534 [arXiv:1211.0461](https://arxiv.org/abs/1211.0461) [hep-ph].
- 2535 [111] R. Paatelainen, K. J. Eskola, H. Niemi, and K. Tuominen, “Fluid dynamics
 2536 with saturated minijet initial conditions in ultrarelativistic heavy-ion
 2537 collisions,” *Phys. Lett.* **B731** (2014) 126–130, [arXiv:1310.3105](https://arxiv.org/abs/1310.3105) [hep-ph].
- 2538 [112] **ALICE** Collaboration, J. Adam *et al.*, “Correlated event-by-event
 2539 fluctuations of flow harmonics in Pb-Pb collisions at $\sqrt{s_{\text{NN}}} = 2.76$ TeV,”
 2540 *Phys. Rev. Lett.* **117** (2016) 182301, [arXiv:1604.07663](https://arxiv.org/abs/1604.07663) [nucl-ex].
- 2541 [113] J. E. Bernhard, J. S. Moreland, S. A. Bass, J. Liu, and U. Heinz, “Applying
 2542 bayesian parameter estimation to relativistic heavy-ion collisions:
 2543 Simultaneous characterization of the initial state and quark-gluon plasma
 2544 medium,” *Phys. Rev. C* **94** (Aug, 2016) 024907.
 2545 <https://link.aps.org/doi/10.1103/PhysRevC.94.024907>.
- 2546 [114] **ALICE** Collaboration, S. Acharya *et al.*, “Systematic studies of
 2547 correlations between different order flow harmonics in Pb-Pb collisions at
 2548 $\sqrt{s_{\text{NN}}} = 2.76$ TeV,” *Phys. Rev.* **C97** no. 2, (2018) 024906,
 2549 [arXiv:1709.01127](https://arxiv.org/abs/1709.01127) [nucl-ex].
- 2550 [115] **ALICE** Collaboration, S. Acharya *et al.*, “Linear and non-linear flow
 2551 modes in Pb-Pb collisions at $\sqrt{s_{\text{NN}}} = 2.76$ TeV,” *Phys. Lett.* **B773** (2017)
 2552 68–80, [arXiv:1705.04377](https://arxiv.org/abs/1705.04377) [nucl-ex].
- 2553 [116] A. Metz and A. Vossen, “Parton Fragmentation Functions,” *Prog. Part.
 2554 Nucl. Phys.* **91** (2016) 136–202, [arXiv:1607.02521](https://arxiv.org/abs/1607.02521) [hep-ex].
- 2555 [117] R. Placakyte, “Parton Distribution Functions,” in *Proceedings, 31st
 2556 International Conference on Physics in collisions (PIC 2011): Vancouver,
 2557 Canada, August 28-September 1, 2011.* 2011. [arXiv:1111.5452](https://arxiv.org/abs/1111.5452) [hep-ph].
 2558

- 2559 [118] V. N. Gribov and L. N. Lipatov, “Deep inelastic e p scattering in
 2560 perturbation theory,” *Sov. J. Nucl. Phys.* **15** (1972) 438–450. [Yad.
 2561 Fiz.15,781(1972)].
- 2562 [119] G. Altarelli and G. Parisi, “Asymptotic Freedom in Parton Language,”
 2563 *Nucl. Phys.* **B126** (1977) 298–318.
- 2564 [120] Y. L. Dokshitzer, “Calculation of the Structure Functions for Deep
 2565 Inelastic Scattering and e+ e- Annihilation by Perturbation Theory in
 2566 Quantum Chromodynamics.,” *Sov. Phys. JETP* **46** (1977) 641–653. [Zh.
 2567 Eksp. Teor. Fiz.73,1216(1977)].
- 2568 [121] J. Pumplin, D. R. Stump, J. Huston, H. L. Lai, P. M. Nadolsky, and W. K.
 2569 Tung, “New generation of parton distributions with uncertainties from
 2570 global QCD analysis,” *JHEP* **07** (2002) 012, arXiv:hep-ph/0201195
 2571 [hep-ph].
- 2572 [122] **ZEUS, H1** Collaboration, A. M. Cooper-Sarkar, “PDF Fits at HERA,”
 2573 *PoS EPS-HEP2011* (2011) 320, arXiv:1112.2107 [hep-ph].
- 2574 [123] J. Butterworth *et al.*, “PDF4LHC recommendations for LHC Run II,” *J.
 2575 Phys.* **G43** (2016) 023001, arXiv:1510.03865 [hep-ph].
- 2576 [124] T. Sjöstrand and P. Z. Skands, “Transverse-momentum-ordered showers
 2577 and interleaved multiple interactions,” *Eur. Phys. J.* **C39** (2005) 129–154,
 2578 arXiv:hep-ph/0408302 [hep-ph].
- 2579 [125] T. Sjöstrand, S. Ask, J. R. Christiansen, R. Corke, N. Desai, P. Ilten,
 2580 S. Mrenna, S. Prestel, C. O. Rasmussen, and P. Z. Skands, “An
 2581 Introduction to PYTHIA 8.2,” *Comput. Phys. Commun.* **191** (2015)
 2582 159–177, arXiv:1410.3012 [hep-ph].
- 2583 [126] M. Bahr *et al.*, “Herwig++ Physics and Manual,” *Eur. Phys. J.* **C58**
 2584 (2008) 639–707, arXiv:0803.0883 [hep-ph].
- 2585 [127] A. Buckley *et al.*, “General-purpose event generators for LHC physics,”
 2586 *Phys. Rept.* **504** (2011) 145–233, arXiv:1101.2599 [hep-ph].
- 2587 [128] Y. L. Dokshitzer, V. A. Khoze, A. H. Müller, and S. I. Troian, *Basics of
 2588 Perturbative QCD*. Editions Frontières, Gif-sur-Yvette, France, 1991.
- 2589 [129] Y. I. Azimov, Y. L. Dokshitzer, V. A. Khoze, and S. I. Troian, “Similarity
 2590 of parton and hadron spectra in qcd jets,” *Zeitschrift für Physik C
 2591 Particles and Fields* **27** no. 1, (Mar, 1985) 65–72.
 2592 <https://doi.org/10.1007/BF01642482>.

- 2593 [130] B. Andersson, G. Gustafson, G. Ingelman, and T. Sjöstrand, “Parton
 2594 fragmentation and string dynamics,” *Physics Reports* **97** no. 2, (1983) 31 –
 2595 145. <http://www.sciencedirect.com/science/article/pii/0370157383900807>.
- 2596
- 2597 [131] **ALICE Collaboration** Collaboration, K. Aamodt *et al.*, “Suppression of
 2598 Charged Particle Production at Large Transverse Momentum in Central
 2599 Pb–Pb Collisions at $\sqrt{s_{NN}} = 2.76$ TeV,” *Phys.Lett.* **B696** (2011) 30–39,
 2600 [arXiv:1012.1004](https://arxiv.org/abs/1012.1004) [nucl-ex].
- 2601
- 2602 [132] **WA98 Collaboration** Collaboration, M. Aggarwal *et al.*, “Transverse
 2603 mass distributions of neutral pions from Pb-208 induced reactions at
 2604 158-A-GeV,” *Eur.Phys.J.* **C23** (2002) 225–236, [arXiv:nucl-ex/0108006](https://arxiv.org/abs/nucl-ex/0108006)
 [nucl-ex].
- 2605
- 2606 [133] D. G. d’Enterria, “Indications of suppressed high p(T) hadron production
 2607 in nucleus - nucleus collisions at CERN-SPS,” *Phys.Lett.* **B596** (2004)
 32–43, [arXiv:nucl-ex/0403055](https://arxiv.org/abs/nucl-ex/0403055) [nucl-ex].
- 2608
- 2609 [134] **PHENIX Collaboration** Collaboration, A. Adare *et al.*, “Suppression
 2610 pattern of neutral pions at high transverse momentum in Au + Au
 2611 collisions at $s(\text{NN})^{**}(1/2) = 200$ -GeV and constraints on medium
 2612 transport coefficients,” *Phys.Rev.Lett.* **101** (2008) 232301,
[arXiv:0801.4020](https://arxiv.org/abs/0801.4020) [nucl-ex].
- 2613
- 2614 [135] **STAR Collaboration** Collaboration, J. Adams *et al.*, “Transverse
 2615 momentum and collision energy dependence of high p(T) hadron
 2616 suppression in Au+Au collisions at ultrarelativistic energies,”
Phys.Rev.Lett. **91** (2003) 172302, [arXiv:nucl-ex/0305015](https://arxiv.org/abs/nucl-ex/0305015) [nucl-ex].
- 2617
- 2618 [136] A. Dainese, C. Loizides, and G. Paic, “Leading-particle suppression in high
 2619 energy nucleus-nucleus collisions,” *Eur.Phys.J.* **C38** (2005) 461–474,
[arXiv:hep-ph/0406201](https://arxiv.org/abs/hep-ph/0406201) [hep-ph].
- 2620
- 2621 [137] I. Vitev, “Jet tomography,” *J.Phys.* **G30** (2004) S791–S800,
[arXiv:hep-ph/0403089](https://arxiv.org/abs/hep-ph/0403089) [hep-ph].
- 2622
- 2623 [138] C. A. Salgado and U. A. Wiedemann, “Calculating quenching weights,”
Phys.Rev. **D68** (2003) 014008, [arXiv:hep-ph/0302184](https://arxiv.org/abs/hep-ph/0302184) [hep-ph].
- 2624
- 2625 [139] N. Armesto, A. Dainese, C. A. Salgado, and U. A. Wiedemann, “Testing
 2626 the color charge and mass dependence of parton energy loss with
 2627 heavy-to-light ratios at RHIC and CERN LHC,” *Phys.Rev.* **D71** (2005)
 054027, [arXiv:hep-ph/0501225](https://arxiv.org/abs/hep-ph/0501225) [hep-ph].

- 2628 [140] T. Renk, H. Holopainen, R. Paatelainen, and K. J. Eskola, “Systematics of
2629 the charged-hadron p_T spectrum and the nuclear suppression factor in
2630 heavy-ion collisions from $\sqrt{s} = 200$ GeV to $\sqrt{s} = 2.76$ TeV,” *Phys. Rev.*
2631 **C84** (2011) 014906, [arXiv:1103.5308](https://arxiv.org/abs/1103.5308) [hep-ph].
- 2632 [141] **CMS Collaboration** Collaboration, S. Chatrchyan *et al.*, “Study of
2633 high-pT charged particle suppression in PbPb compared to pp collisions at
2634 $\sqrt{s_{NN}} = 2.76$ TeV,” *Eur. Phys. J. C72* (2012) 1945, [arXiv:1202.2554](https://arxiv.org/abs/1202.2554)
2635 [nucl-ex].
- 2636 [142] **PHENIX** Collaboration, S. S. Adler *et al.*, “A Detailed Study of
2637 High-p(T) Neutral Pion Suppression and Azimuthal Anisotropy in Au+Au
2638 Collisions at $s(\text{NN})^{**}(1/2) = 200$ -GeV,” *Phys. Rev. C76* (2007) 034904,
2639 [arXiv:nucl-ex/0611007](https://arxiv.org/abs/nucl-ex/0611007) [nucl-ex].
- 2640 [143] **PHENIX** Collaboration, A. Adare *et al.*, “Azimuthal anisotropy of π^0 and
2641 η mesons in Au + Au collisions at $\sqrt{s_{NN}} = 200$ GeV,” *Phys. Rev. C88*
2642 no. 6, (2013) 064910, [arXiv:1309.4437](https://arxiv.org/abs/1309.4437) [nucl-ex].
- 2643 [144] **ALICE** Collaboration, B. Abelev *et al.*, “Anisotropic flow of charged
2644 hadrons, pions and (anti-)protons measured at high transverse momentum
2645 in Pb-Pb collisions at $\sqrt{s_{NN}}=2.76$ TeV,” *Phys. Lett. B719* (2013) 18–28,
2646 [arXiv:1205.5761](https://arxiv.org/abs/1205.5761) [nucl-ex].
- 2647 [145] **CMS** Collaboration, S. Chatrchyan *et al.*, “Azimuthal anisotropy of
2648 charged particles at high transverse momenta in PbPb collisions at
2649 $\sqrt{s_{NN}} = 2.76$ TeV,” *Phys. Rev. Lett. 109* (2012) 022301, [arXiv:1204.1850](https://arxiv.org/abs/1204.1850)
2650 [nucl-ex].
- 2651 [146] W. H. H. Bethe and, “On the stopping of fast particles and on the creation
2652 of positive electrons,” *Proc. Roy. Soc. Lond. A146* (1934) .
- 2653 [147] L. D. Landau and I. Pomeranchuk, “Limits of applicability of the theory of
2654 bremsstrahlung electrons and pair production at high-energies,” *Dokl. Akad. Nauk Ser. Fiz.* **92** (1953) 535–536.
- 2655 [148] A. B. Migdal, “Bremsstrahlung and pair production in condensed media at
2657 high-energies,” *Phys. Rev. 103* (1956) 1811–1820.
- 2658 [149] P. Bosted, M. Cavalli-Sforza, L. Kellerl, R. Becker-Szendyl, P. L. Anthony,
2659 L. M. Kelley, S. Klein, G. Niemi, M. Perll, L. S. Rochester, and J. White,
2660 “Quantum-mechanical suppression of bremsstrahlung*,” 1993.

- 2661 [150] R. Baier, Y. L. Dokshitzer, A. H. Mueller, S. Peigne, and D. Schiff,
 2662 “Radiative energy loss and p(T) broadening of high-energy partons in
 2663 nuclei,” *Nucl. Phys.* **B484** (1997) 265–282, [arXiv:hep-ph/9608322](#)
 2664 [hep-ph].
- 2665 [151] A. Majumder and M. Van Leeuwen, “The Theory and Phenomenology of
 2666 Perturbative QCD Based Jet Quenching,” *Prog.Part.Nucl.Phys.* **A66**
 2667 (2011) 41–92, [arXiv:1002.2206](#) [hep-ph].
- 2668 [152] F. Dominguez, C. Marquet, A. Mueller, B. Wu, and B.-W. Xiao,
 2669 “Comparing energy loss and p-perpendicular - broadening in perturbative
 2670 QCD with strong coupling N = 4 SYM theory,” *Nucl.Phys.* **A811** (2008)
 2671 197–222, [arXiv:0803.3234](#) [nucl-th].
- 2672 [153] M. Gyulassy, P. Levai, and I. Vitev, “Jet quenching in thin quark gluon
 2673 plasmas. 1. Formalism,” *Nucl.Phys.* **B571** (2000) 197–233,
 2674 [arXiv:hep-ph/9907461](#) [hep-ph].
- 2675 [154] U. A. Wiedemann, “Gluon radiation off hard quarks in a nuclear
 2676 environment: Opacity expansion,” *Nucl.Phys.* **B588** (2000) 303–344,
 2677 [arXiv:hep-ph/0005129](#) [hep-ph].
- 2678 [155] P. B. Arnold, G. D. Moore, and L. G. Yaffe, “Photon emission from quark
 2679 gluon plasma: Complete leading order results,” *JHEP* **0112** (2001) 009,
 2680 [arXiv:hep-ph/0111107](#) [hep-ph].
- 2681 [156] X.-N. Wang and X.-f. Guo, “Multiple parton scattering in nuclei: Parton
 2682 energy loss,” *Nucl.Phys.* **A696** (2001) 788–832, [arXiv:hep-ph/0102230](#)
 2683 [hep-ph].
- 2684 [157] T. Sjostrand, S. Mrenna, and P. Z. Skands, “A Brief Introduction to
 2685 PYTHIA 8.1,” *Comput.Phys.Commun.* **178** (2008) 852–867,
 2686 [arXiv:0710.3820](#) [hep-ph].
- 2687 [158] I. Lokhtin and A. Snigirev, “A Model of jet quenching in ultrarelativistic
 2688 heavy ion collisions and high-p(T) hadron spectra at RHIC,” *Eur.Phys.J.*
 2689 **C45** (2006) 211–217, [arXiv:hep-ph/0506189](#) [hep-ph].
- 2690 [159] N. Armesto, L. Cunqueiro, and C. A. Salgado, “Monte Carlo for Jet
 2691 Showers in the Medium,” *Nucl.Phys.* **A830** (2009) 271C–274C,
 2692 [arXiv:0907.4706](#) [hep-ph].
- 2693 [160] K. Zapp, G. Ingelman, J. Rathsman, J. Stachel, and U. A. Wiedemann, “A
 2694 Monte Carlo Model for ‘Jet Quenching’,” *Eur.Phys.J.* **C60** (2009) 617–632,
 2695 [arXiv:0804.3568](#) [hep-ph].

- 2696 [161] T. Renk, “A Comparison study of medium-modified QCD shower evolution
2697 scenarios,” *Phys. Rev.* **C79** (2009) 054906, [arXiv:0901.2818 \[hep-ph\]](#).
- 2698 [162] **ALICE** Collaboration, J. Adam *et al.*, “Measurement of jet suppression in
2699 central Pb-Pb collisions at $\sqrt{s_{NN}} = 2.76$ TeV,” *Phys. Lett.* **B746** (2015)
2700 1–14, [arXiv:1502.01689 \[nucl-ex\]](#).
- 2701 [163] **ATLAS** Collaboration, G. Aad *et al.*, “Measurements of the Nuclear
2702 Modification Factor for Jets in Pb+Pb Collisions at $\sqrt{s_{NN}} = 2.76$ TeV with
2703 the ATLAS Detector,” *Phys. Rev. Lett.* **114** no. 7, (2015) 072302,
2704 [arXiv:1411.2357 \[hep-ex\]](#).
- 2705 [164] **CMS** Collaboration, V. Khachatryan *et al.*, “Measurement of inclusive jet
2706 cross sections in pp and PbPb collisions at $\sqrt{s_{NN}} = 2.76$ TeV,” *Phys. Rev.*
2707 **C96** no. 1, (2017) 015202, [arXiv:1609.05383 \[nucl-ex\]](#).
- 2708 [165] **STAR** Collaboration, L. Adamczyk *et al.*, “Jet-Hadron Correlations in
2709 $\sqrt{s_{NN}} = 200$ GeV $p + p$ and Central $Au + Au$ Collisions,” *Phys. Rev. Lett.*
2710 **112** no. 12, (2014) 122301, [arXiv:1302.6184 \[nucl-ex\]](#).
- 2711 [166] **CMS** Collaboration, V. Khachatryan *et al.*, “Correlations between jets and
2712 charged particles in PbPb and pp collisions at $\sqrt{s_{NN}} = 2.76$ TeV,” *JHEP*
2713 **02** (2016) 156, [arXiv:1601.00079 \[nucl-ex\]](#).
- 2714 [167] A. Kurkela and U. A. Wiedemann, “Picturing perturbative parton cascades
2715 in QCD matter,” *Phys. Lett.* **B740** (2015) 172–178, [arXiv:1407.0293 \[hep-ph\]](#).
- 2717 [168] **JETSCAPE** Collaboration, Y. Tachibana *et al.*, “Jet substructure
2718 modification in a QGP from a multi-scale description of jet evolution with
2719 JETSCAPE,” 2018. [arXiv:1812.06366 \[nucl-th\]](#).
- 2720 [169] P. Aurenche and B. G. Zakharov, “Jet color chemistry and anomalous
2721 baryon production in AA -collisions,” *Eur. Phys. J.* **C71** (2011) 1829,
2722 [arXiv:1109.6819 \[hep-ph\]](#).
- 2723 [170] A. Beraudo, J. G. Milhano, and U. A. Wiedemann, “Medium-induced color
2724 flow softens hadronization,” *Phys. Rev.* **C85** (2012) 031901,
2725 [arXiv:1109.5025 \[hep-ph\]](#).
- 2726 [171] A. Beraudo, J. G. Milhano, and U. A. Wiedemann, “The Contribution of
2727 Medium-Modified Color Flow to Jet Quenching,” *JHEP* **07** (2012) 144,
2728 [arXiv:1204.4342 \[hep-ph\]](#).

- 2729 [172] J. Casalderrey-Solana, Y. Mehtar-Tani, C. A. Salgado, and K. Tywoniuk,
2730 “New picture of jet quenching dictated by color coherence,” *Phys. Lett.*
2731 **B725** (2013) 357–360, [arXiv:1210.7765](https://arxiv.org/abs/1210.7765) [hep-ph].
- 2732 [173] F. D’Eramo, M. Lekaveckas, H. Liu, and K. Rajagopal, “Momentum
2733 Broadening in Weakly Coupled Quark-Gluon Plasma (with a view to
2734 finding the quasiparticles within liquid quark-gluon plasma),” *JHEP* **05**
2735 (2013) 031, [arXiv:1211.1922](https://arxiv.org/abs/1211.1922) [hep-ph].
- 2736 [174] A. Ayala, I. Dominguez, J. Jalilian-Marian, and M. E. Tejeda-Yeomans,
2737 “Relating \hat{q} , η/s and ΔE in an expanding quark-gluon plasma,” *Phys. Rev.*
2738 **C94** no. 2, (2016) 024913, [arXiv:1603.09296](https://arxiv.org/abs/1603.09296) [hep-ph].
- 2739 [175] G. Moliere, “Theorie der Streuung schneller geladener Teilchen I.
2740 Einzelstreuung am abgeschirmten Coulomb-Feld,” *Z. Naturforsch.* **A2**
2741 (1947) 133.
- 2742 [176] **CMS** Collaboration, S. Chatrchyan *et al.*, “Observation and studies of jet
2743 quenching in PbPb collisions at nucleon-nucleon center-of-mass energy =
2744 2.76 TeV,” *Phys. Rev.* **C84** (2011) 024906, [arXiv:1102.1957](https://arxiv.org/abs/1102.1957) [nucl-ex].
- 2745 [177] C. Aidala *et al.*, “Measurement of long-range angular correlations and
2746 azimuthal anisotropies in high-multiplicity $p+\text{Au}$ collisions at $\sqrt{s_{NN}} = 200$
2747 GeV,” *Phys. Rev.* **C95** no. 3, (2017) 034910, [arXiv:1609.02894](https://arxiv.org/abs/1609.02894)
2748 [nucl-ex].
- 2749 [178] **PHENIX** Collaboration, S. S. Adler *et al.*, “Absence of suppression in
2750 particle production at large transverse momentum in $S(\text{NN})^{**}(1/2) =$
2751 200-GeV $d + \text{Au}$ collisions,” *Phys. Rev. Lett.* **91** (2003) 072303,
2752 [arXiv:nucl-ex/0306021](https://arxiv.org/abs/nucl-ex/0306021) [nucl-ex].
- 2753 [179] **BRAHMS** Collaboration, I. Arsene *et al.*, “Transverse momentum spectra
2754 in $\text{Au}+\text{Au}$ and $d+\text{Au}$ collisions at $s^{**}(1/2) = 200$ -GeV and the
2755 pseudorapidity dependence of high $p(T)$ suppression,” *Phys. Rev. Lett.* **91**
2756 (2003) 072305, [arXiv:nucl-ex/0307003](https://arxiv.org/abs/nucl-ex/0307003) [nucl-ex].
- 2757 [180] **PHOBOS** Collaboration, B. B. Back *et al.*, “Centrality dependence of
2758 charged hadron transverse momentum spectra in $d + \text{Au}$ collisions at
2759 $S(\text{NN})^{**}1/2 = 200$ GeV,” *Phys. Rev. Lett.* **91** (2003) 072302,
2760 [arXiv:nucl-ex/0306025](https://arxiv.org/abs/nucl-ex/0306025) [nucl-ex].
- 2761 [181] **STAR** Collaboration, J. Adams *et al.*, “Evidence from $d + \text{Au}$
2762 measurements for final state suppression of high $p(T)$ hadrons in $\text{Au}+\text{Au}$

- 2763 collisions at RHIC,” *Phys. Rev. Lett.* **91** (2003) 072304,
 2764 [arXiv:nucl-ex/0306024 \[nucl-ex\]](#).
- 2765 [182] **PHENIX** Collaboration, A. Adare *et al.*, “Measurements of elliptic and
 2766 triangular flow in high-multiplicity ${}^3\text{He}+\text{Au}$ collisions at $\sqrt{s_{NN}} = 200$
 2767 GeV,” *Phys. Rev. Lett.* **115** no. 14, (2015) 142301, [arXiv:1507.06273](#)
 2768 [nucl-ex].
- 2769 [183] **E735** Collaboration, T. Alexopoulos *et al.*, “Mass identified particle
 2770 production in $p\bar{p}$ collisions at $\sqrt{s} = 300\text{-GeV}$, 540-GeV, 1000-GeV, and
 2771 1800-GeV,” *Phys. Rev.* **D48** (1993) 984–997.
- 2772 [184] **MiniMax** Collaboration, T. C. Brooks *et al.*, “A Search for disoriented
 2773 chiral condensate at the Fermilab Tevatron,” *Phys. Rev.* **D61** (2000)
 2774 032003, [arXiv:hep-ex/9906026 \[hep-ex\]](#).
- 2775 [185] C. Shen, Z. Qiu, and U. Heinz, “Shape and flow fluctuations in ultracentral
 2776 $\text{Pb} + \text{Pb}$ collisions at the energies available at the CERN Large Hadron
 2777 Collider,” *Phys. Rev.* **C92** no. 1, (2015) 014901, [arXiv:1502.04636](#)
 2778 [nucl-th].
- 2779 [186] **PHENIX** Collaboration, A. Adare *et al.*, “Azimuthally anisotropic
 2780 emission of low-momentum direct photons in $\text{Au}+\text{Au}$ collisions at
 2781 $\sqrt{s_{NN}} = 200$ GeV,” *Phys. Rev.* **C94** no. 6, (2016) 064901,
 2782 [arXiv:1509.07758 \[nucl-ex\]](#).
- 2783 [187] **CMS** Collaboration, V. Khachatryan *et al.*, “Observation of Long-Range
 2784 Near-Side Angular Correlations in Proton-Proton Collisions at the LHC,”
 2785 *JHEP* **09** (2010) 091, [arXiv:1009.4122 \[hep-ex\]](#).
- 2786 [188] C. A. Salgado and J. P. Wessels, “Proton–Lead Collisions at the CERN
 2787 LHC,” *Ann. Rev. Nucl. Part. Sci.* **66** (2016) 449–473.
- 2788 [189] **ATLAS** Collaboration, G. Aad *et al.*, “Observation of Long-Range Elliptic
 2789 Azimuthal Anisotropies in $\sqrt{s} = 13$ and 2.76 TeV $p\bar{p}$ Collisions with the
 2790 ATLAS Detector,” *Phys. Rev. Lett.* **116** no. 17, (2016) 172301,
 2791 [arXiv:1509.04776 \[hep-ex\]](#).
- 2792 [190] **ALICE** Collaboration, S. Acharya *et al.*, “Searches for transverse
 2793 momentum dependent flow vector fluctuations in Pb-Pb and p-Pb collisions
 2794 at the LHC,” *JHEP* **09** (2017) 032, [arXiv:1707.05690 \[nucl-ex\]](#).
- 2795 [191] C. Shen, J.-F. Paquet, G. S. Denicol, S. Jeon, and C. Gale, “Collectivity
 2796 and electromagnetic radiation in small systems,” *Phys. Rev.* **C95** no. 1,
 2797 (2017) 014906, [arXiv:1609.02590 \[nucl-th\]](#).

- 2798 [192] H. Niemi and G. S. Denicol, “How large is the Knudsen number reached in
 2799 fluid dynamical simulations of ultrarelativistic heavy ion collisions?,”
 2800 arXiv:1404.7327 [nucl-th].
- 2801 [193] **PHENIX** Collaboration, C. Aidala *et al.*, “Creation of quark-gluon
 2802 plasma droplets with three distinct geometries,” *Nature Phys.* **15** no. 3,
 2803 (2019) 214–220, arXiv:1805.02973 [nucl-ex].
- 2804 [194] **CMS** Collaboration, C. Collaboration, “Elliptic flow of charm and strange
 2805 hadrons in high-multiplicity pPb collisions at $\sqrt{s_{NN}} = 8.16 \text{ TeV}$,”
- 2806 [195] **CMS** Collaboration, V. Khachatryan *et al.*, “Charged-particle nuclear
 2807 modification factors in PbPb and pPb collisions at $\sqrt{s_{NN}} = 5.02 \text{ TeV}$,”
 2808 *JHEP* **04** (2017) 039, arXiv:1611.01664 [nucl-ex].
- 2809 [196] **ATLAS** Collaboration, G. Aad *et al.*, “Measurement of long-range
 2810 pseudorapidity correlations and azimuthal harmonics in $\sqrt{s_{NN}} = 5.02 \text{ TeV}$
 2811 proton-lead collisions with the ATLAS detector,” *Phys. Rev.* **C90** no. 4,
 2812 (2014) 044906, arXiv:1409.1792 [hep-ex].
- 2813 [197] X. Zhang and J. Liao, “Jet Quenching and Its Azimuthal Anisotropy in AA
 2814 and possibly High Multiplicity pA and dA Collisions,” arXiv:1311.5463
 2815 [nucl-th].
- 2816 [198] C. Park, C. Shen, S. Jeon, and C. Gale, “Rapidity-dependent jet energy loss
 2817 in small systems with finite-size effects and running coupling,” *Nucl. Part.
 2818 Phys. Proc.* **289-290** (2017) 289–292, arXiv:1612.06754 [nucl-th].
- 2819 [199] K. Tywoniuk, “Is there jet quenching in pPb?,” *Nucl. Phys.* **A926** (2014)
 2820 85–91.
- 2821 [200] **CMS** Collaboration, A. M. Sirunyan *et al.*, “Azimuthal anisotropy of
 2822 charged particles with transverse momentum up to 100 GeV/ c in PbPb
 2823 collisions at $\sqrt{s_{NN}}=5.02 \text{ TeV}$,” *Phys. Lett.* **B776** (2018) 195–216,
 2824 arXiv:1702.00630 [hep-ex].
- 2825 [201] **ALICE** Collaboration, J. Adam *et al.*, “Centrality dependence of particle
 2826 production in p-Pb collisions at $\sqrt{s_{NN}}= 5.02 \text{ TeV}$,” *Phys. Rev.* **C91** no. 6,
 2827 (2015) 064905, arXiv:1412.6828 [nucl-ex].
- 2828 [202] F. Sikler, “Centrality control of hadron nucleus interactions by detection of
 2829 slow nucleons,” arXiv:hep-ph/0304065 [hep-ph].
- 2830 [203] “Cern.” [Https://home.cern/](https://home.cern/). Accessed: Wed. 17 Apr 2019.

- 2831 [204] 2019. <http://cds.cern.ch/record/2197559/>.
- 2832 [205] P. M. Watkins, “DISCOVERY OF THE W AND Z BOSONS,” *Contemp.*
2833 *Phys.* **27** (1986) 291–324.
- 2834 [206] **NA61/SHINE** Collaboration, A. Laszlo, “The NA61/SHINE Experiment
2835 at the CERN SPS,” *Nucl. Phys.* **A830** (2009) 559C–562C,
2836 [arXiv:0907.4493](https://arxiv.org/abs/0907.4493) [[nucl-ex](#)].
- 2837 [207] **NA62 Collaboration** Collaboration, F. Hahn, F. Ambrosino,
2838 A. Ceccucci, H. Danielsson, N. Doble, F. Fantechi, A. Kluge, C. Lazzeroni,
2839 M. Lenti, G. Ruggiero, M. Sozzi, P. Valente, and R. Wanke, “NA62:
2840 Technical Design Document,” Tech. Rep. NA62-10-07, CERN, Geneva,
2841 Dec, 2010. <https://cds.cern.ch/record/1404985>.
- 2842 [208] **NA63 Collaboration** Collaboration, R. Mikkelsen, U. Uggerhoj, and
2843 T. Wistisen, “Technical Design Report, CERN NA63,” Tech. Rep.
2844 CERN-SPSC-2014-033. SPSC-SR-146, CERN, Geneva, Oct, 2014.
2845 <https://cds.cern.ch/record/1955391>.
- 2846 [209] **AWAKE** Collaboration, S. Döbert, “The Proton Driven Advanced Wake
2847 Field Acceleration Experiment (AWAKE) at CERN.”,
2848 <https://cds.cern.ch/record/2669231>.
- 2849 [210] R. Losito, E. Laface, and W. Scandale, “The UA9 Experiment at the
2850 CERN-SPS.”. <https://cds.cern.ch/record/1223625>.
- 2851 [211] **DIRAC** Collaboration, C. P. Schuetz, “The Dirac experiment at CERN,”
2852 in *Proceedings, 38th Rencontres de Moriond on QCD and High-Energy*
2853 *Hadronic Interactions: Les Arcs, France, March 22-29, 2003.* 2003.
2854 [arXiv:hep-ph/0305121](https://arxiv.org/abs/hep-ph/0305121) [[hep-ph](#)].
- 2855 [212] E. M. Dunne *et al.*, “Global atmospheric particle formation from cern cloud
2856 measurements,” *Science* **354** no. 6316, (2016) 1119–1124.
2857 <https://science.sciencemag.org/content/354/6316/1119>.
- 2858 [213] **n_TOF** Collaboration, P. M. Milazzo *et al.*, “Neutron Capture
2859 Measurements at the n_TOF Facility,” *AIP Conf. Proc.* **1109** no. 1,
2860 (2009) 84.
- 2861 [214] “Cern experiments,” 2019. <https://home.cern/science/experiments>.
- 2862 [215] O. S. Brüning, P. Collier, P. Lebrun, S. Myers, R. Ostojic, J. Poole, and
2863 P. Proudlock, *LHC Design Report*. CERN Yellow Reports: Monographs.
2864 CERN, Geneva, 2004. <https://cds.cern.ch/record/782076>.

- 2865 [216] L. Evans and P. Bryant, “LHC Machine,” *JINST* **3** (2008) S08001.
- 2866 [217] **ALICE** Collaboration, K. Aamodt *et al.*, “The ALICE experiment at the
2867 CERN LHC,” *JINST* **3** (2008) S08002.
- 2868 [218] **ATLAS** Collaboration, G. Aad *et al.*, “The ATLAS Experiment at the
2869 CERN Large Hadron Collider,” *JINST* **3** (2008) S08003.
- 2870 [219] **CMS** Collaboration, S. Chatrchyan *et al.*, “The CMS Experiment at the
2871 CERN LHC,” *JINST* **3** (2008) S08004.
- 2872 [220] **LHCb** Collaboration, A. A. Alves, Jr. *et al.*, “The LHCb Detector at the
2873 LHC,” *JINST* **3** (2008) S08005.
- 2874 [221] **LHCf** Collaboration, O. Adriani *et al.*, “The LHCf detector at the CERN
2875 Large Hadron Collider,” *JINST* **3** (2008) S08006.
- 2876 [222] **TOTEM** Collaboration, G. Anelli *et al.*, “The TOTEM experiment at the
2877 CERN Large Hadron Collider,” *JINST* **3** (2008) S08007.
- 2878 [223] **MoEDAL** Collaboration, B. Acharya *et al.*, “Search for magnetic
2879 monopoles with the MoEDAL prototype trapping detector in 8 TeV
2880 proton-proton collisions at the LHC,” *JHEP* **08** (2016) 067,
2881 [arXiv:1604.06645 \[hep-ex\]](https://arxiv.org/abs/1604.06645).
- 2882 [224] **ATLAS** Collaboration, G. Aad *et al.*, “Observation of a new particle in the
2883 search for the Standard Model Higgs boson with the ATLAS detector at
2884 the LHC,” *Phys. Lett.* **B716** (2012) 1–29, [arXiv:1207.7214 \[hep-ex\]](https://arxiv.org/abs/1207.7214).
- 2885 [225] **CMS** Collaboration, S. Chatrchyan *et al.*, “Observation of a new boson at
2886 a mass of 125 GeV with the CMS experiment at the LHC,” *Phys. Lett.*
2887 **B716** (2012) 30–61, [arXiv:1207.7235 \[hep-ex\]](https://arxiv.org/abs/1207.7235).
- 2888 [226] T. ALICE Collaboration, K. Aamodt, A. Abrahantes, R. Achenbach,
2889 S. Acounis, D. Adamova, C. Adler, M. Aggarwal, F. Agnese,
2890 G. Aglieri Rinella, Z. Ahammed, A. Ahmad, N. Ahmad, S. Ahmad,
2891 A. Akindinov, P. Akishin, D. Aleksandrov, B. Alessandro, R. Alfaro, and
2892 M. Zuffa, “The alice experiment at the cern lhc,” *Journal of
2893 Instrumentation* **3** (08, 2008) S08002.
- 2894 [227] **ALICE** Collaboration, K. Aamodt *et al.*, “Charged-particle multiplicity
2895 density at mid-rapidity in central Pb-Pb collisions at $\sqrt{s_{NN}} = 2.76$ TeV,”
2896 *Phys. Rev. Lett.* **105** (2010) 252301, [arXiv:1011.3916 \[nucl-ex\]](https://arxiv.org/abs/1011.3916).

- 2897 [228] **ALICE** Collaboration, G. Dellacasa *et al.*, “ALICE: Technical design
2898 report of the time projection chamber.”
- 2899 [229] **ALICE** Collaboration, G. Dellacasa *et al.*, “ALICE technical design report
2900 of the inner tracking system (ITS),”.
- 2901 [230] **ALICE** Collaboration, I. Belikov, “Upgrade of the ALICE Inner Tracking
2902 System,” *EPJ Web Conf.* **125** (2016) 01004, [arXiv:1607.01171](https://arxiv.org/abs/1607.01171)
2903 [[physics.ins-det](#)].
- 2904 [231] J. Alme *et al.*, “The ALICE TPC, a large 3-dimensional tracking device
2905 with fast readout for ultra-high multiplicity events,” *Nucl. Instrum. Meth.*
2906 **A622** (2010) 316–367, [arXiv:1001.1950](https://arxiv.org/abs/1001.1950) [[physics.ins-det](#)].
- 2907 [232] **for the ALICE** Collaboration, C. Zampolli, “Particle Identification with
2908 the ALICE detector at the LHC,” in *Proceedings, PLHC2012: Physics at
2909 the LHC 2012 (PLHC2012): Vancouver, BC, Canada, June 4-9, 2012.*
2910 2012. [arXiv:1209.5637](https://arxiv.org/abs/1209.5637) [[hep-ex](#)].
- 2911 [233] **ALICE Collaboration** Collaboration, P. Cortese, *ALICE
2912 transition-radiation detector: Technical Design Report*. Technical Design
2913 Report ALICE. CERN, Geneva, 2001.
2914 <https://cds.cern.ch/record/519145>.
- 2915 [234] **ALICE** Collaboration, G. Dellacasa *et al.*, “ALICE technical design report
2916 of the time-of-flight system (TOF),”.
- 2917 [235] **ALICE** Collaboration, S. Beole *et al.*, “ALICE technical design report:
2918 Detector for high momentum PID,”.
- 2919 [236] **ALICE** Collaboration, B. Abelev *et al.*, “Neutral pion and η meson
2920 production in proton-proton collisions at $\sqrt{s} = 0.9$ TeV and $\sqrt{s} = 7$ TeV,”
2921 *Phys. Lett.* **B717** (2012) 162–172, [arXiv:1205.5724](https://arxiv.org/abs/1205.5724) [[hep-ex](#)].
- 2922 [237] **ALICE** Collaboration, J. Adam *et al.*, “Direct photon production in
2923 Pb-Pb collisions at $\sqrt{s_{\text{NN}}} = 2.76$ TeV,” *Phys. Lett.* **B754** (2016) 235–248,
2924 [arXiv:1509.07324](https://arxiv.org/abs/1509.07324) [[nucl-ex](#)].
- 2925 [238] **ALICE** Collaboration, R. Reed, “Full Jet Reconstruction in 2.76 TeV pp
2926 and Pb-Pb collisions in the ALICE experiment,” *J. Phys. Conf. Ser.* **446**
2927 (2013) 012006, [arXiv:1304.5945](https://arxiv.org/abs/1304.5945) [[nucl-ex](#)].
- 2928 [239] **ALICE** Collaboration, G. Dellacasa *et al.*, “ALICE technical design report
2929 of the photon spectrometer (PHOS),”.

- 2930 [240] **ALICE** Collaboration, P. Cortese *et al.*, “ALICE electromagnetic
2931 calorimeter technical design report.”
- 2932 [241] J. Allen *et al.*, “ALICE DCal: An Addendum to the EMCal Technical
2933 Design Report Di-Jet and Hadron-Jet correlation measurements in
2934 ALICE,” Tech. Rep. CERN-LHCC-2010-011. ALICE-TDR-14-add-1, Jun,
2935 2010. <https://cds.cern.ch/record/1272952>.
- 2936 [242] **ALICE** Collaboration, P. Cortese *et al.*, “ALICE technical design report
2937 on forward detectors: FMD, T0 and V0.”
- 2938 [243] **ALICE** Collaboration, A. I. Maevskaya, “Fast Interaction Trigger for the
2939 upgrade of the ALICE experiment at CERN: design and performance,”
2940 arXiv:1812.00594 [physics.ins-det].
- 2941 [244] **ALICE** Collaboration Collaboration, *ALICE Photon Multiplicity
2942 Detector (PMD): Technical Design Report*. Technical Design Report
2943 ALICE. CERN, Geneva, 1999. <https://cds.cern.ch/record/451099>.
- 2944 [245] **ACORDE** Collaboration, A. Fernández *et al.*, “ACORDE a Cosmic Ray
2945 Detector for ALICE,” *Nucl. Instrum. Meth.* **A572** (2007) 102–103,
2946 arXiv:physics/0606051 [physics.ins-det].
- 2947 [246] **ALICE** Collaboration, G. Dellacasa *et al.*, “ALICE technical design report
2948 of the zero degree calorimeter (ZDC),”
- 2949 [247] A. Villatoro Tello, “Ad, the alice diffractive detector,” *AIP Conference
2950 Proceedings* **1819** (03, 2017) .
- 2951 [248] **ALICE** Collaboration, S. Beole *et al.*, “The forward muon spectrometer of
2952 ALICE,”
- 2953 [249] **ALICE** Collaboration, M. Krivda, D. Alexandre, L. S. Barnby, D. Evans,
2954 P. G. Jones, A. Jusko, R. Lietava, J. Pospíšil, and O. V. Baillie, “The
2955 ALICE Central Trigger Processor (CTP) upgrade,” *JINST* **11** no. 03,
2956 (2016) C03051.
- 2957 [250] J. Král, *Intrinsic transverse momentum distribution of jet constituents in
2958 p-Pb collisions at ALICE*. PhD thesis, University of Jyväskylä, 8, 2014.
- 2959 [251] J. Kral, T. Awes, H. Muller, J. Rak, and J. Schambach, “L0 trigger for the
2960 emcal detector of the alice experiment,” *Nuclear Instruments and Methods
2961 in Physics Research Section A: Accelerators, Spectrometers, Detectors and
2962 Associated Equipment* **693** (2012) 261 – 267. http:
2963 //www.sciencedirect.com/science/article/pii/S0168900212007681.

- 2964 [252] **ALICE Collaboration** Collaboration, B. Abelev *et al.*, “Upgrade of the
 2965 ALICE Experiment: Letter of Intent,” Tech. Rep. CERN-LHCC-2012-012.
 2966 LHCC-I-022. ALICE-UG-002, CERN, Geneva, Aug, 2012.
 2967 <https://cds.cern.ch/record/1475243>.
- 2968 [253] A. Maevskaya, “Fast Interaction Trigger for the upgrade of the ALICE
 2969 experiment at CERN: design and performance,” *EPJ Web Conf.* **204**
 2970 (2019) 11003.
- 2971 [254] “Technical Design Report for the Muon Forward Tracker,” Tech. Rep.
 2972 CERN-LHCC-2015-001. ALICE-TDR-018, Jan, 2015.
 2973 <https://cds.cern.ch/record/1981898>.
- 2974 [255] F. Sauli, L. Ropelewski, and P. Everaerts, “Ion feedback suppression in
 2975 time projection chambers,” *Nucl. Instrum. Meth.* **A560** (2006) 269–277.
- 2976 [256] **ALICE TPC** Collaboration, M. Ball, K. Eckstein, and T. Gunji, “Ion
 2977 backflow studies for the ALICE TPC upgrade with GEMs,” *JINST* **9**
 2978 (2014) C04025.
- 2979 [257] **The ALICE Collaboration** Collaboration, “Upgrade of the ALICE Time
 2980 Projection Chamber,” Tech. Rep. CERN-LHCC-2013-020.
 2981 ALICE-TDR-016, Oct, 2013. <http://cds.cern.ch/record/1622286>.
- 2982 [258] P. F. Little, *Secondary Effects*, pp. 574–662. Springer Berlin Heidelberg,
 2983 Berlin, Heidelberg, 1956.
 2984 https://doi.org/10.1007/978-3-642-45844-6_9.
- 2985 [259] M. Vargyas, *Jet shape modification in Pb-Pb collisions at $\sqrt{s_{\text{NN}}} = 2.76 \text{ TeV}$ using two-particle correlations*. PhD thesis, University of Jyväskylä, 11,
 2986 2018.
- 2987 [260] **ALICE TPC upgrade** Collaboration, J. E. Brücke and T. E. Hildén,
 2988 “The GEM QA Protocol of the ALICE TPC Upgrade Project,” in *5th
 2989 International Conference on Micro Pattern Gas Detectors (MPGD2017)
 2990 Temple University, Philadelphia, USA, May 22-26, 2017*. 2018.
 2991 [arXiv:1811.07043](https://arxiv.org/abs/1811.07043) [physics.ins-det].
- 2992 [261] T. Hildén, E. Brücke, J. Heino, M. Kalliokoski, A. Karadzhinova,
 2993 R. Lauhakangas, E. Tuominen, and R. Turpeinen, “Optical quality
 2994 assurance of GEM foils,” *Nucl. Instrum. Meth.* **A770** (2015) 113–122,
 2995 [arXiv:1704.06691](https://arxiv.org/abs/1704.06691) [physics.ins-det].

- 2997 [262] **ALICE** Collaboration, B. B. Abelev *et al.*, “Performance of the ALICE
 2998 Experiment at the CERN LHC,” *Int. J. Mod. Phys. A***29** (2014) 1430044,
 2999 arXiv:1402.4476 [nucl-ex].
- 3000 [263] **ALICE** Collaboration, K. Aamodt *et al.*, “Alignment of the ALICE Inner
 3001 Tracking System with cosmic-ray tracks,” *JINST* **5** (2010) P03003,
 3002 arXiv:1001.0502 [physics.ins-det].
- 3003 [264] R. Fruhwirth, “Application of Kalman filtering to track and vertex fitting,”
 3004 *Nucl. Instrum. Meth. A***262** (1987) 444–450.
- 3005 [265] A. Maire, “Track reconstruction principle in ALICE for LHC run I and run
 3006 II. Principes de reconstruction de traces dans ALICE pour les runs I et II
 3007 du LHC.” General Photo, Oct, 2011.
- 3008 [266] **ALICE** Collaboration, B. Abelev *et al.*, “Measurement of Event
 3009 Background Fluctuations for Charged Particle Jet Reconstruction in Pb-Pb
 3010 collisions at $\sqrt{s_{NN}} = 2.76$ TeV,” *JHEP* **03** (2012) 053, arXiv:1201.2423
 3011 [hep-ex].
- 3012 [267] **ALICE** Collaboration, B. Abelev *et al.*, “Long-range angular correlations
 3013 on the near and away side in p -Pb collisions at $\sqrt{s_{NN}} = 5.02$ TeV,” *Phys.*
 3014 *Lett. B***719** (2013) 29–41, arXiv:1212.2001 [nucl-ex].
- 3015 [268] M. Cacciari, G. P. Salam, and G. Soyez, “FastJet User Manual,” *Eur. Phys.*
 3016 *J. C***72** (2012) 1896, arXiv:1111.6097 [hep-ph].
- 3017 [269] M. Cacciari, G. P. Salam, and G. Soyez, “The anti- k_t jet clustering
 3018 algorithm,” *JHEP* **04** (2008) 063, arXiv:0802.1189 [hep-ph].
- 3019 [270] T. Sjöstrand, S. Mrenna, and P. Z. Skands, “A Brief Introduction to
 3020 PYTHIA 8.1,” *Comput. Phys. Commun.* **178** (2008) 852–867,
 3021 arXiv:0710.3820 [hep-ph].
- 3022 [271] G. Upton and I. Cook, *A Dictionary of Statistics*. 01, 2008.
 3023 <http://www.oxfordreference.com/view/10.1093/acref/9780199541454.001.0001/acref-9780199541454>.
- 3025 [272] “Roounfold: Root unfolding framework.”
 3026 <http://hepunx.rl.ac.uk/~adye/software/unfold/RooUnfold.html>,
 3027 2013.
 3028 <http://hepunx.rl.ac.uk/~adye/software/unfold/RooUnfold.html>.
- 3029 [273] A. Hocker and V. Kartvelishvili, “SVD approach to data unfolding,” *Nucl.*
 3030 *Instrum. Meth. A***372** (1996) 469–481, arXiv:hep-ph/9509307 [hep-ph].

- 3031 [274] P. Z. Skands, “Tuning Monte Carlo Generators: The Perugia Tunes,” *Phys.*
3032 *Rev.* **D82** (2010) 074018, [arXiv:1005.3457](https://arxiv.org/abs/1005.3457) [hep-ph].
- 3033 [275] R. Brun, R. Hagelberg, M. Hansroul, and J. C. Lassalle, *Simulation*
3034 *program for particle physics experiments, GEANT: user guide and reference*
3035 *manual.* CERN, Geneva, 1978. <https://cds.cern.ch/record/118715>.
- 3036 [276] R. Brun, F. Bruyant, F. Carminati, S. Giani, M. Maire, A. McPherson,
3037 G. Patrick, and L. Urban, “GEANT Detector Description and Simulation
3038 Tool.”. [http://cds.cern.ch/record/1082634](https://cds.cern.ch/record/1082634).
- 3039 [277] **ALICE** Collaboration, S. Acharya *et al.*, “Jet fragmentation transverse
3040 momentum measurements from di-hadron correlations in $\sqrt{s} = 7$ TeV pp
3041 and $\sqrt{s_{NN}} = 5.02$ TeV p-Pb collisions,” *JHEP* **03** (2019) 169,
3042 [arXiv:1811.09742](https://arxiv.org/abs/1811.09742) [nucl-ex].
- 3043 [278] Y.-T. Chien and I. Vitev, “Towards the understanding of jet shapes and
3044 cross sections in heavy ion collisions using soft-collinear effective theory,”
3045 *JHEP* **05** (2016) 023, [arXiv:1509.07257](https://arxiv.org/abs/1509.07257) [hep-ph].